UiT The Arctic University of Norway

Faculty of Science and Technology

Department of Physics and Technology

Detection of Marine Plastic Debris in the North Pacific Ocean using Optical Satellite Imagery

Tora Båtvik

EOM-3901 Master's Thesis in Energy, Climate, and Environment – June 2021

To my parents,

for teaching me that the sky is not the limit.

“An understanding of the natural world is a source of not only great curiosity,
but great fulfilment.”
–Sir David Attenborough

Abstract

Plastic pollution is ubiquitous across marine environments, yet detection of anthropogenic debris in the global oceans is in its infancy. Here, we exploit high-resolution multispectral satellite imagery over the North Pacific Ocean and information from GPS-tracked floating plastic conglomerates to explore the potential for detecting marine plastic debris via spaceborne remote sensing platforms. Through an innovative method of estimating material abundance in mixed pixels, combined with an inverse spectral unmixing calculation, a spectral signature of aggregated plastic litter was derived from an 8-band WorldView-2 image. By leveraging the spectral characteristics of marine plastic debris in a real environment, plastic detectability was demonstrated and evaluated utilising a Spectral Angle Mapper (SAM) classification, Mixture Tuned Matched Filtering (MTMF), the Reed-Xiaoli Detector (RXD) algorithm, and spectral indices in a three-variable feature space. Results indicate that floating aggregations are detectable on sub-pixel scales, but as reliable ground truth information was restricted to a single confirmed target, detections were only validated by means of their respective spectral responses. Effects of atmospheric correction algorithms were evaluated using ACOLITE, ACOMP, and FLAASH, in which derived unbiased percentage differences ranged from 1% to 81% following a pairwise comparison. Building first steps towards an integrated marine monitoring system, the strengths and limitations of current remote sensing technology are identified and adopted to make suggestions for future improvements.

Acknowledgements

This project was in collaboration with Kongsberg Satellite Services (KSAT), who provided most of the satellite imagery and some additional reference datasets. I would like to sincerely thank them for the opportunity to work on such an important issue – and for introducing me to numerous scientists whose work I greatly admire. It has been such a pleasure to get involved in the remote sensing community. A special thanks goes out to Charlotte Bishop, my co-supervisor from KSAT, whom has provided me with invaluable guidance and insights throughout the project period.

I would also like to express my sincere thanks to Anthony P. Doulgeris, my university supervisor, for all scientific discussions, ideas, help, and availability. Our meetings have always given me an extra motivational boost.

The WorldView imagery provided by the National Oceanic and Atmospheric Administration (NOAA) was greatly appreciated, and indeed very useful, as the contents of this thesis would have been very different without it.

I am also grateful to the Geological Remote Sensing Group (GRSG) for their help with acquiring a one-year ENVI software licence, and to Harris Geospatial Solutions for providing me with the ENVI Atmospheric Correction Module.

Finally, to my family, and to all the fantastic people I have had the pleasure to meet throughout my educational journey – thank you. These years, as well as myself, would not have been the same without you.

Contents

List of Figures

List of Tables

Abbreviations

AC	Atmospheric Correction
BOA	Bottom-Of-Atmosphere
DEM	Digital Elevation Model
DN	Digital Number
EM	Electromagnetic
ENVI	ENvironment for Visualising Images
GCP	Ground Control Point
GPS	Global Positioning System
GPGP	Great Pacific Garbage Patch
GSD	Ground Sampling Distance
KSAT	Kongsberg Satellite Services
MS	Multispectral
MTMF	Mixture Tuned Matched Filtering
NDVI	Normalised Difference Vegetation Index
NIR	Near-Infrared
NOAA	National Oceanic and Atmospheric Administration
PCA	Principal Component Analysis

PET	Polyethylene Terephthalate
PPI	Pixel Purity Index
RGB	Red-Green-Blue
RNDWI	Reversed Normalised Difference Water Index
RPC	Rational Polynomial Coefficient
SAM	Spectral Angle Mapper
SAR	Synthetic Aperture Radar
SNR	Signal-to-Noise Ratio
SST	Sea Surface Temperature
SWIR	Shortwave Infrared
TOA	Top-Of-Atmosphere
UAV	Unmanned Aerial Vehicle
UPD	Unbiased Percentage Differences
UTC	Coordinated Universal Time
UTM	Universal Transverse Mercator
VNIR	Visible and Near-Infrared
WV2	WorldView-2
WV3	WorldView-3
WV-WCI	WorldView Whitecaps Index

1 Introduction

Millions of tonnes of plastic litter enter our oceans each year (Biermann et al., 2020). Once there, the vast majority is expected to remain in the environment in some form over geological timescales – severely affecting marine ecosystems, the economy, and human health. The cumulative increase of marine plastic debris over the last six decades (Kikaki et al., 2020) is a worrying trend, and targeting conglomerates and individual pieces of plastic for clean-up has proven difficult in the large global oceans. Scientists have primarily relied on vessel-based observations for detection, but this technique is both costly and inefficient. In the wake of recent technological advancements, a new field of research has emerged in which the potential of satellite imagery for marine plastic detection is being explored. If successful, spaceborne remote sensing can bridge gaps between the currently sparse *in situ* observations (Maximenko et al., 2019) and provide global coverage with unmatched revisit frequency. Further research is needed before satellite technology can be fully exploited, but an increasing global concern for marine plastic littering along with several promising studies are paving the way for further advancements in the field.

1.1 Background and Motivation

With limited existing research on open water litter analysis, a number of studies have taken first steps towards marine plastic debris detection. Some have approached the detection problem through the use of modelling (Politikos

et al., 2017; Liubartseva et al., 2018; Prevenios et al., 2018; Meyerjürgens et al., 2019; Mansui et al., 2020; Sebille et al., 2020) or remote sensing (Topouzelis et al., 2019; Biermann et al., 2019; Topouzelis et al., 2020), while others have used information based on sighting reports from shipborne observers (Suaria and Aliani, 2014). Maximenko et al. presented the need for an integrated marine debris observing system in 2019, suggesting detection requirements and identifying current limitations. Owing to the vastness of the global oceans, remote sensing is a key tool for the detection of marine plastic litter because of the superior spatial and temporal coverage. An initial assessment of spaceborne observation requirements was given by Martínez-Vicente et al. (2019), while Dubucq et al. (2020) reviewed recent improvements and remaining challenges for remote sensing detection of plastic waste. Although current remote sensing techniques are immature, several studies have explored plastics' detectability through aerial hyperspectral imaging (Garaba et al., 2018; Goddijn-Murphy et al., 2018), unmanned aerial vehicles (UAVs) or stable cameras (Moy et al., 2018; Fallati et al., 2019; Papachristopoulou et al., 2020), and with the direct use of satellite imagery (Aoyama, 2016; Biermann et al., 2019; Topouzelis et al., 2019; Topouzelis et al., 2020). Research has also demonstrated the potential of index-based detection algorithms (Biermann et al., 2020) as a valuable monitoring tool.

Using remote sensing, the detection problem can be approached in either a direct or an indirect manner. Some studies have gone the route of the latter, by finding correlations between plastic aggregation and sea surface parameters. For example, in Pichel et al. (2007), plastic debris densities were found to be significantly correlated with sea surface temperature (SST) and chlorophyll-A concentration and its gradient. Resulting from this discovery, satellite remote sensing data was used to derive SST and estimate chlorophyll aggregations to guide an aerial search for possible plastic accumulation zones. In another study, by considering spatio-temporal distributions of floating objects, Thiel et al. (2011) showed that higher abundances of anthropogenic debris typically were found in areas prone to developing coastal fronts and eddies during calm weather conditions.

More direct methods of measuring marine debris have been undertaken by several researchers in later years. For example, during the Plastic Litter Projects in 2018 and 2019 (Topouzelis et al., 2019; Topouzelis et al., 2020), large artificial floating plastic targets were deployed in coastal waters to examine detection abilities with the Sentinel-2 imager. As the targets were not large enough to cover a full pixel of the imagery (the highest spatial resolution for Sentinel-2 bands is 10 m), spectral image analysis took the form of an unmixing problem. The team of researchers was able to extract a signature for the PET (polyethylene terephthalate) targets, representing the spectral behaviour of marine plastics in a semi-natural environment. In another study, candidate pix-

els containing possible marine debris were extracted based on differing spectra from those of surrounding waters and wave crests (Aoyama, 2016), which were subsequently used in a spectral angle mapper (SAM) classification. In Biermann et al. (2020), the separability of plastics from other ocean targets was demonstrated using spectral indices and a supervised learning classifier.

Despite rapid advancements in marine debris detection algorithms, there are several gaps in existing research that must be addressed for a better understanding of marine plastic behaviour. Access to standardised *in situ* data is essential for automation of image analysis and to further develop knowledge of debris accumulation, plastics abundance, and aggregation hot spots (Biermann et al., 2019; Kornei, 2019), yet no such reference datasets exist to date. Extensive research is also needed to determine detection- and classification schemes' capabilities in imagery of different sensor characteristics.

This project is first and foremost an exploration study, with the aim of contributing to the developing field of marine debris research. By considering the potential and limitations of high-resolution satellite imagery, different methods are assessed to help determine how we can best utilise remote sensing in the battle against marine plastic.

1.2 Impacts of Marine Plastic Littering

Plastics are the most common form of marine litter, estimated to contribute from 60% to 80% of the total amount of marine debris (Martínez-Vicente et al., 2019). In the Great Pacific Garbage Patch (GPGP) alone, scientists predict that at least 79 thousand tonnes of ocean plastic is floating at or near the sea surface; a figure four to sixteen times higher than previously assumed for this area (Lebreton et al., 2018). Furthermore, there is sufficient evidence that the GPGP – the world's largest plastics accumulator – is constantly growing (Kikaki et al., 2020). The increasing amount of plastic in the ocean poses a serious threat not only to flora and fauna but also to human well-being. Fish and shellfish stocks are decreasing due to plastic contamination, and, coupled with broader factors such as climate change and overfishing, many species of fish are critically endangered (Beaumont et al., 2019). Approximately 46% of the plastic mass floating in the GPGP consists of derelict fishing gear, and an estimated 30% of the decline in some fish populations is assumed to be a direct consequence of such discarded equipment (Lebreton et al., 2018; Maximenko et al., 2019). In a study from 2015, plastics were found in more than 25% of individual fish and in >50% of the species collected from fish markets in Indonesia and the USA (Rochman et al., 2015), potentially introducing health risks to humans when

entering the food chain[1].

Figure 1.1: A sea turtle entangled in an abandoned fishing net. Image courtesy of NOAA.

Because of plastics' ability to withstand prolonged exposure to radiation and wave action, it can remain at the sea surface for long periods of time (decades or longer) and travel distances over 3000 kilometres from where it first originated (Beaumont et al., 2019). Plastic debris has been found in animals from different biomes all over the world, and its movement across large regions significantly increases the risk of transferring harmful bacteria and diseases between biomes.

Larger fauna, such as marine mammals and seabirds, are frequently exposed to harmful and even fatal entanglement and ingestion of plastics. For example, leatherback sea turtles often mistake plastic bags for jellyfish, their main food source, while albatrosses unwittingly feed their chicks with plastic resin pellets, believing they are fish eggs (Micalizio, 2019). Furthermore, seals, turtles, fish, and other fauna get entangled in abandoned fishing nets (Figure 1.1) with fatal consequences induced by starvation or drowning (a phenomenon referred to as 'ghost fishing').

Marine litter can also disrupt the food webs of ecosystems in the garbage patch. If accumulated into large patches at or near the sea surface, plastics may obstruct vital solar photons from reaching phytoplankton and algae below. Being among the most common types of autotrophs[2], these organisms are considered the bases of aquatic food cycles (Micalizio, 2019). A disturbance in their communities can therefore change the entire food web of the ecosystem. Animals with algae and phytoplankton as their main food source (e.g., fish and crustaceans) will decline in population, which in turn will lead to decreasing populations of apex predators (e.g., sharks and whales) as well as animals of all other trophic levels. Eventually, seafood becomes less accessible for humans,

1. Further research is necessary to thoroughly map risks to human health.
2. Autotrophs, or producers, are organisms that can produce their own nutrients using materials from inorganic sources, such as carbon and sunlight.

and some marine species may go extinct.

The vortex of the oceans makes the increasing issue of marine littering a borderless problem (Corbari et al., 2020). Although plastic pollution is considered a global issue, its occurrence in areas beyond national jurisdiction (e.g., the Great Pacific Garbage Patch) introduces the problematic matter of responsibility (Vince and Hardesty, 2017). According to a study conducted by The Ocean Cleanup and Deloitte, the annual costs related to marine plastic were estimated to be between 6 and 19 billion USD, calculated from loss of tourism revenue, impacts on fisheries and aquaculture, and governmental cleanup expeditions. These costs do not, however, include expenses related to human health and the negative impacts on marine ecosystems. In addition, most cleanup missions are not government-regulated, but rather conducted by nonprofit organisations whose funding comes from donations and private sponsors. The true annual cost of marine plastic pollution is thus unknown, but assumed to be much higher than initial estimates.

The key to solving the ongoing pollution crisis over time is believed to be prevention (NOAA, 2021). By stopping the problem at the source, cost-prohibitive cleanup initiatives can eventually become obsolete. Indeed, the world is not there yet, and cleanup vessels have yet many voyages to embark upon – of which satellite imagery may play a key role for efficient guidance and targeting in the future.

1.3 Objectives

The idea for this project was proposed by Kongsberg Satellite Services (KSAT) and is a further analysis of the satellite imagery acquired during their research and development study in the Great Pacific Garbage Patch in May–July 2020. The images were collected over areas of known plastic accumulation, and whilst no direct *in situ* measurements were taken, Global Positioning System (GPS) information related to four plastic conglomerates was available (an example of such a plastic aggregation is shown in Figure 1.2a). Positive tracker detections were confirmed in some of the images, which have been used as a baseline for understanding of the plastic features and their detectability.

The primary objective was to look for common features in the satellite imagery that could be used to detect marine plastic debris, and, if such evidence was found, explore whether the method could be adopted for use on other images. Although both synthetic aperture radar (SAR) and optical scenes were available for the study, early investigation of the SAR products yielded no immediate features of interest. Considering that, as well as time constraints, the

(a) (b)

Figure 1.2: Plastic debris collected in the Great Pacific Garbage Patch during a clean-up expedition in June 2020. Images are courtesy of Ocean Voyages Institute.

scope of the study was limited to the optical imagery with associated GPS tracker information, serving as a starting point for extracting marine plastic characteristics.

Exploration of the datasets required application of potential algorithms in a systematic manner. Through a rigorous literature review and interactive examination of the available imagery, it was decided to address the detection problem using a spectral approach. With the help of image analysis software and scientific coding environments, specific objectives included:

- Digitise GPS trackers into vectors and use linear interpolation to estimate their relative position at image acquisition time.
- Image pre-processing with suitable atmospheric correction algorithms, georeferencing, pan-sharpening, and cloud masking.
- Endmember extraction of plastic targets located by GPS information.
- Spectral analysis of extracted features and comparison to other ocean surface elements.
- Spectral unmixing for classification.
- Test effects of band ratios and spectral indices to enhance class distinction.

Ultimately, the aim of the study was to explore whether plastic detection was possible with the available data and with the strictly limited ground truth information. To the author's knowledge, no previous research has addressed the marine plastic detection problem using high-resolution commercial satellite

products in a real (i.e., no artificial, deployed targets) open ocean environment. Understanding marine plastic behaviour in remote areas, where it aggregates naturally, can contribute in making necessary steps towards fully automated detection schemes in the future.

1.4 Structure of Thesis

The thesis is divided into six chapters, including the introduction. Subsequent chapters and their main contents are organised as follows:

Chapter 2 reviews the concepts of remote sensing fundamentals and builds a theoretical basis of image analysis techniques needed to evaluate the main objective. Several algorithms are described in-depth to provide a full understanding of their functionality.

Chapter 3 introduces the datasets that were made available for the purpose of this study, in addition to giving a brief overview of the study area and how the Great Pacific Garbage Patch is formed.

Chapter 4 addresses the methodology of how the work of the thesis was conducted. It presents the application of pre-processing steps, feature extraction algorithms, and detection schemes, as well as the reasoning behind choices for further processing and analysis.

Chapter 5 presents the results obtained from exploring the datasets. The findings and their consistency with other literature are systematically discussed with respect to the main objectives.

Chapter 6 concludes the work presented in this thesis and makes suggestions to future work based on the findings and challenges encountered throughout the project.

All figures and illustrations presented in this thesis are either i) a product of own work; ii) republished with permission from the owner; or iii) licensed under a Creative Commons Attribution Licence granting noncommercial redistribution of published material. The source is clearly cited under each figure where the work of others has been borrowed.

2

Theory

2.1 Passive Remote Sensing

Remote sensing refers to the concept of obtaining information from the Earth's surface without being in physical contact with it. For passive remote sensing systems, this involves measuring energy that is naturally available in the form of either reflected or emitted solar energy. Most passive imaging satellites measure electromagnetic (EM) radiation within the range of reflected energy[1] and are thus only operative during the time of day when the Earth is illuminated by the sun. Despite this limitation, the abundance of different passive satellite instruments offers extreme versatility in terms of observation and detection capabilities. To fully understand the functionality of such systems, some fundamental knowledge of remote sensing and its physical concepts is necessary.

2.1.1 Electromagnetic Spectrum

Electromagnetic radiation is the means by which information is transferred from an object to a sensor. As illustrated in Figure 2.1, it consists of an electric and a magnetic force field of equal magnitude (i.e., energy) propagating perpendicularly as sinusoidal waves, where its properties are determined by the wavelength, or frequency, of the wave. Being inversely related, the wavelength

1. Roughly between 0.4 and 3 µm.

can be expressed by the frequency and vice versa:

$$\lambda = \frac{c}{\nu} \tag{2.1}$$

where λ denotes the wavelength [m], c is the speed of light in vacuum [m/s], and ν is the frequency [Hz].

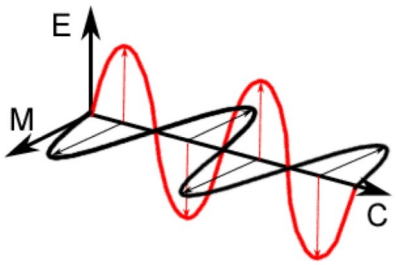

Figure 2.1: Electromagnetic radiation consists of an electric (E) and magnetic (M) field, oriented perpendicularly and propagating as waves at the speed of light[2] (CCRS, 2019).

The range of frequencies of EM radiation are referred to as the *electromagnetic spectrum*. Divided into a number of spectral regions (as seen in Figure 2.2), the total range extends from the longest radio waves to the shortest known cosmic rays. Each region of frequencies has distinct differences in wave-matter interaction; hence, remote sensing technologies utilise different parts of the spectrum depending on the application. For example, radar systems possess the ability to operate regardless of cloud cover due to the penetration capability of longer wavelengths, whereas shorter wavelengths (e.g., visible and infrared) will be reflected.

Electromagnetic energy is transported in units of photons – the smallest discrete quanta of electromagnetic radiation. In quantum mechanics, these elementary particles account for phenomena that occur when high-energy waves (i.e., short wavelengths) interact with matter, which can only be described by particle theory (Elachi and Zyl, 2006). As such, EM radiation is subject to a wave-particle duality that can be presented in a quantised form as bursts of radiation with photon energy, E, given by Planck's equation:

$$E = h\nu \tag{2.2}$$

where h is Planck's constant[3] and ν is wave frequency. As the frequency is directly proportional to the energy of the wave, remote sensing systems operating in longer wavelength regions of the spectrum must utilise wider bands to obtain a high-energy signal.

2. $c = 299,792,458$ m/s.
3. $h = 6.626 \times 10^{-34}$ Js.

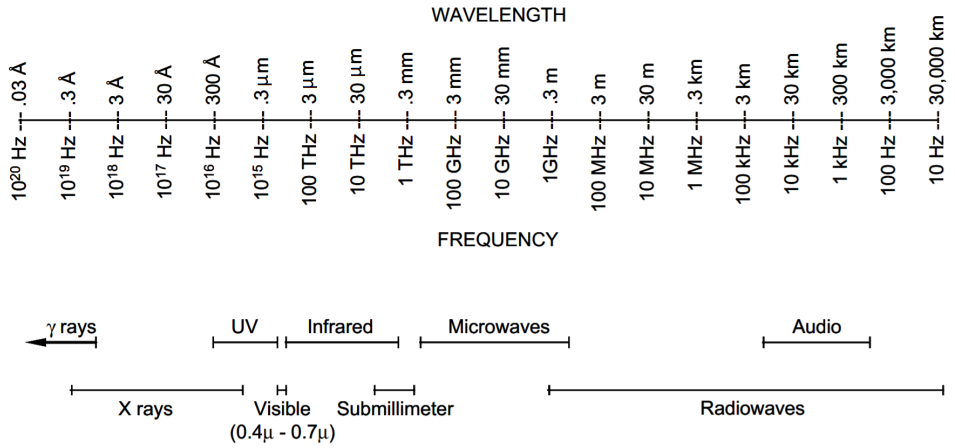

Figure 2.2: The electromagnetic spectrum. (Modified from Elachi and Zyl, 2006).

2.1.2 Basic Principles of Passive Imaging Systems

When an object is illuminated by an external source of EM radiation, three forms of wave-matter interaction are possible: absorption, reflection, and transmission (Lillesand et al., 2004). The type of interaction between the object and the incoming wave is determined by the wave frequency (thus, its energy) and the energy level structure of the material. Following the law of conservation of energy, the incident radiation can be decomposed as

$$E_I(\lambda) = E_A(\lambda) + E_R(\lambda) + E_T(\lambda) \tag{2.3}$$

where E_I is the incident wave energy of wavelength λ and E_A, E_R, and E_T denote the absorbed, reflected, and transmitted energies, respectively. If a photon's energy (Eq. 2.2) perfectly matches or is higher than the energy levels of the medium, the energy will get absorbed by its electrons. Conversely, for lower-energy waves that do not correspond to any of the medium's energy steps, the light can either heat the object, or, depending on the geometry and dielectric properties of the matter, reflect[4] off its surface (Elachi and Zyl, 2006).

In passive imaging systems, the source of electromagnetic radiation is the Sun, and the signal received by the sensor is reflected light from the surface. With an effective surface temperature of almost 5800 degrees Kelvin, the Sun is considered an ideal source (called a blackbody) in thermal equilibrium, with an emission spectrum described by Planck's radiation law:

$$S(\lambda, T) = \frac{2\pi hc^2}{\lambda^5} \frac{1}{e^{ch/\lambda kT} - 1} \tag{2.4}$$

4. Reflection of light typically occurs as a mix of the specular direction (mirror-like reflection) and uniform scattering in all directions.

where S represents the spectral radiance, h is Planck's constant, k is the Boltzmann constant[5], c is the speed of light, λ is the wavelength, and T is the absolute temperature in degrees Kelvin (Elachi and Zyl, 2006). Although the atmosphere is opaque to certain wavelength regions (e.g., gamma rays, X-rays, ultraviolet, and much of the infrared spectrum), objects on the Earth's surface are illuminated by light across large portions of the spectrum, from which it absorbs and reflects the different incident wavelengths based on its inherent energy levels. This principle is exploited in optical remote sensing, where reflected waves from the visible, near-infrared (NIR), and short-wave infrared (SWIR) are recorded in bands of varying wavelength ranges and used to form images with a spectral depth equal to the number of bands. This way, the reflectance properties of a certain material can reveal a characteristic spectral response, as illustrated in Figure 2.3, which can be used for identification, classification, or other image analysis.

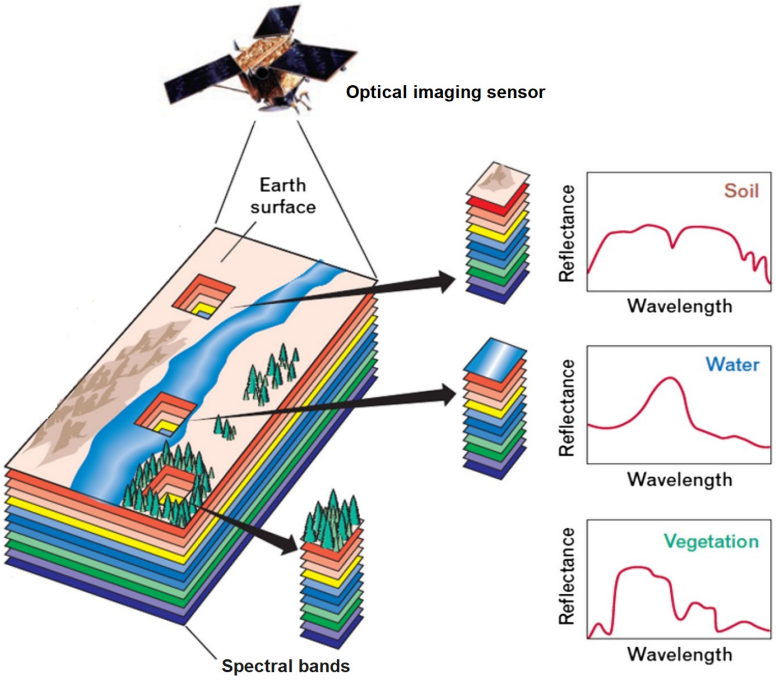

Figure 2.3: Recording the reflectance at different ranges of wavelengths (bands) reveals characteristic spectral shapes of each surface material. (Figure modified from Bhatt and Joshi, 2016).

5. $k = 1.381 \times 10^{-23}$

2.1.3 Remote Sensing Resolutions

There are four primary types of resolution related to satellite imagery: spectral, spatial, radiometric, and temporal. The spectral resolution is related to the number of bands in an imaging sensor, as illustrated in Figure 2.3, as well as to the bandwidth of these channels. The sampling rate and electromagnetic range over which a single band records surface-reflected radiance determine the spectral information content that can be derived from the scene, where a high spectral resolution is recognised by a narrow bandwidth and many spectral bands. For remote sensing instruments, hyperspectral sensors represent those of very high spectral resolution, capable of providing a nearly continuous spectrum for each image pixel using bandwidths of about 5–10 nm (Martínez-Vicente et al., 2019).

Fine spectral resolution is limited in space, and usually, there is a trade-off between spectral and spatial resolution. When an imaging sensor records electromagnetic energy at very narrow spectral ranges, it must compensate for the low-magnitude signal by recording over a larger surface area. The spatial resolution refers to this ground extent that corresponds to each pixel in the image and is a measure of the smallest object size that can be resolved by the sensor (Liang et al., 2012). In the field of marine debris detection, a very high spatial resolution is generally required to identify the material's low size distributions. However, commercial imagery is limited to resolutions of 25–50 cm (while only military satellite technology can achieve higher resolutions), restricting their utility to metre-sized objects in spatial analyses (Maximenko et al., 2019). The effects of spatial resolution are visualised in Figure 2.4.

Radiometric resolution, or dynamic range, describes the sensitivity of the imaging sensor to detect slight differences in electromagnetic energy, specifically, radiant flux[6]. Measured in bits[7], the radiometric properties determine the maximum number of integers in which pixel values of a single-band image are encoded. Evidently, more nuances and subtle changes in energy can be derived from an image of fine radiometric resolution, albeit with an increasing demand for storage capacity.

Finally, the temporal resolution refers to the frequency at which a sensor can record subsequent imagery of a particular area. The revisit frequency is affected by several different satellite characteristics, including its swath width, latitude, sensor agility[8], and type of orbit. In optical systems, persistent cloud cover can

6. Emitted or reflected radiant energy per unit time.
7. A number to the exponential power of 2.
8. A sensor's ability of observing the same area outside its ground trace between different satellite passes.

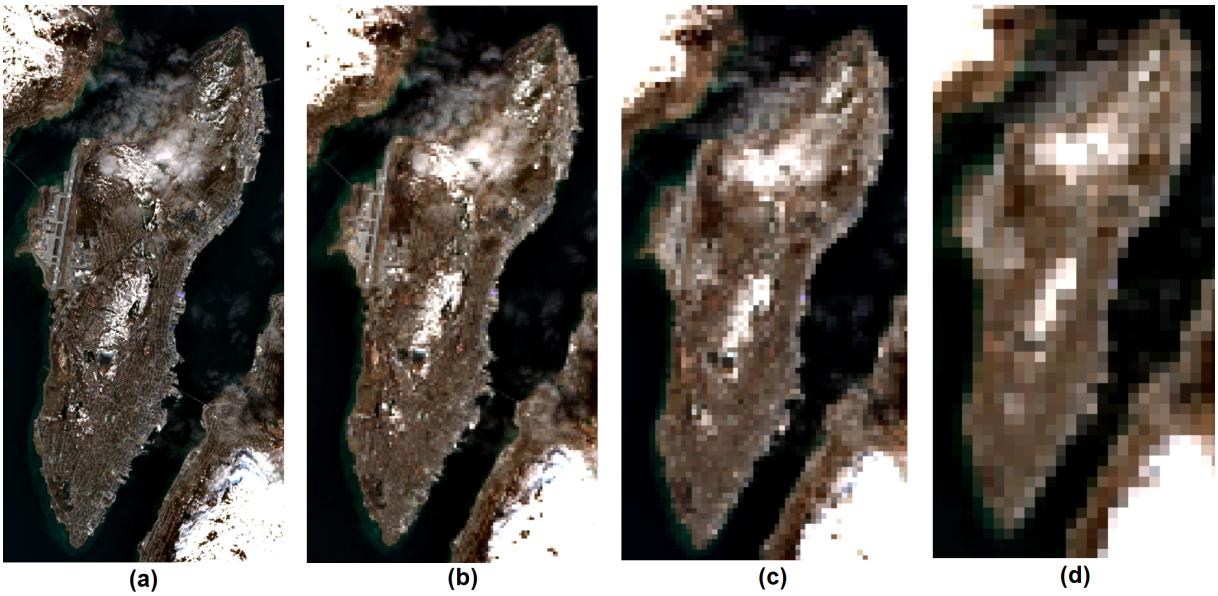

Figure 2.4: RGB composite showing the island of Tromsø, Norway, with spatial resolutions of (**a**) 10 m (native resolution), (**b**) 50 m, (**c**), 100 m, and (**d**) 200 m. The image is a Sentinel-2B product gathered from the Copernicus Open Access Hub (provided by the European Space Agency).

substantially extend revisit times, increasing the importance of sensor agility - particularly in tropical regions.

2.2 Linear Interpolation

Linear interpolation is a technique for estimating new data points within the range of a discrete set of known points. In the simplest case, two known coordinates, (x_0, y_0) and (x_1, y_1), are used to estimate the position of a third point, (x, y), located on a straight line joining the two known data points (Bayen and Siauw, 2015). For a value x contained within the interval (x_0, x_1), the position of y can be found from the slope equation,

$$\frac{y - y_0}{x - x_0} = \frac{y_1 - y_0}{x_1 - x_0}, \tag{2.5}$$

derived from Figure 2.5. Rearranging Equation (2.5) gives the formula for linear interpolation:

$$y = y_0 + (x - x_0)\frac{y_1 - y_0}{x_1 - x_0} = \frac{y_0(x_1 - x) + y_1(x - x_0)}{x_1 - x_0}, \tag{2.6}$$

where y is the unknown value at x.

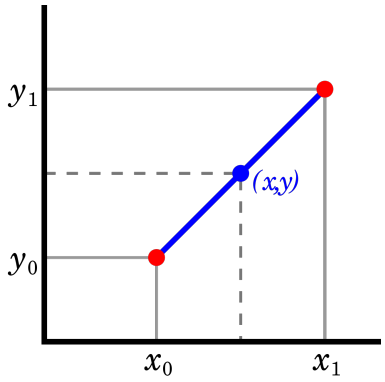

Figure 2.5: Given two known data points, (x_0, y_0) and (x_1, y_1), the position of y at a value of x can be estimated from linear interpolation.

This method can be adopted to pinpoint the estimated position of a GPS-tracker where two or more tracker positions have been recorded. For coordinates given in decimal degrees, the location of a point between consecutive tracker positions at a certain time t can be calculated by the equations

$$\text{lat}_{\text{est}} = \text{lat}_{\text{start}} + t\frac{\Delta\text{lat}}{\Delta t} \tag{2.7}$$

$$\text{lon}_{\text{est}} = \text{lon}_{\text{start}} + t\frac{\Delta\text{lon}}{\Delta t} \tag{2.8}$$

where $\text{lat}_{\text{start}}$ and $\text{lon}_{\text{start}}$ are the latitude and longitude coordinates at $t = 0$ respectively, Δlat and Δlon are the differences in latitude and longitude decimal degrees between consecutive tracker information, Δt is the time elapsed between the two GPS-tracker recordings, and t is time in seconds between starting position and the point that is to be estimated. Using Equations (2.7) and (2.8), an approximate position of the GPS-tracked plastic conglomerates can be estimated.

Interestingly, the temporal linear interpolation described by Equation 2.6 and Figure 2.5 depict the exact same mathematics as the linear mixture model, in which t represents the mixing parameter. These concepts are further explained in Section 2.6.

2.3 Image Pre-processing

Image pre-processing operations are intended to correct for sensor- and platform-specific radiometric and geometric distortions of the recorded data (CCRS, 2019). Basic radiometric and geometric corrections (e.g., for sensor noise and

viewing geometry) are usually performed by the image provider; however, depending on the product level of the imagery and the image application, further rectification steps may be applied. Additionally, to facilitate comparison between data, it may be desirable to calibrate the imagery to known units of (absolute) radiation or reflectance.

2.3.1 Atmospheric Correction

Atmospheric correction (AC) is the process of removing atmospheric effects on the reflectance values in satellite imagery (illustrated in Figure 2.6). Ideally, the derived bottom-of-atmosphere (BOA) reflectance spectra should match the same spectral response as if retrieved by a sensor at ground level. However, since atmospheric effects in optical remote sensing are both significant and complex, differences in BOA reflectance can vary substantially between AC algorithms (Topouzelis et al., 2020). Radiative transfer through the atmosphere is heavily influenced by absorption and scattering[9] processes caused by gas molecules and aerosols, and because these effects are variable, removal is necessary to allow for intercomparison across imagery of different sensors.

Figure 2.6: Before (left) and after (right) atmospheric correction of a Landsat-8 image of Venice, Italy, by the NASA-developed LEDAPS correction scheme. Image courtesy of Mapbox (2013).

9. Based on the wavelength of incident radiant energy and the size of the scattering particle, three types of scattering processes are recognised: Rayleigh (diameter $<< \lambda$), Mie (diameter $\sim \lambda$), and nonselective (diameter $>> \lambda$).

Atmospheric correction of high-resolution multispectral (MS) imagery is challenging, particularly in vast open ocean scenes (Vanhellemont and Ruddick, 2018). It is estimated that about 90% of the total signal measured by the sensor originates from atmospheric effects, while the water-leaving radiance only contributes <10% (Huang et al., 2019). Generally, it is beneficial for any detection task to remove the major effects of the atmosphere and extract the minor water signal in its purity, but uncertainties introduced in the various atmospheric correction schemes should be addressed to determine their reliability. Additionally, not all AC models provide spectral and aerosol information in the remote parts of the world oceans (e.g., the North Pacific Ocean). In this study, three AC algorithms have been explored for the purpose of retrieving at-surface reflectance values; FLAASH, ACOLITE, and ACOMP; which are further introduced in the sequel.

FLAASH

Fast Line-of-sight Atmospheric Analysis of Spectral Hypercubes (FLAASH) is a MODTRAN5[10]-based atmospheric correction algorithm suitable for most hyperspectral and multispectral sensors with bands in the visible, NIR, and SWIR regions of the electromagnetic spectrum (Harris Geospatial Solutions, 2020). The input file to the algorithm must be in floating-point at-sensor radiance units of $\mu W/cm^2 \cdot nm \cdot sr$, which can be computed from the equation

$$L_\lambda = (Gain \cdot q_{\text{pixel,band}} + Offset) \cdot \text{scale factor} \tag{2.9}$$

where gain- and offset values are calibration coefficients provided within the image metadata, $q_{\text{pixel,band}}$ is the pixel digital number of a certain band, and L_λ is the top-of-atmosphere (TOA) radiance. The scale factor must be found so that L_λ is in units of $\mu W/cm^2 \cdot nm \cdot sr$. After applying Equation (2.9) to the image DN data, FLAASH starts by using a standard equation for the radiance at a sensor pixel, L, to apply the solar wavelength range and Lambertian surface model[11] (ITT Visual Information Solutions, 2009). The equation is given as

$$L = \left(\frac{A\rho}{1 - \rho_e S}\right) + \left(\frac{B\rho_e}{1 - \rho_e S}\right) + L_a \tag{2.10}$$

10. MODTRAN (MODerate resolution atmospheric TRANsmission) is a computer code for modelling of atmospheric propagation of electromagnetic radiation in the spectral range of 0.2-100 µm.
11. A Lambertian surface or material appears uniformly bright regardless of an observer's angle of view.

where:

L is the radiance at a sensor pixel

ρ is the pixel surface reflectance

ρ_e is the mean surface reflectance for the pixel and a surrounding region

L_a is the radiance backscattered by the atmosphere

S is the spherical albedo of the atmosphere

A and B are coefficients related to atmospheric and geometric conditions, independent of surface characteristics

All variables are dependant on the waveband, and Equation (2.10) must accordingly be applied onto each spectral channel in the image. The distinction between the first and second term is that the latter corresponds to radiance coming from the surface and being scattered by the atmosphere into the sensor, while the first represents surface reflected radiance that travels directly into the sensor. The different values of ρ and ρ_e are employed to account for spatial mixing of radiance in nearby pixels, which is caused by atmospheric scattering (ITT Visual Information Solutions, 2009).

The values for A, B, S, and L_a strongly depend on the scene's water vapour column amount, which is generally not known and varies across a scene. The water vapour cannot be accurately retrieved without a dedicated water band (~1130 nm and <15 nm spectral resolution), which are only found in hyperspectral instruments. Thus, for FLAASH processing of MS imagery, the water vapour column amount is estimated using MODTRAN5 that operates the viewing and solar angles and the average surface elevation of the sensor through the assumption of an atmospheric model, aerosol type, and visible range (Jawak et al., 2019). The unknown parameters are then calculated using a MODTRAN radiation transfer code, which yields a unique solution for each image.

Finally, with the modelled water vapour, Equation (2.10) can be solved for the surface reflectance for each pixel in all of the sensor's spectral bands. As part of the solution, a spatially averaged radiance image L_e is computed from the equation

$$L_e \approx \left(\frac{(A+B)\rho_e}{1-\rho_e S} + L_a \right), \tag{2.11}$$

also referred to as the radiative transfer equation, from which the spatially averaged surface reflectance ρ_e can be estimated (ITT Visual Information Solutions, 2009).

Although FLAASH includes a method for aerosol retrieval, this was not used for the purpose of this study, as the available image data do not contain appropriate

aerosol bands.

ACOLITE

ACOLITE is a generic atmospheric correction processor developed for aquatic applications of satellite imagery[12]. The Dark Spectrum Fitting (DSF) algorithm, first presented in Vanhellemont and Ruddick (2018), was selected for this study based on its previously demonstrated success in marine environments (Topouzelis et al., 2019; Biermann et al., 2020). Although it generally performs best for optically complex waters (e.g., coastal and inland turbid waters), reasonable success is also achieved over open ocean (Vanhellemont, 2020). The algorithm is scene-based, requiring no previously defined 'black-pixel band'[13] such as NIR or SWIR. Instead, using the DSF method, the darkest pixels are dynamically selected based on various dark targets in the scene (Biermann et al., 2020). In-depth derivation of the scheme is beyond the scope of this study, and a detailed description is given in Vanhellemont and Ruddick (2018).

ACOMP

ACOMP (Atmospheric COMPensation) is an image processing algorithm developed by Maxar Technologies for atmospherically correcting WorldView and GeoEye imagery[14]. The correction scheme is not publicly available, which means that ACOMP imagery must be purchased directly from Maxar (or one of their certified resellers). Although the processing is strictly limited to only a few types of satellite sensors[15], the algorithm is rigorously tested and offers robustness even across the vast Pacific Ocean, according to Maxar. By providing an accurate estimate of the haze, aerosol, and water vapour amount, their scattering effects can be mitigated from the scene. The resulting satellite imagery can be used for intercomparison and analysis over diverse atmospheric conditions and across multiple sensor types (Maxar Technologies, 2020).

While all AC products offer values of surface reflectance without the oceanic and atmospheric components, the scaling of pixel values can vary and therefore

12. Originally developed for Landsat (5/7/8) and Sentinel-2 (A/B) imagery but is now hosting support for many other multispectral sensors as well.
13. The 'black-pixel' assumption is utilised in several other maritime AC schemes, in which a NIR or SWIR band's pixel values are considered to be zero because of the strong absorption of the water itself.
14. The WorldView and GeoEye series of satellites are owned by Maxar Technologies.
15. WorldView-1/-2/-3, GeoEye-1.

challenge a comparison with other images. For most ACOMP products[16], the imagery is delivered with an 11-bit radiometric resolution - giving a possible range of pixel values from 0 to 2047. Hence, to convert the image to units of fractional reflectance (from 0 to 1.0), one must divide each pixel in each band by 2048.

2.3.2 Pan-sharpening

Pan-sharpening is a useful technique for improving visual image interpretation. By utilising a multiband raster and a higher-resolution panchromatic band (of the same scene), a pan-sharpened image can be created as a fusion of the two. The radiometrically transformed image combines the spatial information of the pan-band with the spectral information of the multiband data. While many different pan-sharpening techniques are available, the Gram-Schmidt spectral sharpening method was chosen for this study because of its (generally) high spectral accuracy (Harris Geospatial Solutions, 2020). However, spectral values will always be altered in the pan-sharpening process, and hence, the imagery should only be used in spatial analyses.

The Gram-Schmidt technique, patented in Laben and Brower (2000), is based on a general algorithm for vector orthogonalisation in which each band of an image corresponds to a high-dimensional vector (the number of image pixels equals the number of vector dimensions). In the ENVI software, the algorithm is performed in four discrete steps. First, a panchromatic band is simulated from the lower-resolution multispectral bands by computing their weighted average. Next, the simulated pan-band and the original spectral bands are decorrelated through the Gram-Schmidt orthogonalisation method, treating each band as a multidimensional vector and using the simulated low-resolution panchromatic band as the first band (i.e., nontransformed). The high-resolution panchromatic band is then inserted as replacement of the first Gram-Schmidt band (simulated pan-band), and finally, the inverse Gram-Schmidt transform is applied to form the pan-sharpened multiband image.

2.3.3 Orthorectification

Orthorectification is the process of removing the effects of relief (terrain) and image perspective (tilt) displacements to create a planimetrically correct image. The orthorectification process usually requires a geometric model, a digital elevation model (DEM), and ground control points (GCPs), but if the Rational

16. The exception being WorldView-3 multispectral imagery ordered along with eight-band SWIR. In this case, pixels are scaled with a 1/10000 ratio.

Polynomial Coefficient (RPC) model is used, the latter can be omitted (Cheng and Chuck, 2010). This makes RPC orthorectification one of the most popular methods when working with high-resolution imagery, particularly in aquatic scenes where GCPs are unobtainable.

RPCs are a type of sensor model in which the physical relationship between image coordinates (i, j) and ground coordinates (x, y, z) are mapped using a mathematical transform. The sensor models are unique to each sensor, and the accuracy of the orthorectification depends on the accuracy of the given sensor model, as well as the quality of the image. Using a third-order rational polynomial of the form

$$(i, j) = f(x, y, z), \tag{2.12}$$

the two-dimensional image points are related to the corresponding longitude (x), latitude (y), and elevation (z) on the ground (Harris Geospatial Solutions, 2020). Many commercial high-resolution products include pre-computed RPCs within the imagery metadata (e.g., WorldView-2/-3) that allows georeferencing to a standard spatial reference via the RPC method. For optimal accuracy of the transformation, a high-resolution DEM should be used for the orthorectification process with a spatial extent matching that of the input raster.

2.4 Image Analysis

To take advantage of the vast opportunities enabled by remote sensing, meaningful information must be extracted from the data through interpretation and analysis. In this study, various techniques exploiting the spectral characteristics of plastic targets have been evaluated.

2.4.1 Noise Level Estimation

Image noise can be explained as random variation of brightness or colour information in image pixels (Jeon et al., 2012). Generally, these defects arise from electronic noise generated by the sensor and its circuitry or by shot noise (Poisson noise). Any noise resulting from image acquisition is an undesirable artefact that adds spurious information to the imagery. Typically, noise level information is provided by the noise standard deviation, and in optical satellite sensing, the noise level for each band can be computed as the pixels' mean value divided by their standard deviation, i.e., the signal-to-noise ratio (SNR):

$$\mathrm{SNR} = \frac{\mu_{ij}}{\sigma_{ij}} \tag{2.13}$$

where i and j represent the rows and columns of the image, respectively, μ_{ij} is the pixel mean, and σ_{ij} is the standard deviation. The SNR is often reported using the logarithmic decibel (dB) scale, which can be expressed through

$$\text{SNR}_{dB} = 20\log_{10}(\text{SNR}) \tag{2.14}$$

Because the mean and standard deviation represent measures of amplitude (as opposed to units of power), the factor is 20 instead of the conventional factor of 10. The SNR of remote sensing imagery should be investigated to evaluate its impact on the optimal functioning of the image processing pipeline (Jeon et al., 2012), as the image information content is reduced in line with signal noise corruption.

2.4.2 Classification

Classification of images involves applying a set of rules to extract information classes from a multiband raster image. By identifying similar characteristics in different pixels, the total data space can be divided into several subsets separated by decision boundaries[17]. The pixels that fall within the volume created by such boundaries are then classified as belonging to one specific class (Elachi and Zyl, 2006). An abundance of classification criteria exist, ranging from simple Euclidean distance measures to complex neural network schemes, and performance of a certain algorithm depends heavily on the nature of the input data.

In general, we separate between two major approaches for image classification: supervised and unsupervised. Both techniques, as well as two type-specific algorithms, are explained in the following sections.

Supervised Classification

Supervised classification involves the mapping and classification of image pixels by comparison to training feature vectors selected by the image analyst. These regions of interest represent homogeneous samples of different surface cover types and can be envisioned as vectors defining the centroids of the decision volumes that are separated by the decision boundaries (Elachi and Zyl, 2006).

In this study, the *Spectral Angle Mapper* (SAM) algorithm (Kruse et al., 1993) has been tested for its mapping capabilities of marine plastic. This physically-based

17. A region of a multidimensional space that separates input data from other classes.

spectral classification method uses an n-dimensional angle α to match image pixels to reference spectra, where n corresponds to the number of available spectral bands. To determine spectral similarity between a reference spectrum r and an image pixel spectrum t, the following equation is employed:

$$\alpha = \cos^{-1}\left(\frac{\sum_{i=1}^{n} t_i r_i}{\left(\sum_{i=1}^{n} t_i^2\right)^{1/2}\left(\sum_{i=1}^{n} r_i^2\right)^{1/2}}\right) \tag{2.15}$$

Smaller angles represent closer resemblance to the reference spectrum, and pixels are assigned to the class exhibiting the smallest spectral angle α (Weyermann et al., 2009). As illustrated by the simple example in Figure 2.7, each pixel can be regarded as a vector in an n-dimensional feature space with a given length and direction. SAM calculations (Eq. (2.15)) only consider the vector's direction, however, meaning that its length does not impact the spectral angle result. Consequently, SAM is relatively insensitive to variations in total illumination intensity across the scene, albeit only for linear, multiplicative differences between spectra.

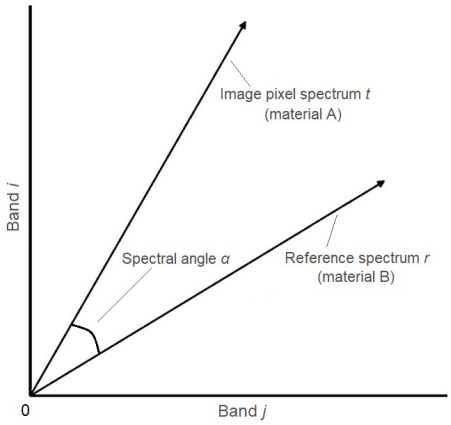

Figure 2.7: Two-dimensional illustration on the concept of Spectral Angle Mapper classification.

Pre-determined angle thresholds can be set to ensure a certain level of spectral similarity in assigned class pixels. Theoretically, any arbitrary pixel can be classified to a given class if its allowed spectral angle is chosen large enough (Weyermann et al., 2009). The threshold should therefore be defined so that the reference spectrum is allowed inherent class variation, neglecting differences induced by viewing geometry or other anisotropy, while still excluding other classes with similar spectral characteristics.

Unsupervised Classification

Unsupervised classification is the process of clustering pixels in an image based on statistics only, without the need for defining training areas. The pixels are classified solely based on the numerical information in each of the image's spectral bands (i.e., feature space) and grouped together based on similarity in spectral response. Thus, no extensive prior knowledge of the scene is required, but classes must be manually identified after the classification process (HSU, 2014).

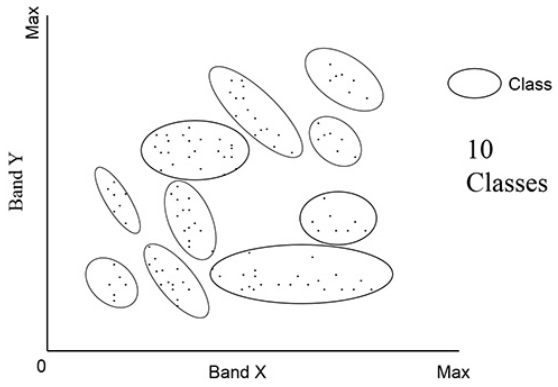

Figure 2.8: Result of an unsupervised classification using two spectral bands and ten classes/clusters. Illustration courtesy of Humboldt State University.

ENVI has two built-in methods for unsupervised classification: *K-Means clustering* and the *Iterative Self-Organizing Data Analysis Technique* (ISODATA). Although the two methods are very similar, the latter has been used for this project. Both K-means and ISODATA are hard clustering algorithms, meaning that each data point (i.e., pixel in image classification) belongs exclusively to a single class or cluster. The assumption is thus that the membership coefficients u_{ij} are either one or zero: 1 for the class C_j of which it belongs to and zero for all other classes, C_k, where $k \neq j$ (Koutroumbas and Theodoridis, 2009). That is,

$$u_{ij} \in 0, 1, \quad j = 1, ..., m \tag{2.16}$$

and

$$\sum_{j=1}^{m} u_{ij} = 1 \tag{2.17}$$

The aim is now to minimise the *cost function*[18], given as

$$J(\boldsymbol{\theta}, U) = \sum_{i=1}^{N} \sum_{j=1}^{m} u_{ij} d(\boldsymbol{x}_i, \boldsymbol{\theta}_j) \tag{2.18}$$

18. A function of an optimisation problem that measures the performance of a classification model for given data.

where N is the number of data points, m is the number of clusters, and $d(\boldsymbol{x}_i, \boldsymbol{\theta}_j)$ is a minimum distance measure between a data vector $\boldsymbol{x}_i$, representing a single pixel, and the unknown parameter vector $\boldsymbol{\theta}_j$. This cost function can be minimised by assigning each $\boldsymbol{x}_i$ to its closest cluster, i.e., the shortest distance as determined by $d(\boldsymbol{x}_i, \boldsymbol{\theta}_j)$. For the ISODATA and K-Means algorithm, this distance measure is the squared Euclidean distance. Thus, Equation (2.18) becomes

$$J(\boldsymbol{\theta}, U) = \sum_{i=1}^{N} \sum_{j=1}^{m} u_{ij} \|\boldsymbol{x}_i - \boldsymbol{\theta}_j\|^2 \tag{2.19}$$

The parameter representative $\boldsymbol{\theta}_j(0)$ is arbitrarily chosen for the first iteration. Thereafter, the updating of vectors $\boldsymbol{\theta}_j$ follow the equation

$$\sum_{i=1}^{N} u_{ij} \frac{\partial d(\boldsymbol{x}_i, \boldsymbol{\theta}_j)}{\partial \boldsymbol{\theta}_j} = 0, \quad j = 1, ..., m \tag{2.20}$$

As a consequence of the choice of distance measure in Equation (2.19), Equation (2.20) yields that $\boldsymbol{\theta}_j$ is the mean vector of the jth class (Koutroumbas and Theodoridis, 2009). A number of m classes must be requested by the user, and pixels are iteratively classified to the closest cluster relative to the current class mean, $\boldsymbol{\theta}_j$. ISODATA unsupervised classification differs from K-Means by not having a fixed number of classes, meaning that classes can be split, merged, and deleted throughout the iteration process based on input threshold parameters (Harris Geospatial Solutions, 2020). Unless a standard deviation or distance threshold is specified, all pixels will be classified to the nearest cluster. The algorithm recovers classes with as low variability in pixels as possible and converges to a minimum of the cost function when either the number of pixels in each class changes by less than a predetermined change threshold or the maximum number of iterations is reached (Harris Geospatial Solutions, 2020).

2.4.3 Spectral Indices

A spectral index is a mathematical expression that is applied per pixel on two or more spectral bands of an image. Numerous such indices exist, each designed to enhance certain properties of a scene's surface, with many being functionally equivalent. The basic idea is to utilise the spectral response of a target material by identifying channels or wavelength ranges that have unique reflectance and absorption[19] features relative to surrounding materials. For plastics, a spectral peak is shown in the near-infrared (Kornei, 2019), with other significant spectral features in the shortwave infrared (Martínez-Vicente et al.,

19. Wavelengths that show very low reflectance in a material.

2019). The ocean, however, is a dark target that strongly absorbs wavelengths in the NIR and SWIR spectra (Maximenko et al., 2019; Biermann et al., 2020), and, compared to plastics and other floating materials, exhibit overall lower reflectance in these wavelength ranges. Accordingly, an index that makes use of NIR and SWIR bands could be appropriate for marine plastic detection.

Many spectral indices require the input bands to be in units of scaled surface reflectance (0 to 1.0) as the equations contain numerical constants that are typically determined using reflectance data. However, for expressions without such constants, it is possible to apply the index onto pixel values of top-of-atmosphere reflectance or even radiance. This way, possible errors arising from the atmospheric correction process can be mitigated (Garaba et al., 2018). The results of such an approach should be evaluated independently, however, and not be directly compared to that of BOA reflectance data. For a rigorously tested index, predetermined numerical ranges associated with certain surface cover types may change depending on the input data, and an individual assessment of results will be needed.

Normalised Difference Vegetation Index (NDVI)

The Normalised Difference Vegetation Index (NDVI), introduced by Rouse et al. in 1973, is a traditional method for mapping of vegetation in multispectral imagery. NDVI is defined as:

$$\text{NDVI} = \frac{R_{\text{NIR}} - R_{\text{RED}}}{R_{\text{NIR}} + R_{\text{RED}}} \tag{2.21}$$

where R_{NIR} and R_{RED} are the reflectance[20] in the near-infrared and red channels, respectively. The index is based on the fact that all forms of vegetation show an increase in reflectance spectra at around 700 nm (the "red edge") and into the NIR spectral range (Hu, 2009). The difference between reflectance values in the NIR and red bands serves as a measure of both vegetation density and photosynthetic capacity, where a high NDVI value indicates healthy and/or dense vegetation. For water, which is a strong absorber of NIR wavelengths, NDVI values are typically low to negative.

Figure 2.9 illustrates how the spectral signature of marine plastic debris exhibit an increased reflectance in the NIR region, similar to that of vegetation. However, the floating algae tends to have a significantly higher peak at NIR (Kikaki et al., 2020), making its NDVI values distinguishable from plastic. This was

20. While units of reflectance are most commonly used, the principle of NDVI will also work with radiance imagery.
21. A genus of brown macroalgae (seaweed; Phaeophyceae).

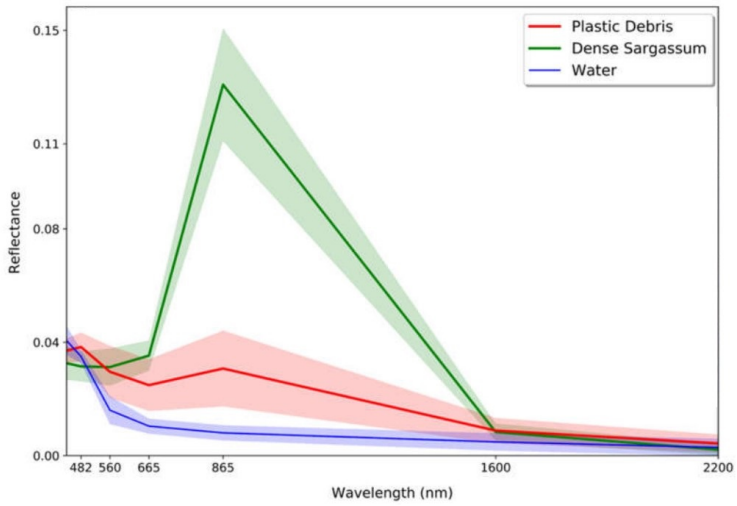

Figure 2.9: Spectral signatures of plastic debris (red), dense *Sargassum*[21] (green), and seawater (blue), derived from ACOLITE corrected Landsat-8 and Sentinel-2 imagery. Republished with permission from Kikaki et al., 2020.

demonstrated in Biermann et al. (2020), where marine plastics were shown to occupy distinct NDVI ranges that do not overlap with seawater, seaweed, sea foam, pumice, and floating wood.

2.4.4 Anomaly Detection

Anomaly detection is the process of identifying samples that do not conform to the expected pattern of the data. In the case of high-resolution satellite imagery, it refers to the problem of detecting image pixels with spectra that significantly differ from a common background spectrum. The most widely employed algorithm for this purpose, which has also been applied in this study, is the Reed-Xiaoli Detector (RXD) developed by Reed and Yu (1990). Grouped with other covariance-based anomaly detectors, the RXD algorithm can extract small targets that are spectrally distinct from other image pixels of a given region, but the anomalous feature(s) must be sufficiently compact relative to the background for the method to function properly.

The RXD algorithm works in the following way: First, we consider an image $\mathbf{X} = [\mathbf{x}_1\mathbf{x}_2...\mathbf{x}_N]$ consisting of N pixels, whose column vectors $\mathbf{x}_i = [x_{i1}x_{i2}...x_{im}]^T$ represent the ith pixel value of spectral band m. Estimated spectral behaviour of background pixels can then be expressed by their mean vector $\hat{\boldsymbol{\mu}}$ and covariance

matrix $\hat{\mathbf{\Sigma}}$, given as

$$\hat{\boldsymbol{\mu}} = \frac{1}{N}\sum_{i=1}^{N}\mathbf{x}_i \quad \text{and} \quad \hat{\mathbf{\Sigma}} = \frac{1}{N}\sum_{i=1}^{N}\overline{\mathbf{x}}_i\overline{\mathbf{x}}_i^T \tag{2.22}$$

where $\overline{\mathbf{x}}_i = (\mathbf{x}_i - \hat{\boldsymbol{\mu}})$. The mean and covariance estimates are computed from the full image (or a pre-determined subset) under the assumption that the vectors $\mathbf{x}_i$ are measurements of the same random process (Verdoja and Grangetto, 2020). For this to hold, the anomalous features must therefore be small enough to have negligible effects on the estimates.

The squared Mahalanobis distance is employed to compute the generalised likelihood of a pixel $\mathbf{x}$ being an anomaly with respect to the estimated covariance matrix. The likelihood is calculated as

$$\delta_{RXD}(\mathbf{x}) = \overline{\mathbf{x}}_i^T\hat{\mathbf{\Sigma}}^{-1}\overline{\mathbf{x}}_i \tag{2.23}$$

Usually, the results from Equation (2.23) are evaluated by a decision threshold η that automatically discards or confirms suspected anomaly targets. This can be done by choosing η adaptively as a percentage of the full dynamic range of δ_{RXD}, specifically:

$$\eta = t \cdot p \max_{i=1,\ldots,N}(\delta_{RXD}(\mathbf{x}_i)) \tag{2.24}$$

where $t \in [0, 1]$ and p is the number of spectral channels (same as m if a dimensionality reduction of the data is not performed). Thus, a pixel is regarded anomalous if $\delta_{RXD}(\mathbf{x}) \geq \eta$ (Verdoja and Grangetto, 2020).

2.5 Endmember Extraction

The detection of plastics in satellite imagery is often limited by the spatial resolution of the sensor. Even for metre-sized floating patches of plastic, the ground sampling distance (GSD) of most optical instruments is not high enough for plastics to fully cover a single pixel. Furthermore, floating plastics are likely to be wet with seawater and partially submerged, preventing a pure plastic spectrum to be directly derived from the image. To this date, no reference library spectra of marine plastic debris in a natural environment exist (Topouzelis et al., 2020), and, consequently, spectral information of plastics must be derived from the scene using appropriate endmember extraction methods. In this study, two such techniques have been explored: the Pixel Purity Index and an Inverse Spectral Unmixing calculation. The former is an automated algorithm designed to extract the most spectrally pure pixel signatures in a scene, while the latter requires prior knowledge about material abundance in a nonuniform pixel.

Regardless, the aim of the two approaches is the same: to locate and extract a pure plastic spectrum in an image that can be used to detect other potential plastic pixels via spectral unmixing and classification algorithms.

2.5.1 Endmembers

In most classification schemes, it is assumed that each pixel in an image belongs to one feature vector class only. But this is rarely the case for satellite imagery. Depending on the image spatial resolution, a single pixel can cover multiple different surface types that each have a different spectral response. Such pixels are referred to as *mixed pixels*, and their spectral signatures, as measured by the sensor, are made up of the weighted sum of all contributing surface element spectra, referred to as *endmembers* (Elachi and Zyl, 2006). The spectral response of an endmember represents a purely homogeneous pixel, covering only one type of surface component. In subpixel classification schemes, the measured spectrum of a mixed pixel, $S_{\text{total}}(\lambda)$, is fundamentally assumed to follow the linear mixture model equation:

$$S_{\text{total}}(\lambda) = \sum_{i=1}^{N} a_i S_{ei}(\lambda) + n \tag{2.25}$$

where a_i is the relative fraction of the measured spectrum contributed by the endmember spectrum $S_{ei}(\lambda)$, and n represents additive noise. Assuming that all endmember spectra in an image are known, and that all fractions must be positive, Equation (2.25) is constrained by

$$\sum_{i=1}^{N} a_i = 1; \quad a_i \geq 0 \tag{2.26}$$

In the ideal case, when Equation (2.26) holds and all coefficients in the linear combination sum up to 1, a_i is interpretable as cover fraction or abundance of a certain endmember. This is illustrated in Figure 2.10, showing a simple mixture model that has the geometrical shape of a triangle whose vertices are the endmembers. Cover fractions can then be determined by the position of spectral components in the two-dimensional data cloud and be considered relative coordinates in a new reference system defined by the endmembers (Plaza et al., 2002).

2.5.2 Pixel Purity Index

The Pixel Purity Index (PPI) is a tool originally developed for the ENVI software, which can be used to locate the purest pixels in a multi- or hyperspectral image.

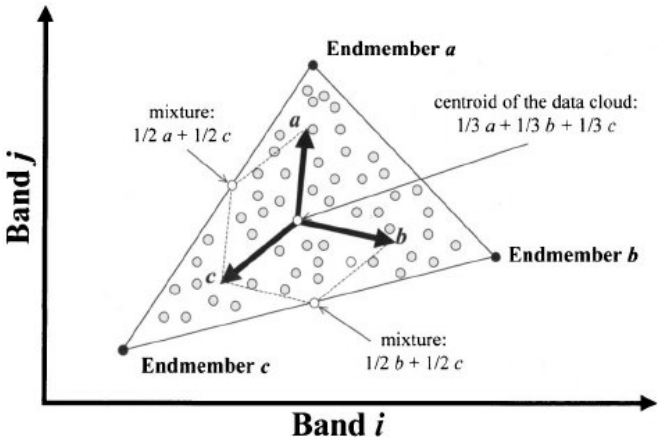

Figure 2.10: Scatterplot of two-dimensional spectral data points demonstrating the physical interpretation of a mixture model based on endmembers. Figure from Plaza et al. (2002).

The algorithm is based on the geometry of convex sets[22], where each pixel is considered a vector in n-dimensional feature space[23]. PPI starts by generating random unit vectors, or "skewers", constrained to pass through the centre – the mean value – of the n-dimensional data cloud. A random vector is then selected, onto which each pixel in the image is projected (as illustrated in Figure 2.11). The values of the projection are loaded into a histogram, where the most extreme pixels in the direction of the skewers fall into the tails of the histogram distribution and are considered spectrally pure. The threshold value of these histogram tails can be modified by the user but is typically two to three times the noise level in the data[24] (Harris Geospatial Solutions, 2020).

The PPI algorithm will iterate through a set number of iterations. Throughout the process, ENVI keeps track of how many times each pixel is marked as spectrally extreme for a single skewer – incrementing its value in the output PPI image by one for each time. When the algorithm reaches maximum iterations, it outputs a rule image of each pixel's PPI score. The resulting image can then be used to identify pixels with a high PPI value that are likely to be endmembers in the input scene.

To facilitate extraction of the endmembers, ENVI has a tool called n-D Visualiser to locate, identify, and cluster the most extreme spectral responses in an n-dimensional data cloud (Harris Geospatial Solutions, 2020). Using both the PPI

22. A convex set is a set of elements from a vector space such that all the points on the straight line between any two points of the set are also contained within the set.
23. *n* is the number of spectral channels in the image.
24. The noise level will be equal to one if using Minimum Noise Fraction (MNF) transformed data.

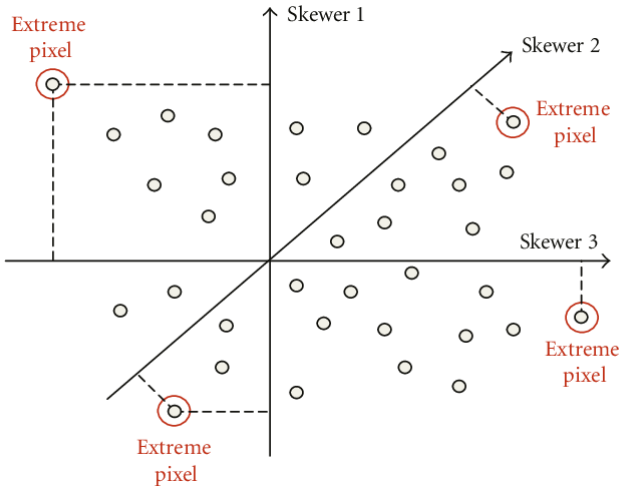

Figure 2.11: Simple example illustrating the performance of the PPI algorithm in a two-dimensional feature space. Figure from González et al. (2010).

image and the original scene as input, the n-D Visualiser allows for interactively rotating data in n-D space and manually or automatically selecting the purest pixels based on vertices in the data cloud. The resulting endmember signatures can be identified as belonging to a certain class through either visual inspection or comparison to reference library spectra, after which they can be used in classification schemes or spectral mixture analyses.

2.5.3 Inverse Spectral Unmixing

The inverse spectral unmixing approach involves a modification of Equation (2.25) describing a linear mixed model. It is not a typical method for endmember extraction, as it is, in its forward sense, used to decompose the spectral signature of a mixed pixel into a set of predetermined endmembers and corresponding abundances (Topouzelis et al., 2020). However, if the fractions of each endmember comprising the mixed pixel are known, a target's spectral response can be derived from inverse spectral unmixing provided it is the only unknown variable. That is, all other endmember spectra are known explicitly.

In the simplest case, a mixed pixel is composed of two different surface components. The mixed pixel can then be expressed as

$$S_{mix}(\lambda) = a_1 S_1(\lambda) + a_2 S_2(\lambda) \tag{2.27}$$

where a_1 and a_2 are the fractional coverage of the pixel's endmember spectra S_1 and S_2 for wavelength λ, respectively. The inverse spectral unmixing approach assumes that both abundances, as well as S_{mix} and one of the two endmember

signatures, are known. An estimation of the target's pure spectral response would then follow the equation:

$$S_1(\lambda) = \frac{S_{mix}(\lambda) - a_2 S_2(\lambda)}{a_1} \tag{2.28}$$

where S_1 is the unknown endmember spectrum calculated from the other known variables. Equation (2.28) is deterministic in the sense that it does not account for random noise in the channels, and hence, the result comes with an immeasurable level of uncertainty. Nevertheless, the technique is useful for extracting spectral responses of smaller targets without the need for a pure pixel.

2.6 Spectral Unmixing – Mixture Tuned Matched Filtering

Mixture Tuned Matched Filtering (MTMF), first described in Boardman (1998), is an advanced spectral unmixing algorithm designed to detect specific materials within mixed image pixels. Unlike linear spectral unmixing, MTMF does not require all materials or endmember spectra within a scene to be known; one target spectrum is sufficient. This makes the MTMF appropriate to use on multispectral imagery where not all endmember spectra can be resolved[25], despite the algorithm being originally developed for hyperspectral data.

The algorithm, illustrated in Figure 2.12, is designed to leverage mixing between a target of interest and the background in order to solve the problem of "selectivity" common to simpler methods (Boardman and Kruse, 2011). Through a partial unmixing calculation, the abundance of a user-defined endmember can be found by maximising the response of the endmember of interest and minimising the response of the composite unknown background (Mehr et al., 2013). MTMF is very effective for detecting small subpixel targets differing subtly from the background, and it also calculates an *infeasibility* image for each endmember allowing false positives to be rejected. The process of applying MTMF to an image can be divided into three main steps: i) Pre-processing and data conditioning, ii) Matched Filtering for abundance estimation, and iii) Mixture Tuning for false positive identification and rejection (Boardman and Kruse, 2011). All three steps are presented in detail in the following sections.

25. The number of spectral bands in a sensor determines the upper limit for the number of endmembers that can be derived from an image.

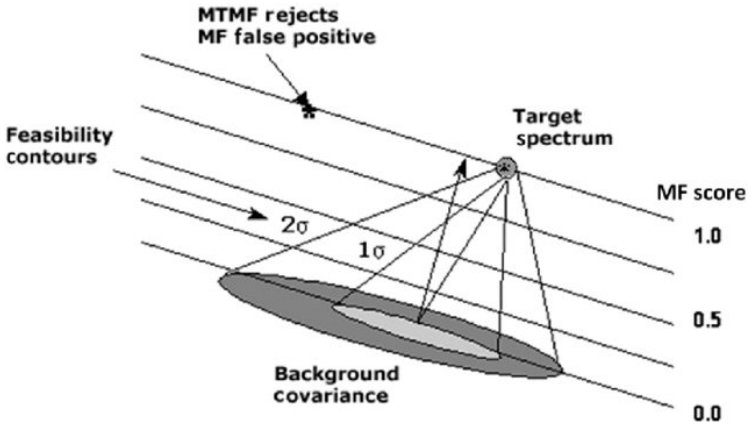

Figure 2.12: Concept of Mixture Tuned Matched Filtering showing identification and quantification of a known target spectrum against a diverse background. High MF scores indicate a large fraction of target spectrum within the pixel, where 1.0 equals a perfect match between the user-supplied endmember and pixel spectrum (i.e., 100% abundance). The infeasibility scores constrain the spectral profile in the context of mixing of the background and target signature. Consequently, the best spectral matches are identified by a high MF score and a low infeasibility score. Figure is made by F. A. Kruse (Kruse et al., 2015).

i) Pre-processing and Data Conditioning (MNF Transform)

The first step of MTMF is to apply a Minimum Noise Fraction (MNF) transform to the data. This process is twofold, comprising noise whitening[26] and data decorrelation, with the aim of segregating noise in multi- or hyperspectral imagery. To whiten the noise, the noise covariance matrix and its decomposition into a corresponding eigenvalue vector and eigenvector matrix must be estimated. This can be done in different ways, but for scenes without appropriate auxiliary data[27], the estimation must be done via the *shift difference* method (Boardman and Kruse, 2011). As described in Boardman and Kruse (2011), the shift difference leverages the fact that neighbouring pixels typically have a strong spatial correlation, while a much lower correlation is seen for noise. As a result, the difference between neighbouring pixels will primarily depict the noise.

Since the method derives noise statistics directly from the dataset, the input is the image itself. This is represented by a $r \times c \times b$ matrix, $\boldsymbol{D}$, whose dimensions are the rows, columns, and bands, respectively. The method proceeds to create

26. Noise whitening is the process of rescaling the noise in the data.
27. Other methods can be utilised if the scene has a dark current image or if noise statistics are known *a priori*.

a new matrix, $\boldsymbol{N}$, by calculating the differences between adjacent pixels for each band. $\boldsymbol{N}$ will then be a "noise-only" dataset of dimensions $r-1 \times c-1 \times b$, where every band correspond to the average row- and column shift difference of the same band in $\boldsymbol{D}$, i.e.:

$$\boldsymbol{N}_{ijk} = \frac{1}{2}\left(\boldsymbol{D}_{ijk} - \boldsymbol{D}_{(i-1)jk}\right) + \frac{1}{2}\left(\boldsymbol{D}_{ijk} - \boldsymbol{D}_{i(j-1)k}\right) \tag{2.29}$$

where i, j, and k represent row, column, and band indices, respectively (Boardman and Kruse, 2011). To calculate the covariance noise matrix, $\hat{\Sigma}_{\mathrm{n}}$, $\boldsymbol{N}$ is considered two-dimensional with dimensions $(r-1)(c-1) \times b$. $\hat{\Sigma}_{\mathrm{n}}$ is then estimated from the sample covariance, given as

$$\hat{\Sigma}_{ij} = 1.5\left(\frac{\sum\left(\boldsymbol{N}_{ki} - \bar{n}_i\right)\left(N_{kj} - \bar{n}_j\right)}{p-1}\right) \tag{2.30}$$

where p is the total number of pixels in the shift difference result $[(r-1)(c-1)]$, and $\bar{n}_i$ and $\bar{n}_j$ denote the mean value of band i and j of the noise image $\boldsymbol{N}$, respectively. The factor of 1.5 is added to account for the squaring of the terms in Equation (2.29)[28].

The next step in data pre-processing is decomposing $\hat{\Sigma}_{\mathrm{n}}$ into eigenvalues and eigenvectors. This is done by first reducing the covariance matrix to tridiagonal form[29] using Householder reflections[30], and then applying a diagonalisation via QL factorisation[31]. Next, the eigenvalues and corresponding eigenvectors are sorted in descending order. The final results of the decomposition are the noise eigenvalue vector $\boldsymbol{\Lambda}_{\mathrm{n}}$ and the noise eigenvector matrix $\boldsymbol{E}_{\mathrm{n}}$ (Boardman and Kruse, 2011).

Following this, the original image is mean corrected by subtracting the average spectrum $\bar{S}$ from the data. Then, to decorrelate the noise, the mean-corrected image is projected onto $\boldsymbol{E}_{\mathrm{n}}$. Finally, each resulting band is normalised by dividing it by the square root of the corresponding noise eigenvalue, producing a noise-whitened image of zero mean. This transformation is referred to as Principal Component Analysis (PCA) whitening, conducted using the PCA whitening matrix:

$$\boldsymbol{W} = \boldsymbol{E}_{\mathrm{n}}\boldsymbol{\Lambda}_{\mathrm{n}}^{-\frac{1}{2}} \tag{2.31}$$

28. From Eq. (2.29), we have that $\boldsymbol{N}_{ijk} = \frac{1}{2}(\boldsymbol{D}_{ijk} - \boldsymbol{D}_{(i-1)jk}) + \frac{1}{2}(\boldsymbol{D}_{ijk} - \boldsymbol{D}_{i(j-1)k}) = \boldsymbol{D}_{ijk} - 0.5\boldsymbol{D}_{(i-1)jk} - 0.5\boldsymbol{D}_{i(j-1)k}$. Since the estimation of the noise covariance matrix involves squaring $\boldsymbol{N}$, the result must be divided by $1^2 + 0.5^2 + 0.5^2 = 1.5$ (Boardman and Kruse, 2011).
29. A tridiagonal matrix has nonzero elements on the main diagonal and the first diagonals directly above and below this only.
30. A transformation that reflects a matrix about some plane or hyperplane.
31. A decomposition of the matrix $\boldsymbol{D}$ into a product $\boldsymbol{D} = \boldsymbol{Q}\boldsymbol{L}$, where $\boldsymbol{Q}$ is an orthogonal matrix and $\boldsymbol{L}$ is the lower triangular matrix.

The noise-whitened and mean-corrected data, $\boldsymbol{D}_{\text{mcnw}}$, is thus given by

$$\boldsymbol{D}_{\text{mcnw}} = \boldsymbol{W}^T \boldsymbol{D}_{\text{mc}} \tag{2.32}$$

where $\boldsymbol{D}_{\text{mc}}$ is the mean-corrected image and $\boldsymbol{\Lambda}_{\text{n}}$ and $\boldsymbol{E}_{\text{n}}$ are the eigenvalue and eigenvector components of the noise covariance matrix $\hat{\Sigma}_n$, respectively.

The final step of the MNF transform involves a standard PCA rotation of $\boldsymbol{D}_{\text{mcnw}}$, which projects the data onto its own covariance eigenvectors. This is done using the same procedure as described previously: the covariance matrix $\hat{\Sigma}_{\text{mcnw}}$ of $\boldsymbol{D}_{\text{mcnw}}$ is computed so that the associated eigenvalues and eigenvectors[32] can subsequently be retrieved. The final MNF output is then given by

$$\boldsymbol{D}_{\text{mnf}} = \boldsymbol{E}_{\text{mcnw}}^T \boldsymbol{D}_{\text{mcnw}} \tag{2.33}$$

where $\boldsymbol{E}_{\text{mcnw}}$ is the eigenvector matrix of the covariance matrix $\hat{\Sigma}_{\text{mcnw}}$, estimated from $\boldsymbol{D}_{\text{mcnw}}$.

The MNF transformed image has several useful properties. Firstly, it contains uncorrelated unit variance white noise, which is essential for proceeding with the mixture tuning part of the MTMF algorithm. Additionally, the data has a zero mean and uncorrelated variables, which is useful for speeding up and simplifying the rest of the MTMF process (Boardman and Kruse, 2011).

ii) Matched Filtering

After pre-processing and data conditioning, the MNF image $\boldsymbol{D}_{\text{mnf}}$ can be used as input to the MTMF algorithm. The method consists of two discrete steps; the first part is Matched Filtering (MF). This process can be described as a filtering of image pixels for good matches to the user-supplied target spectrum, while the remaining background spectra are suppressed (Mundt et al., 2007). The target spectrum must match the units of the input image for the algorithm to work and therefore needs to be transformed to MNF space using the method described in i). A *Matched Filter vector* is then created by projecting the transformed spectrum onto the inverse covariance matrix of the MNF data and normalising it to the magnitude of the target spectrum. This way, the MF vector is of unit length and corresponds to target abundance ranging from 0.0 to 1.0 (or 0 to 100%). Its mathematical expression is given as

$$\boldsymbol{w} = \frac{\hat{\Sigma}_{D_{\text{mnf}}}^{-1} \boldsymbol{s}_{\text{mnf}}}{\boldsymbol{s}_{\text{mnf}}^T \hat{\Sigma}_{D_{\text{mnf}}}^{-1} \boldsymbol{s}_{\text{mnf}}} \tag{2.34}$$

32. The eigenvectors will always be orthogonal with non-negative eigenvalues due to the nature of the PCA algorithm

where $\hat{\Sigma}^{-1}_{\boldsymbol{D}_{\text{mnf}}}$ is the estimated covariance matrix[33] of the MNF transformed image and $\boldsymbol{s}_{\text{mnf}}$ is the $b \times 1$ vector of the target spectrum in MNF space. MF scores are computed for each pixel through a projection of the MNF image onto the MF vector $\boldsymbol{w}$ from Equation (2.34). The output image is an $i \times j$ target abundance rule image (Mundt et al., 2007), defined as

$$\boldsymbol{D}_{\text{mf}} = \boldsymbol{D}_{\text{mnf}}\boldsymbol{w} \tag{2.35}$$

Its pixel values represent the magnitude of the output MF scores, where any positive value indicates the fractional abundance of the target component, and 1.0 equals a perfect match. MF scores that are zero or negative represent background pixels in which no target component is detected.

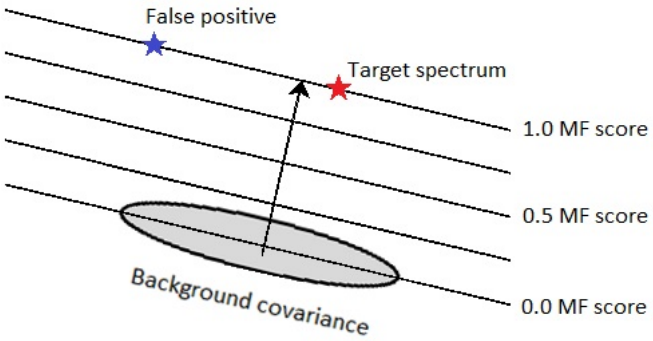

Figure 2.13: Diagram illustrating the classical Matched Filtering method. Modified figure from Boardman and Kruse (2011).

For systems with low spectral contrast[34], MF values greater than one may occur; typically as the result of spectral confusion. This irregularity can be interpreted as an artefact of variability within the target or as unique mixtures of background components that falsely identify as the target spectrum (Mundt et al., 2007). In the classical Matched Filtering approach (as illustrated in Figure 2.13), there are no means of rejecting false positives; MF scores provide purely a measure of calculated (and thus assumed) target abundance.

iii) Mixture Tuning

The final step of the MTMF algorithm, and the segregating power from classical Matched Filtering, is *Mixture Tuning* (MT). This step allows for an assessment

33. The covariance matrix of the MNF data will be approximately the same as the background covariance if the target is sparsely distributed.
34. Spectral contrast refers to the level difference between peaks and valleys in the spectrum.

of feasibility, or likelihood of correct matches, for each MF classified pixel. As a high MF score may be received for anomalies that both do and do not resemble the target spectral signature (see Fig. 2.13), infeasibility values can help detect and reject the false positives.

According to the linear mixture model, a purely homogeneous target pixel cannot exhibit any form of mixing with background spectra. Therefore, all variations must be caused by noise in the data. Background pixels, however, can comprise any mixing combination of endmembers and thus contain variance from both the background as well as variance explained by noise. This leads to the following two infeasibility constraints: 1) abundances of each endmember for a given pixel must all be nonnegative, and 2) all abundances must sum up to one. As implied by these constraints, the spectral scatterplot of mixed pixels will occupy an n-dimensional simplex[35] whose vertices are the $n + 1$ endmembers present in the image (Boardman and Kruse, 2011). Pixels that represent a pure target spectrum will lie directly at the end of the target vector and have zero mixing freedom, acting as one of the vertices of the mixing simplex (as illustrated in Figure 2.14, point **c**). For pixels containing 0% of the target material, maximum mixing freedom between all other endmembers exists – provided they are feasible mixtures. Pixels that fall outside the n-simplex will be rejected as infeasible mixtures between target and background (Fig. 2.14; point **d** and **e**).

The proximity of each pixel to its idealised location on the target vector describes the conceptual measure of infeasibility (Mundt et al., 2007). During the MTMF process, a pixel's expected feasible mixing range is calculated from a range of distributions (characterised by their means and standard deviations) as a function of the pixel's MF abundance score. Each MF value is associated with a distribution, ranging from zero abundance in one end (background distribution[36]) to 100% abundance in the other end (target distribution[37]). These distributions are illustrated by the feasibility contours in Figure 2.12, which will get smaller as the pixel approaches the target spectrum. Evidently, the mixing distribution of a pure target is noise only - and here, the noise whitening properties of the MNF transform is advantageous. Since no mixing freedom is allowed in a pure target, all such pixels must be within a few standard deviations of the target spectrum (Boardman and Kruse, 2011). For intermediate distributions, falling anywhere between the two extrema, a linear interpolation of the background- and noise distributions determine their statistics of the respective intermediate MF abundance values.

35. An n-simplex is an n-dimensional object which is the convex closure of its $n + 1$ vertices.
36. Characterised by the mean background spectrum and its standard deviations.
37. Characterised by the target spectrum and unit standard deviations.

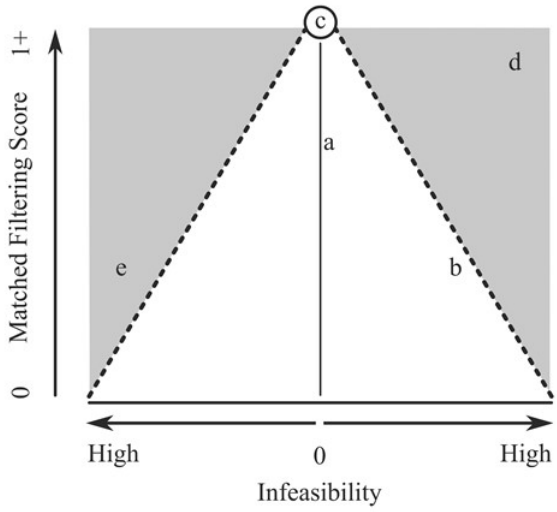

Figure 2.14: Two-dimensional projection (2-simplex) of the MTMF space with Matched Filtering scores and infeasibility scores on the vertical and horizontal axes, respectively. The dashed lines indicate the infeasibility threshold, and the white area represents pixels' mixing freedom. (**a**) Large MF value near zero infeasibility; (**b**) smaller MF value and marginally feasible; (**c**) perfect match between pixel and target spectrum and entirely feasible; (**d**) very large MF score but highly infeasible (false positive); (**e**) low MF score and very infeasible. Figure from Routh et al. (2018).

The Mixture Tuning is performed by calculating infeasibility values (MT scores) for each pixel. This is done using a simple distance measure, where the infeasibility number correspond to the geometric distance from the pixel spectrum to the mean spectrum of the appropriate distribution (associated with the pixel's MF score). Numerically, the MT score refers to the number of standard deviations (of the mixing distribution) between the distribution mean and the pixel. As seen from the noise sigma contours in Figure 2.12, the infeasibility scores vary in DN scale depending on the associated MF value.

In further detail, the calculation of infeasibility for each pixel involves three distinct steps: 1) determination of the pixel's target vector component (mean of the distribution corresponding to the MF score of a pixel), 2) interpolation of the variance eigenvalues derived from the target vector component, and 3) computation of the standardised separation between a pixel and its ideal target vector component via a projection onto scaled eigenvectors (Mundt et al., 2007). For the first step, each pixel's target vector component can be calculated as

$$\boldsymbol{c}_i = d_{\mathrm{mf},i} \times \boldsymbol{s}_{\mathrm{mnf}} \tag{2.36}$$

where $d_{\mathrm{mf},i}$ is the MF score of the ith pixel and $\boldsymbol{s}_{\mathrm{mnf}}$ is the target spectrum in MNF space. Note that Equation (2.36) will only be useful for MNF transformed

data (assuming a zero-mean background), such that the distribution mean ranges from the background spectrum (zero vector) to $\boldsymbol{s}_{\text{mnf}}$ as the MF pixel values range from zero to unity (Boardman and Kruse, 2011).

The second step of the MT calculation involves eigenvalue interpolation for the appropriate distribution. This is done to establish variance thresholds based on a pixel's level of mixing freedom, such that pixels with a small target vector component (i.e., high mixing freedom) are allowed a higher degree of variance and vice versa (Mundt et al., 2007). The eigenvalue interpolation is given by

$$\boldsymbol{e}_i = \left(\sqrt{\boldsymbol{e}_{\text{mnf}}} - d_{\text{mf},i} \times \left(\sqrt{\boldsymbol{e}_{\text{mnf}}} - \boldsymbol{e}_n\right)\right)^2 \tag{2.37}$$

where $\boldsymbol{e}_i$ denotes the vector of interpolated eigenvalues, $\boldsymbol{e}_{\text{mnf}}$ is the vector of MNF values, and $\boldsymbol{e}_n = \text{diag}(\boldsymbol{\Lambda}_n)$; the vector whose elements are the MNF noise eigenvalues (a vector of ones). The variance thresholds, or infeasibility thresholds, derived from this calculation, make up the facets of the linear mixing simplex (as shown in Figure 2.14).

The final step in the infeasibility assessment is a calculation of the geometric distance from the pixel to the target vector, normalised to the infeasibility threshold magnitude corresponding to the pixel's MF score. Mathematically, this is given as

$$d_{\text{mt},i} = \frac{\|\boldsymbol{s}_i - \boldsymbol{c}_i\|}{\|\boldsymbol{e}_i\|} \tag{2.38}$$

where $d_{\text{mt},i}$ is the infeasibility score for the ith pixel, $\boldsymbol{s}_i$ is the MNF spectrum for pixel i, and $\boldsymbol{c}_i$ and $\boldsymbol{e}_i$ are given by Eqs. (2.36) and (2.37), respectively.

The Mixture Tuning part of MTMF will assign an infeasibility value to all pixels in the scene, and their scores can be directly interpreted as a measure of mixing feasibility (Mundt et al., 2007). Low scores are typically associated with feasible mixtures, while high scores (i.e., many standard deviations of separation from the mixing simplex) indicate infeasible mixtures and can be used to reject false positives (Boardman and Kruse, 2011). However, whether a mixture is feasible also depends on the mixing freedom of which the pixel possesses.

Finally, it should be noted that the performance of the MTMF algorithm largely depends on the quality of the user-supplied endmember and the linear properties of the involved spectral mixing. For the MTMF to yield improved results from classical MF, the target spectrum should have a sufficiently low spectral variability, and must therefore be carefully selected for an accurate subpixel detection assessment.

3

Study Area and Datasets

3.1 Great Pacific Garbage Patch

The Great Pacific Garbage Patch (GPGP) is the largest accumulation of marine plastic in the world. Located between Hawaii and California, it covers an estimated surface area of 1.6 million km^2 in the North Pacific Ocean (The Ocean Cleanup, 2021) – a figure more than four times the size of Norway. The GPGP is formed by the North Pacific Gyre, a large-scale rotating ocean current that draws floating debris into its stable centre and subsequently forms 'patches' of marine litter. The gyre actually comprises two such patches: the Western Garbage Patch, located southeast of Japan, and the Eastern Garbage Patch, more commonly known as the Great Pacific Garbage Patch (Figure 3.1). These regions of swirling debris are linked by the North Pacific Subtropical Convergence zone, where warm water from the South Pacific converges with cooler water from the Arctic. This way, marine debris can be transported over large distances from one patch to another.

Conventional plastics are not biodegradable; they simply break into smaller pieces over time, caused by the effects of the sun, oceanic waves, and marine life (Micalizio, 2019). The amount of marine debris can therefore accumulate to form areas comprising millions of tonnes of plastic. However, because the accumulation zones are so large, the plastics appear as highly dispersed rather than a floating 'island' of debris - contradicting many people's envision of the patch. Much of the debris, particularly in later stages of degradation, is also suspended in the upper layers of the water column, and much of it sinks to the

ocean floor. Debris size varies greatly, ranging from large derelict fishing nets to tiny pieces of microplastic (<5 mm). Combined, these factors make plastic detection by satellite imagery challenging, albeit not impossible.

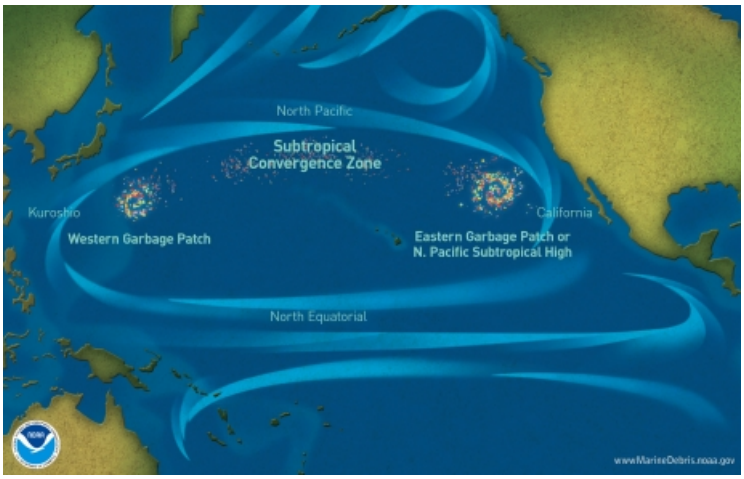

Figure 3.1: The garbage patch is formed in the gyre of the North Pacific Subtropical Convergence Zone. Image credit: NOAA.

The extent of the study area is illustrated in Figure 3.2 and was based on research conducted by The Ocean Cleanup Foundation. By simulating concentration levels of floating debris in the North Pacific, the team of scientists demonstrated significant seasonal and interannual variations of the GPGP's shape and location due to changes in sea surface winds and currents (Lebreton et al., 2018). On the basis of these findings, the study area for this project was selected to include both the conventional extent of the area as well as its seasonal and interannual variability, encompassing the entire patch regardless of the year.

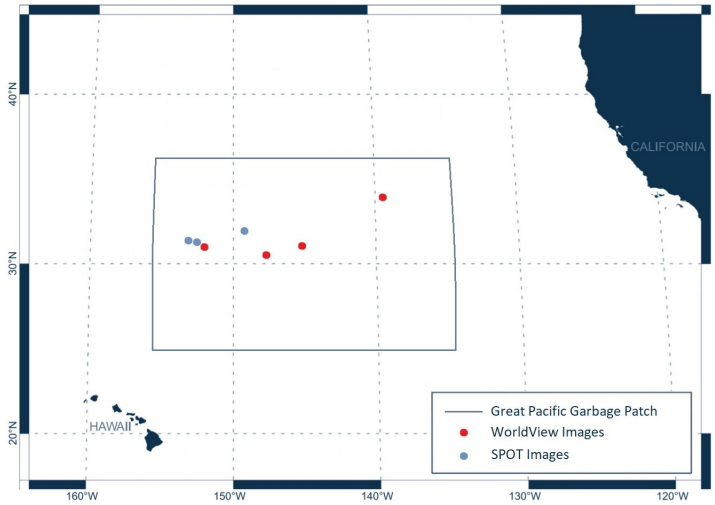

Figure 3.2: Extent of the study area in the North Pacific Ocean with approximate positions of the satellite imagery marked. Note that seasonal and interannual variations of the GPGP extent are included in this figure (i.e., the actual garbage patch is considered smaller). Figure made in QGIS 3.18.2.

3.2 Satellite Data

Initially, 31 images from 9 different commercial satellites were made available by KSAT for this project, consisting of 24 optical and 7 synthetic aperture radar (SAR) products. The optical imagery comprised very high spatial resolution scenes (0.3–6 m) from the following satellites: KOMPSAT-3, KOMPSAT-3A, SPOT-6, SPOT-7, WorldView-2 (WV2), and WorldView-3 (WV3). The SAR products, on the other hand, were from Radarsat-2, SAOCOM-1A, and TerraSAR-X with spatial resolutions ranging from 3 to 100 metres.

Although the purpose of this study was to explore the images for marine plastic litter, low availability of ground truth information for the given datasets was a severely limiting factor. Without *in situ* data for confirmation or a sufficiently high spatial resolution to visually distinguish plastics from other sea surface features, any conclusions drawn from such images would have been purely based on assumptions. For this reason, supported by the limited time frame of the project, the focus was gradually shifted to be on the images with confirmed GPS tracker information alone. These datasets, consisting of three SPOT and five WorldView images, are presented in the following sections, and only results involving this imagery are considered and discussed throughout the thesis.

3.2.1 SPOT-6/7

The SPOT series of missions has been supplying high resolution optical imagery since 1986. SPOT-6 (launched in 2012) and SPOT-7 (launched in 2014) are the two latest and only operational satellites in the series as of May 2021, and they are owned by Airbus Defence and Space - a division of the European multinational aerospace corporation Airbus. SPOT-6 and -7 carry the same multispectral instrument[1] with a panchromatic band, four multispectral bands in VNIR (visible and near-infrared), and a swath width of 60 km (refer to Table 3.1 for details of spectral bands). The two satellites make up a constellation that can provide a revisit frequency of 1 day in cloud-free conditions.

Table 3.1: Wavelengths of the SPOT-6 and SPOT-7 spectral bands. Spatial resolution is at nadir.

	SPOT-6/-7		
Band	**Central Wavelength (nm)**	**Bandwidth (nm)**	**Spatial Resolution (m)**
Panchromatic	598	289	1.5
Blue	485	66	6
Green	560	61	
Red	660	70	
NIR	825	121	

KSAT holds the licence to the SPOT imagery that was collected for the purpose of the study. This includes three SPOT-6 and five SPOT-7 scenes, of which three had associated ground truth information[2]. These three images – two SPOT-6 and one SPOT-7 scene – are presented in Table 3.2.

Table 3.2: Details of the SPOT datasets.

Satellite	**Date and Image Time (UTC)**	**Product Type**	**Spatial Resolution**
SPOT-6	20200706, 20:21:53	Pan + 4 band VNIR	1.5/6 m
SPOT-6	20200727, 20:09:58	Pan + 4 band VNIR	1.5/6 m
SPOT-7	20200705, 20:30:27	Pan + 4 band VNIR	1.5/6 m

According to the SPOT Imagery User Guide[3], all SPOT products are corrected for radiometric and sensor distortions as a minimum. Optional further processing can thereafter be applied by request of the customer. For the imagery presented in Table 3.2, the geometric processing level is 'Standard Ortho', which

1. New Astrosat Optical Modular Instrument (NAOMI).
2. GPS tracked plastic conglomerates.
3. SPOT product guide available from: `https://www.intelligence-airbusds.com/en/8718-user-guides`

means that the products are georeferenced and corrected from acquisition and terrain off-nadir effects (Airbus Defence and Space, 2021). The radiometric processing level for the SPOT-7 and the SPOT-6 acquired on 05/07/20 and 06/07/20, respectively, is 'Reflectance', while the SPOT-6 image from 27/07/20 is a 'Basic' product. The latter means that the image pixels consist of digital numbers from the sensor acquisition, i.e., native values after equalisation that are not physically meaningful without calibration. However, all Basic products are corrected for radiometric and sensor distortions (e.g., striping artefacts produced by nonuniformity of detectors), referred to as *relative radiometric correction*. 'Reflectance' processing, on the other hand, means that the pixels have been calibrated to at-sensor reflectance and represent actual physical values (*absolute radiometric correction*). For SPOT Reflectance products, the pixel values are scaled by a factor of 10,000.

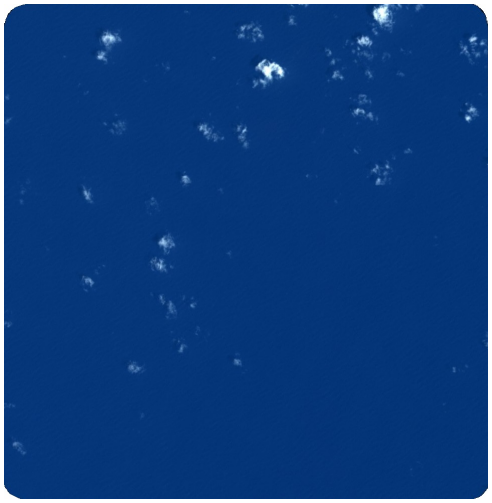

Figure 3.3: A SPOT-6 scene preview. The image, acquired on 27/07/20, is a Level 1L product displayed in RGB colour. *©Airbus DS/Spot Image 2020.*

3.2.2 WorldView-2/3

The WorldView series consists of commercial Earth observation satellites owned by Maxar Technologies (previously known as DigitalGlobe Inc.) – a space technology company based in the United States. The first three satellites in the series are currently operational and supply high resolution imagery from a sun-synchronous orbit. WorldView-1, launched in 2007, carries a panchromatic-only instrument which produces 50 cm resolution grayscale imagery, while WorldView-2 (launched in 2009) and WorldView-3 (launched in 2014) carries a camera with 8 spectral bands in VNIR. Additionally, WorldView-3 has 8

bands in the SWIR spectral range and 12 CAVIS[4] bands. Specifications for the WorldView-2 and WorldView-3 satellites are given in Table 3.3 and Table 3.4, respectively.

The WorldView imagery available for this study was kindly provided by the National Oceanic and Atmospheric Administration (NOAA) and shared with their permission by KSAT. There are five images in total, of which three are 8-band VNIR images from WorldView-2 and two are 8-band images from WorldView-3 - one in VNIR and one in SWIR. Panchromatic bands are available for all four VNIR images. The WorldView-3 scenes are overlapping and acquired two seconds apart, while the WorldView-2 images are located in different parts of the North Pacific and acquired on different dates. Table 3.5 lists further details of the imagery, and Figure 3.4 displays the entire WorldView-2 image (~270 km^2) from 19/05/20.

Table 3.3: Wavelengths of the WorldView-2 spectral bands. Spatial resolution is at nadir.

WorldView-2			
Band	**Central Wavelength (nm)**	**Bandwidth (nm)**	**Spatial Resolution (m)**
Panchromatic	632	337	0.46
Coastal Blue	427	52	1.8
Blue	478	61	
Green	546	70	
Yellow	608	39	
Red	659	60	
Red Edge	724	40	
NIR 1	833	118	
NIR 2	908	92	

All five images are product Level 1B, or 'Basic Imagery Products', which means that minimal processing has been applied to the imagery. According to the DigitalGlobe Core Imagery Products Guide[5], Basic Products are designed for users with advanced image processing capabilities. Applied processing includes radiometric- and sensor corrections but not geometric projection to a plane using a map projection or datum. The correction for sensor distortions blends the pixels from all detectors into the synthetic array to make a single image, and because the look angle of the satellite gradually changes during the image acquisition process, the resulting GSD will vary across the entire scene. A

4. CAVIS (Clouds, Aerosols, Vapours, Ice, & Snow) bands are intended for atmospheric monitoring and correction.
5. DigitalGlobe product guide available at: `http://lps16.esa.int/posterfiles/paper1213/[RD12]_digitalglobe-core-imagery-products-guide.pdf`

Table 3.4: Wavelengths of the WorldView-3 spectral bands (excluding CAVIS bands). Spatial resolution is at nadir.

WorldView-3			
Band	**Central Wavelength (nm)**	**Bandwidth (nm)**	**Spatial Resolution (m)**
Panchromatic	625	350	0.31
Coastal Blue	425	50	1.24
Blue	480	60	
Green	545	70	
Yellow	605	40	
Red	660	60	
Red Edge	725	40	
NIR 1	833	125	
NIR 2	950	180	
SWIR 1	1210	30	3.7
SWIR 2	1570	40	
SWIR 3	1660	40	
SWIR 4	1730	40	
SWIR 5	2165	40	
SWIR 6	2205	40	
SWIR 7	2260	50	
SWIR 8	2330	70	

Table 3.5: Details of the WorldView datasets.

Satellite	**Date and Image Time (UTC)**	**Product Type**	**Spatial Resolution**
WorldView-2	20200518, 20:41:26	Pan + 8 band VNIR	0.7/2.7 m
WorldView-2	20200519, 20:01:54	Pan + 8 band VNIR	0.5/1.9 m
WorldView-2	20200611, 20:57:09	Pan + 8 band VNIR	1.1/4.2 m
WorldView-3	20200701, 20:56:59	Pan + 8 band VNIR	0.3/1.3 m
WorldView-3	20200701, 20:57:01	8 band SWIR	3.8 m

geometric calibration file containing Rational Polynomial Coefficients (RPCs) is supplied with the product to allow for orthorectification of the data, i.e., removing distortions that occur during imaging, for the purpose of creating a planimetrically correct image (Harris Geospatial Solutions, 2020).

In addition to the five images listed in Table 3.5, an atmospherically corrected subset of the 20200519 WorldView-2 scene was supplemented by NOAA. The image is an Ortho-Ready Standard (Level OR2A) product processed with ACOMP atmospheric correction.

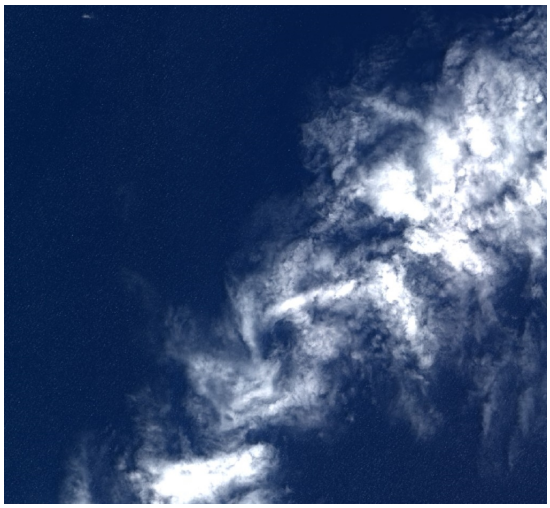

Figure 3.4: RGB composite of a full WorldView-2 scene (Level 1B/Basic product), acquired on 19/05/20. *WorldView-2 ©2020 DigitalGlobe, Inc., a Maxar company.*

3.3 GPS Satellite Trackers

The only ground truth data related to the satellite imagery were GPS trackers attached to conglomerates of floating plastic debris (illustrated in Figure 3.5). The North Pacific Ocean comprises many such trackers, operated by Ocean Voyages Institute, of which four were overlapping with the image data. Although providing valuable ground truth information, it should be noted that the markers have a chance of becoming detached from the plastic and thus being much less useful. At times they can also submerge while still producing a signal that can be recorded. However, since the imagery associated with the GPS trackers is of very high spatial resolution, a visual inspection can in many cases confirm an anomaly in proximity of the tracker. Table 3.6 presents the recorded signal information associated with the available satellite imagery[6].

Tracker A had a positive tracker detection in the WorldView-2 image acquired on 20200518. The recorded signals closest to image acquisition time were at 19:29 UTC (1 hour and 12 minutes before image caption) and at 00:00 (3 hours and 19 minutes after image caption).

Tracker B was confirmed in the WorldView-2 image from 20200519. The signal was recorded at 20:00, 1 minute and 54 seconds before image acquisition, and is the closest to image caption time out of all tracker detections.

6. In the original version of this document, explicit location information and native satellite tracker IDs were listed in the table. For confidentiality purposes, location information has been removed and GPS tracker names have been changed.

Figure 3.5: Floating ghost net in the Great Pacific Garbage Patch with a GPS tracker attached. Image credit: Ocean Voyages Institute.

Table 3.6: Confirmed positions and corresponding times of four GPS-tracked plastic conglomerates in the North Pacific Ocean (note that locations have been redacted owing to confidentiality).

Tracker ID	Date	Time (UTC)	Latitude (N)	Longitude (W)
Tracker A	18/05/20	18:00	–	–
	18/05/20	19:29	–	–
	19/05/20	00:00	–	–
Tracker B	19/05/20	20:00	–	–
Tracker C	11/06/20	12:00	–	–
	12/06/20	00:00	–	–
	27/07/20	20:00	–	–
Tracker D	01/07/20	12:00	–	–
	02/07/20	00:00	–	–
	05/07/20	00:00	–	–
	05/07/20	04:00	–	–
	05/07/20	08:00	–	–
	05/07/20	12:00	–	–
	05/07/20	16:00	–	–
	05/07/20	20:00	–	–
	06/07/20	00:00	–	–
	06/07/20	04:00	–	–
	06/07/20	08:00	–	–
	06/07/20	12:00	–	–
	06/07/20	16:00	–	–
	06/07/20	20:00	–	–

Tracker C was confirmed at 20:00 in the SPOT-6 scene from 20200727. The signal was recorded 9 minutes and 58 seconds before image acquisition. Furthermore, Tracker C was also confirmed in the WorldView-2 image from 20200611 at 12:00 (8 hours and 57 minutes before image) and at 00:00 (3 hours and 3 minutes after image).

Tracker D had a total of 14 signal recordings related to the satellite imagery. The first two detections were confirmed in the WorldView-3 images from 20200701 at 12:00 (8 hours and 57 minutes before image) and at 00:00 (3 hours and 3 minutes after image). The remaining detections corresponded to two SPOT images – one SPOT-7 scene from 20200705, in which the closest marker position was recorded 30 minutes and 27 seconds before image caption, and one SPOT-6 scene from 20200706 with a positive tracker confirmation 21 minutes and 53 seconds before the image.

3.4 Supplementary Data

In addition to the satellite imagery and GPS tracker information, supplementary datasets were available from the University of Hawaii. This includes cloud coverage, wind speed and direction, and projected accumulation data. All datasets are freely available and can be accessed online[7] from the Asia-Pacific Data-Research Center (APDRC). Additionally, global surface current data from the OSCAR (Ocean Surface Current Analyses Real-time) product can be accessed via NASA[8] with a 5-day resolution. For daily current velocity estimates, Copernicus Marine Service offers global ocean physics analysis data from CMEMS (`http://marine.copernicus.eu/`).

7. Available at: `http://apdrc.soest.hawaii.edu/data/data.php`
8. Available at: `http://podaac-tools.jpl.nasa.gov/soto/`

4

Method

Given the exploratory nature of this study, the aim was to evaluate the potential of different methods for marine plastic detection. A literature review of published research articles was done at the start of the project period to map the field's current advancements and challenges. Following this, a number of approaches were systematically explored using the provided satellite imagery. A spectral analysis was emphasised, and priority was given to the images with GPS tracker information in proximity to image acquisition time.

All processing and image analysis have been conducted in ENVI (ENvironment for Visualising Images) and ENVI Classic 5.6 – software programs developed by L3Harris Geospatial for analysing remote sensing imagery. An ENVI licence was kindly provided by the Geological Remote Sensing Group (GRSG), who offers one-year software licences to student members. The ENVI Atmospheric Correction Module, requiring a separate licence, was generously provided free of charge by Harris Geospatial Solutions for a 60-day period. Moreover, open source software such as QGIS (v. 3.16.0) and Google Earth Pro have been used for image visualisation and for creating vector layers of the GPS tracker positions. Finally, Spyder (written in the Python language) has been used for implementing some of the algorithms and for plotting graphs.

4.1 Image Pre-processing

Image pre-processing is the first step in any image analysis workflow, where the methods depend on the specific application and on the initial product level of the satellite data. To conduct an unbiased spectral analysis, the integrity of the spectral response must be retained. Pre-processing steps should therefore conserve as much spectral information as possible while also enabling intercomparison between separate datasets.

The Level 1B WorldView imagery (presented in Table 3.5) was processed according to Figure 4.1, however; products from each step were individually conserved throughout the pre-processing workflow. This way, different levels of processed imagery were easily accessible for applications benefiting from fewer pre-processing steps than what was provided in the end-product.

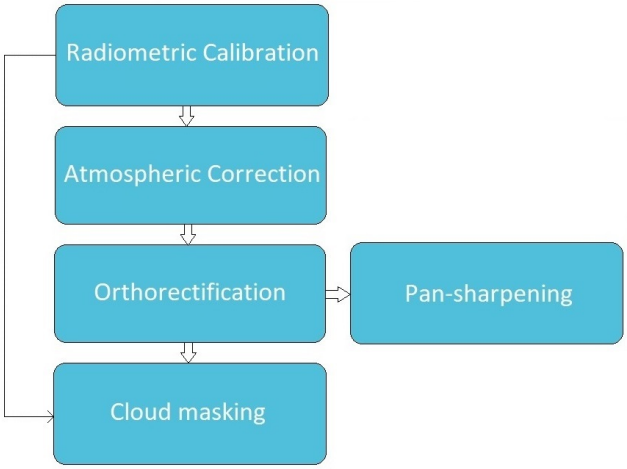

Figure 4.1: Image pre-processing workflow for WorldView Level 1B imagery.

4.1.1 Atmospheric Correction

At present, no generic, automated, and well-grounded atmospheric correction (AC) algorithm exists for water applications of metre-scale resolution imagery (Vanhellemont and Ruddick, 2018). The correction of broadband optical sensors without SWIR bands is particularly challenging, as these wavelengths are commonly used to improve the performance of AC schemes over large water bodies[1]. Another challenge is the unavailability of reliable information in the remote parts of the world oceans, where many correction algorithms utilise atmospheric parameters derived from spaceborne instruments that do

1. Water is a strong absorber of SWIR wavelengths, which are thus useful in correction schemes over the ocean.

not provide coverage in the GPGP area[2]. Furthermore, there is a chance of 'over-correcting' the data: the radiance pixel values of deep water scenes are generally very low, which can cause AC models to subtract too much of the signal (hence, 'over-correcting' the image), resulting in zero to negative reflectance values.

However, the benefits of using atmospherically corrected imagery may outweigh its limitations. Essentially, units of at-surface reflectance is ideal not only to have a common measure between images but also to highlight spectral features in the wavebands. Many spectral indices, detection algorithms, and classification schemes require pixel values of surface reflectance to work properly, and for methods to be adopted across imagery of different sensors, a common radiometric scale is necessary for consistency in processing and for allowing intercomparison.

There are two main steps for atmospheric correction: 1) transformation of digital number (DN) values to at-sensor spectral radiance (the scaling is important as different correction algorithms require different scale factors to produce proper results) and 2) transformation of at-sensor radiance to surface reflectance (atmospheric correction step; Jawak et al., 2019). All of the images in this study have been corrected for radiometric and sensor distortions[3] by the provider; however, to represent physically meaningful values of radiance or reflectance, and to be used for input in AC algorithms, the images must be converted to absolute radiometry.

Using Eq. (2.9) from Section 2.3.1, the SPOT Basic product and WorldView images were calibrated to TOA radiance. TOA reflectance images were also computed using the following equation:

$$\rho_\lambda = \frac{\pi \cdot L_\lambda \cdot d^2}{Esun_\lambda \cdot cos(\theta_s)} \tag{4.1}$$

where L_λ is the at-sensor radiance calculated from Eq. (2.9), d is the Earth-sun distance in astronomical units for the image acquisition date, $Esun_\lambda$ is the band-averaged exoatmospheric solar irradiance, and θ_s is the solar zenith angle (Kuester, 2017). All necessary values for calculation of Eq. (4.1) and its parameters are found within the image metadata. Two of the SPOT images (20200705 and 20200706), already in units of TOA reflectance, were not further pre-processed. The radiometric calibration was successful for all scenes except

2. For example, the Moderate Resolution Imaging Spectroradiometer (MODIS) instrument.
3. Radiometric corrections include relative radiometric response between detectors, non-responsive detector fill, and conversion parameters for absolute radiometry (Maxar Technologies, 2020).

the WV3 20200701 SWIR image, which, for unknown reasons[4], obtained a zero pixel value for nearly all oceanic pixels.

The next step was then to test the effects of different atmospheric corrections in the Pacific Ocean. Three methods were explored for this purpose: ACOLITE (scene-based), FLAASH (model-based), and ACOMP (Maxar product). Finally, a qualitative assessment to compare AC techniques was conducted by calculating unbiased percentage differences (UPDs).

ACOMP

The ACOMP algorithm, developed by Maxar Technologies, is a commercial product provided at request by the customer for an additional charge. For this reason, only a small subset of the 20200519 WorldView-2 scene was processed, based on its proximity to a GPS satellite tracker (Tracker B). The spatial extent and ACOMP result is illustrated in Figure 5.3b.

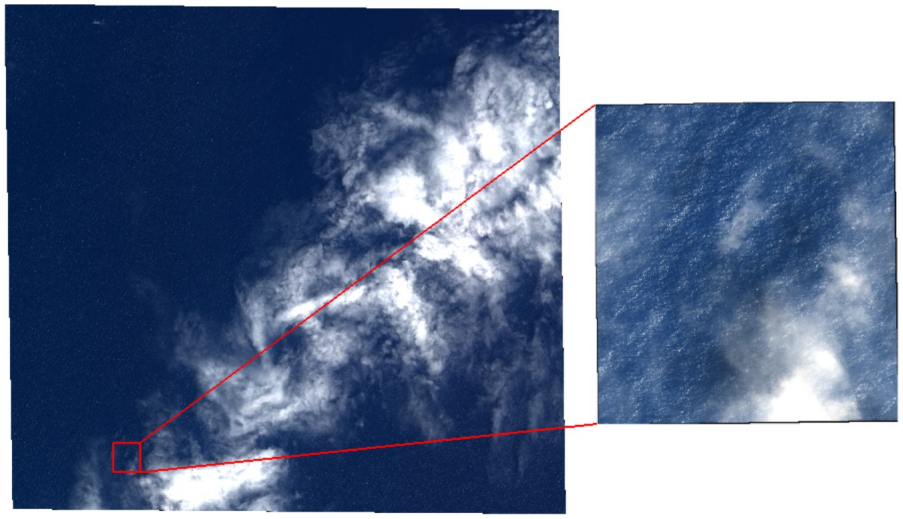

Figure 4.2: WorldView-2 scene acquired on 19/05/20 (left) showing the spatial subset of the ACOMP corrected image (right). *WorldView-2 ©2020 DigitalGlobe, Inc., a Maxar company.*

4. Possibly due to errors within the image metadata or an error in the ENVI software. Regardless, shortwave infrared spectral bands can be difficult to correct due to the low signal response of the ocean.

ACOLITE

The inherent optical properties of plastic debris can be utilised for detection if wavelengths in the NIR region are conserved during the atmospheric correction process (Biermann et al., 2020). This is a trait included in the scene-based ACOLITE Dark Spectrum Fitting (DSF) algorithm: by dynamically selecting the darkest pixels based on multiple dark targets in a given scene, no previously defined 'dark band' like the NIR is required (Vanhellemont and Ruddick, 2018). Although ACOLITE was originally developed for coastal waters in Landsat 8 and Sentinel-2 imagery, its current version supports processing of several other sensors, including SPOT and WorldView. Using the Python script for ACOLITE DSF (version 20210114.0), outputs for apparent surface reflectance (rhos, ρ_s) were computed for the WorldView and SPOT Basic imagery[5] and visualised in ENVI. ACOLITE was the only successful radiometric pre-processing of the SWIR WV3 image.

An issue with the coastal blue band (B1) was discovered during ACOLITE processing of the WorldView data. The channel, which is expected to have a strong signal in oceanic scenes, showed a significantly lower response compared to the other visible channels. Quinten Vanhellemont, a developer of ACOLITE, was contacted and could confirm the presence of the issue and that it had not yet been addressed as of mid April 2021. For this reason, the coastal blue band has been excluded from all further processing of ACOLITE corrected WorldView imagery.

A new generic version of ACOLITE was released on 4 May 2021, offering better performance for WorldView imagery; however, the time left for this project was not sufficient to repeat processing.

FLAASH

The FLAASH algorithm uses the MODTRAN radiative transfer model code and has been extensively tested for its capability to retrieve surface reflectance (Jawak et al., 2019). Its input file must be an at-surface radiance image in units of $\mu W/(cm^2 \cdot sr \cdot nm)$, which was computed using Equation (2.9) with a scale factor of 0.1. The application of the FLAASH model was then performed in ENVI v5.6 as an automated two-step calculation. The first step was the retrieval of atmospheric parameters (Eq. (2.10)) through an aerosol description (including initial visibility or aerosol optical depth) and assumption of a certain model atmosphere. The 'Maritime' aerosol model was selected for all images,

5. For ACOLITE, the input should be the uncalibrated data (relative radiometric correction data) as the algorithm itself will do the necessary conversions for absolute radiometry.

which is most representative for oceanic scenes. As no water vapour information was available, the atmospheric model was selected based on the surface air temperature (which tends to correlate with water vapour), whose values were retrieved from the APDRC[6] for each scene. From this, the 'Mid-Latitude Summer' atmospheric model was found to be suitable for all images. Aerosol retrieval was set to 'None' as neither of the datasets contained appropriate aerosol bands.

In the second and final step, the atmospheric and aerosol/haze models were used for the solution of the radiative transfer equation (Eq. (2.11)) to obtain surface reflectance data. Figure 4.3 illustrates the difference between an at-sensor radiance image and a BOA corrected FLAASH image using WorldView-2 data.

The aerosol optical depth (initial visibility) was initially left at its default value of 40 km; however, this resulted in zero to negative reflectance values in the NIR bands for nearly all water pixels. After consulting with Dr. Adler-Golden (a developer of FLAASH) and testing with several different initial visibility values, the final parameter was set to 250 km – close to the maximum of ~300 km – to avoid over-correction in the NIR bands, which are already dark over water. While such a high value improved the amount of negative pixel values, it did not fully solve the problem. This is not unexpected, however, as AC models are less robust over open ocean due to the water content in the atmosphere. In addition, 'forcing' the model to yield valid remote sensing reflectances through an over-estimation of optical depth introduces other uncertainties to the data (e.g., for spectral signatures and expected response of endmembers), albeit more reliable results than that of negative (and invalid) pixel values.

With these limitations in mind, the WorldView and SPOT imagery was processed according to the method described. For consistency, all images of the same sensor were processed with equal parameters. Finally, since the output from FLAASH is scaled to integers by default with pixels ranging from 0 to 10,000, the image pixel values were divided by 10,000 to obtain floating-point values (0 to 1.0) of apparent surface reflectance.

Unbiased Percentage Differences

As no reference spectra dataset of marine plastic debris exists, the atmospherically corrected end-products were compared by deriving the unbiased percentage differences at different wavebands, as done previously (Garaba and Zielinski, 2013; Topouzelis et al., 2019). To determine the UPD between two

6. http://apdrc.soest.hawaii.edu/data/data.php

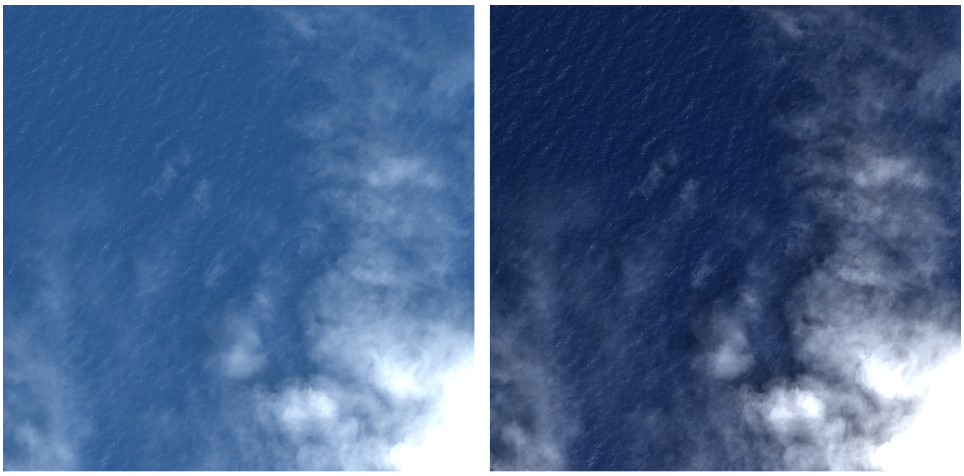

Figure 4.3: Comparison of at-sensor radiance (a) and FLAASH atmospheric correction (b) of a cropped WorldView-2 scene. *WorldView-2 ©2020 DigitalGlobe, Inc., a Maxar company.*

approaches A and B, the following equation was employed:

$$\psi_B^A(\lambda) = \frac{\left|R^A(\lambda) - R^B(\lambda)\right|}{0.5\left(R^A(\lambda) + R^B(\lambda)\right)} \times 100\% \tag{4.2}$$

where R is the normalised reflectance of a given material class at wavelength λ. Equation (4.2) was applied to compare the AC methodologies pairwise using spectra of a known plastic target. Subsequently, the spectral average UPD was calculated summing and weighting Eq. (4.2) for N spectral channels; i.e. (Garaba and Zielinski, 2013),

$$\Psi_B^A(\lambda) = \frac{1}{N}\sum_{i=1}^{N}\psi_B^A(\lambda_i). \tag{4.3}$$

4.1.2 RPC Orthorectification

To leverage the WorldView Level 1B imagery for GIS (geographic information system) applications (e.g., accurate distance measures), reduce geometric distortions, and provide a common map scale between datasets, the imagery must be projected onto a plane through an orthorectification process. Although it is recommended to use a rigorous orthorectification solution to achieve more accurate results for DigitalGlobe (Maxar) Basic data (Harris Geospatial Solutions, 2020), the Rigorous Orthorectification tool in ENVI requires a separate licence that was not available for this study. Instead, ENVI's RPC Orthorectification tool was used, which works well for oceanic scenes where geometric accuracy

will be limited regardless. The inputs to the workflow were the RPC sensor model provided with the image metadata and the Global Multi-resolution Terrain Elevation Data 2010 (GMTED2010) – a digital elevation model (DEM) provided within the ENVI software and used for geoid height correction of the data. No ground control points (GCPs) were applied (this is rarely used for ocean satellite imagery), and the image resampling technique was set to Cubic Convolution[7] as previous research (Rizeei and Pradhan, 2019) indicates better radiometric performance and lower vertical and horizontal uncertainties for this resampling technique as compared to ENVI's other resampling options (Nearest Neighbour and Bilinear Interpolation).

By definition, the orthorectification process modifies the shape of the original image, and resulting pixels may be rearranged or reoriented. Therefore, orthorectification should be performed as one of the last steps of an image pre-processing workflow (i.e., after radiometric calibration and atmospheric correction). However, due to the exploratory nature of this study[8], not only the surface reflectance WorldView data were processed, but also the TOA reflectance and TOA radiance data. The Level 1B imagery and ACOMP subset image (OR2A) were both orthorectified to their respective UTM (Universal Transverse Mercator) zones in the WGS-84 datum.

4.1.3 Pan-sharpening

Pan-sharpening is a technique for combining the spectral information of a multiband sensor with the spatial information of a panchromatic band. While useful for a spatial analysis and improved visual observations, the process introduces uncertainties in the data that can corrupt detection and classification schemes relying on accurate spectral information. For this reason, pan-sharpened imagery should only be used for visual analyses.

In this study, all images associated with a GPS tracker were pan-sharpened using ENVI's SPEAR pan-sharpening tool. The Gram-Schmidt method was chosen for processing, as it uses the spectral response function of a given sensor to estimate what the panchromatic data looks like and is therefore generally more accurate than other pan-sharpening algorithms implemented into ENVI (Harris Geospatial Solutions, 2020). The processing was applied to both atmospherically corrected and at-sensor radiance data.

7. CC uses a weighted average of 16 pixels to approximate the sinc function using cubic polynomials to resample the image. It is generally considered more accurate than simpler resampling methods but more computationally intensive.
8. The uncertainties related to the AC imagery might cause a favouring of radiance data in later applications, in which case nonreflectance orthorectified data would be needed.

In many cases, it is preferable to perform the pan-sharpening process before geometric correction to mitigate small alignment errors caused by the accuracy of the DEMs used in the orthorectification process (Cheng and Chuck, 2010). However, this should only be performed on products where the panchromatic and multispectral data are resampled to occupy the exact same geographic extents, which applies to the ortho-ready SPOT products and ACOMP corrected WorldView-2 subset (Level OR2A), but not to the WorldView Level 1B (Basic) imagery. Therefore, the WorldView Basic products were orthorectified prior to the pan-sharpening process.

Pan-sharpened imagery will have the same spatial resolution as the sensor's panchromatic band. Because of its enhanced resolution, it is useful in detecting waves and sun glint (Vanhellemont and Ruddick, 2018), as well as other floating features on the water surface. As seen in Figure 4.4, the waves are more evident and well-defined in the pan-sharpened image than that of the lower resolution image. However, since any pan-sharpening process will alter the pixels' native spectral information, the resulting pan-sharpened imagery was only used for visually confirming features of interest, in addition to selecting training areas and validating results of classification (i.e., no spectral analyses were conducted using pan-sharpened images).

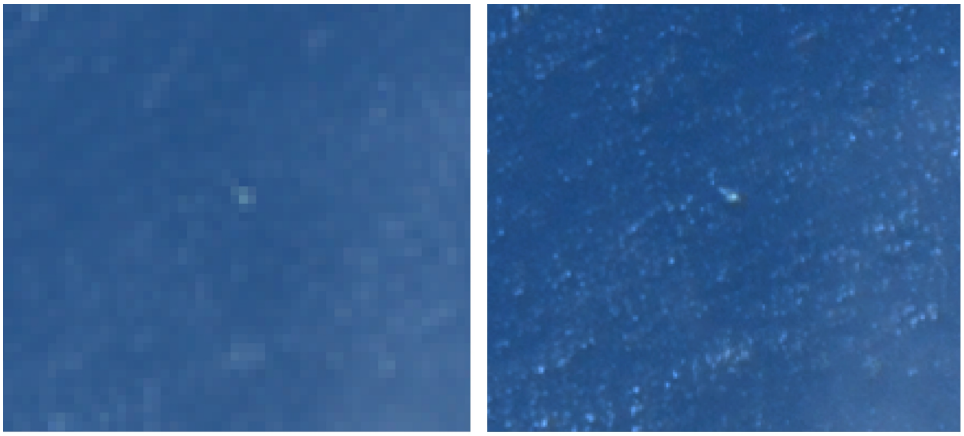

Figure 4.4: Before (**a**) and after (**b**) pan-sharpening of the 20200519 WorldView-2 scene with 1.9 m and 0.5 m spatial resolution, respectively. The images have been calibrated to at-sensor radiance and are zoomed in on Tracker B attached to a plastic conglomerate (seen as a bright spot in the middle of the image). *WorldView-2 ©2020 DigitalGlobe, Inc., a Maxar company.*

4.1.4 Cloud Masking

Optical remote sensing is largely affected by the presence of water vapour in the atmosphere. Clouds do not only limit the amount of surface information that can be extracted from a scene but can also compromise classification algorithms by altering the spectral signature of ground cover subjected to haze or cloud shadows (Lisens et al., 2000). Additionally, cloud removal tends to remove spectral outliers from the image, improving the results of a spectral analysis. Accurate cloud masking is therefore an essential step before any information derivation schemes, albeit difficult as it can result in loss of valid data (e.g., if the cloud is partially transparent; Hu, 2009).

Several cloud detection algorithms have been developed for different types of sensors and with varying levels of complexity and accuracy. For this project, the initial objective was to find such suitable algorithms for the relevant sensors[9]. However, during testing of unsupervised classification in ENVI, it was discovered that this method did an adequate job at distinguishing clouds, haze, and cloud shadows from the oceanic background. The method was therefore adopted to mask out clouds from the satellite imagery using the workflow shown in Figure 4.5. The illustration uses a WorldView-2 scene as an example, but the processing steps were the same for all images.

First, the radiometrically corrected radiance image was processed with ISODATA unsupervised classification in ENVI. Although it was experimented with both a higher and lower number of requested classes, the best results, while still maintaining an acceptable computation time, were produced from using 15 classes. The classes exclusively containing cloud or haze pixels were then manually identified and used to create a temporary mask. To further improve the accuracy of the cloud mask and facilitate enhanced haze removal, a second unsupervised classification processing was applied to the image excluding the masked pixels from the previous classification. Again using 15 classes and manually selecting those of clouds, a final cloud mask for the entire scene was constructed. Visual inspection from zooming in on hazy areas in the image confirmed an acceptable accuracy of the mask and that no further iterations of the process were needed.

9. SPOT-6/7, WorldView-2/3.

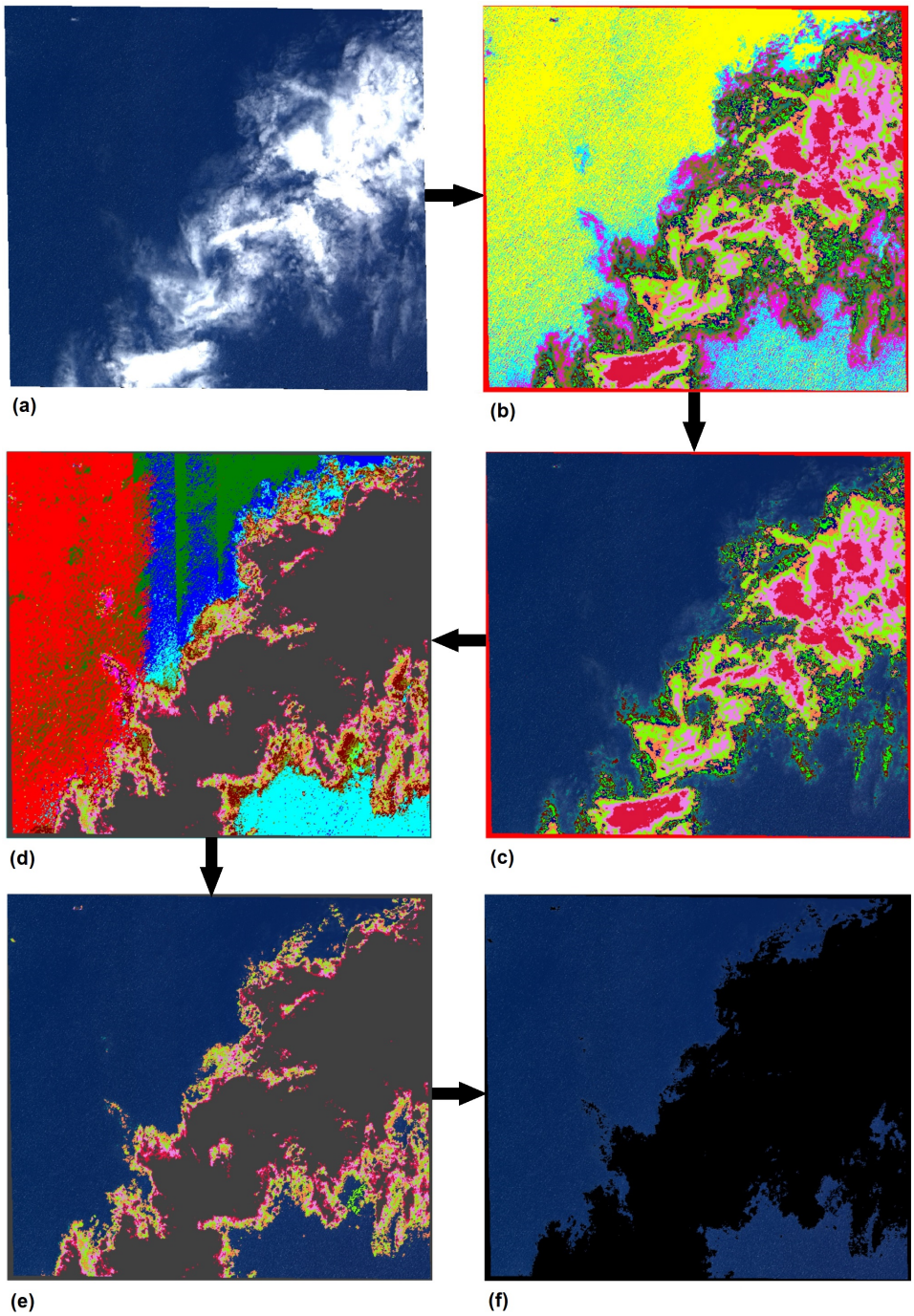

Figure 4.5: Cloud masking process of a WorldView-2 scene using an unsupervised classification approach. (**a**) Stretched radiance image; (**b**) Result of first classification with 15 classes; (**c**) Manually selected classes that contain clouds or haze, excluding water pixels; (**d**) Result of second classification with 15 classes and masked pixels from last step; (**e**) Manually selected classes with remaining cloud pixels; (**f**) Final cloud mask. *WorldView-2 ©2020 DigitalGlobe, Inc., a Maxar company.*

4.2 Calculating Debris Speed and Trajectory

A recurring problem with the ground truth data was the delay between GPS signal recording and satellite image acquisition. This delay ranged from a few minutes and up to several hours, preventing the plastic conglomerates from being accurately pinpointed in the imagery. Marine debris is, like the ocean itself, dynamic; and detection of the known debris becomes increasingly difficult with a larger time gap between GPS signal and image capture. To approximate the GPS tracker's position in a scene, two different approaches were attempted: linear interpolation and plastic velocity estimation. Both methods require a tracker of >1 signal recordings, but results can be adopted to trackers of a single known position[10].

Table 3.6 shows that three out of four GPS markers[11] could be used to estimate the average travel speed of plastic debris at the sea surface. For each of these trackers, daily average speeds were calculated using the recorded coordinates and time intervals between recordings. Direction of travel was determined from the mean angle between GPS signal points of the given day. In addition to these observations, data regarding the wind direction and speed were derived from the Asia-Pacific Data Research Center[12] (APDRC) and the Physical Oceanography Distributed Active Archive Center[13] (PO.DAAC) provided by the University of Hawaii and NASA, respectively. Sea surface current velocity was estimated using daily ocean physics analysis data from CMEMS[14] (Global ocean 1/12° physics analysis and forecast daily product), supported by 5-day resolution data from the OSCAR product. To investigate potential correlations between surface currents, wind speeds, and plastic debris velocity, a simple regression analysis was conducted on the derived values using Microsoft Excel.

4.3 Linear Interpolation and Anomaly Detection

To estimate the plastic position through linear interpolation, a Python script was written using Equation (2.7) and Equation (2.8) from Section 2.2. The 20200706 SPOT-6 scene required linear *extrapolation*, given that the image was captured after the last known recording of Tracker D's position. Linear extrapolation is given as

$$y(x_*) = y_{k-1} + \frac{x_* - x_{k-1}}{x_k - x_{k-1}}(y_k - y_{k-1}) \tag{4.4}$$

10. Here: Tracker B
11. Tracker A, Tracker C, and Tracker D.
12. `http://apdrc.soest.hawaii.edu/data/data.php`
13. `https://podaac.jpl.nasa.gov/dataaccess`
14. `http://marine.copernicus.eu/`

where x_* is the point to be extrapolated and (x_{k-1}, y_{k-1}) and (x_k, y_k) are its two nearest data points. (If $x_{k-1} < x_* < x_k$, Eq. (4.4) becomes equivalent to linear interpolation).

The estimated tracker positions were then compared to the plastic's trajectory derived from estimated debris velocity, surface currents data, and wind speeds and direction. Finally, a polygon was constructed based on the estimations, enclosing an area of high likelihood of plastic debris. In the sequel, an automated anomaly detection using the RXD algorithm was applied to extract any spectral features differing from the background (potential plastics). To ensure that the calculated mean spectrum comprised only negligible contributions from non-background pixels (anomalies), a larger subset containing roughly 6000 pixels was used for the RXD algorithm. Anomaly percentage thresholds were selected interactively by previewing and inspecting detection results, and were finally set to 0.05%. Lastly, the constructed polygons were employed to extract feasible anomalous pixels, whose spectral signatures were inspected for validation.

4.4 Data Analysis

In this study, most methods of data analysis have been conducted utilising the spectral information in the imagery. For remote sensing applications, this refers to the extraction of qualitative and quantitative information from a given pixel's spectral response, derived from its wavelength-dependent reflectance properties (Biermann et al., 2020). Classes of materials can therefore be grouped by their spectral features and characteristics (spectral signatures) and in that way be distinguished from other objects. In a study of this nature, where the ground truth data is very limited, the spectral information is key to provide a level of validation to certain areas or pixels of suspected plastic debris.

4.4.1 Ground Truth Data

Of the four GPS trackers available for this study (presented in Table 3.6), Tracker B was investigated as a potential source for pinpointing plastics due to its proximity to image acquisition time. The tracker, whose signal was recorded approximately two minutes before capture of the 20200519 WorldView-2 image, was located ~9 metres north of a feature clearly distinct from the background (Figure 4.6a). This was explored as a possible patch of plastic debris. To strengthen suspicions, ocean current velocity data was gathered from the Copernicus Marine Service, revealing surface currents in a southward direction for the given time and location (Figure 4.6b). Furthermore, spectral signatures

of the brightest potential plastic pixel were extracted from the atmospherically corrected images (ACOLITE, ACOMP, and FLAASH) and compared to known plastic signatures from published literature (Biermann et al., 2020; Topouzelis et al., 2020; Kikaki et al., 2020). All three reflectance spectra revealed a similar spectral shape as that of other research, including the spectral peak at NIR which is typical for plastics.

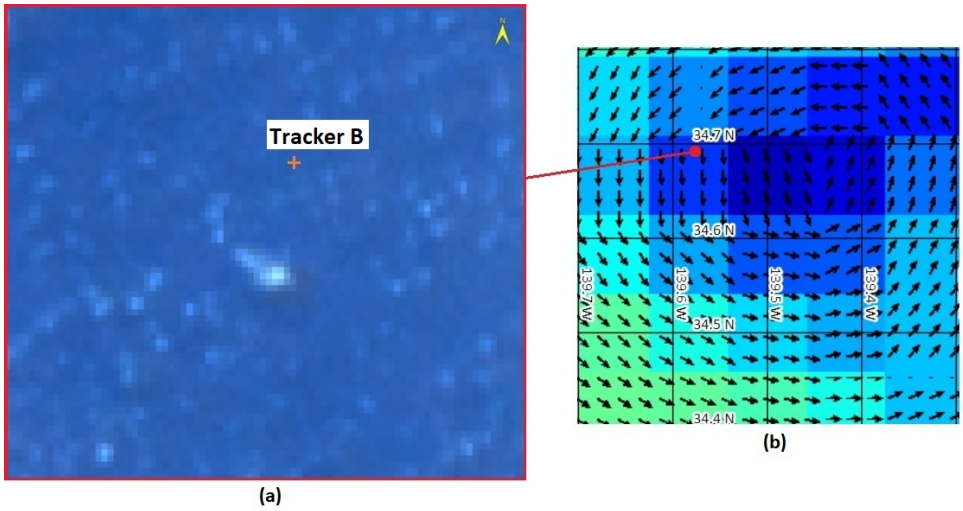

Figure 4.6: (**a**) Pan-sharpened WV2 image showing the recorded position of Tracker B and suspected plastic debris. *WorldView-2 ©2020 DigitalGlobe, Inc., a Maxar company.* (**b**) Sea surface current velocity estimates from 19 May 2020 (gathered from E.U. Copernicus Marine Service Information), where the red dot indicates the position of the subset in (a). Current direction is pointing south with a speed of ~0.07 m/s.

Based on the spectral signatures and currents information, as well as the relative position of the tracker, the suspected plastic conglomerate in the WV2 image was considered validated. Figure 4.7 illustrates the plastics' extent, which provided the basis of the endmember extraction conducted in the following section.

4.4.2 Endmember Extraction

To search for unidentified patches of marine plastic debris across an entire scene, the spectral behaviour of a plastic target must be known. With no known pixels comprising only plastic materials, the challenge was then to obtain a spectral signature representing a pure plastic spectrum. The PPI, while an effective endmember extraction technique for scenes abundant with pure pixels, cannot be used to derive endmembers from mixed pixels. Instead, an inverse spectral unmixing approach was attempted, which requires knowledge of each

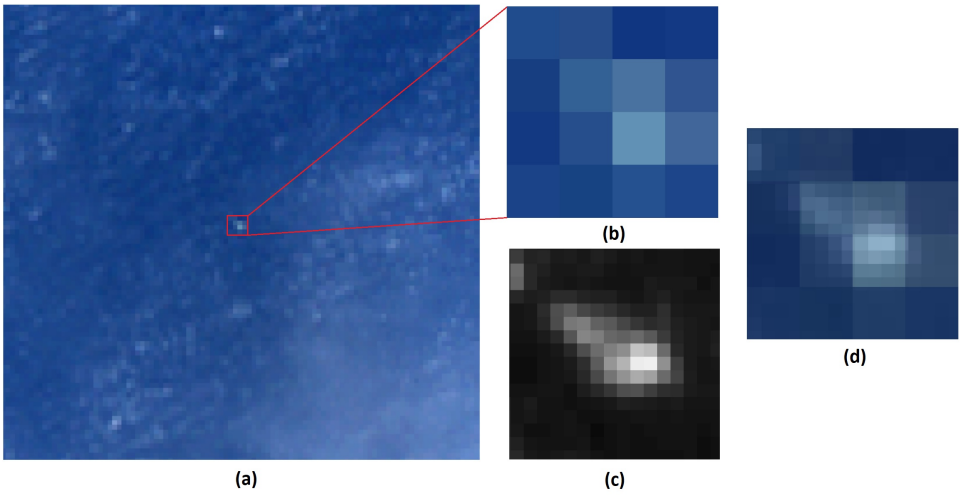

Figure 4.7: Marine plastic debris attached to Tracker B in the 20200519 WorldView-2 image. (**a**) Spatial subset of RGB composite image, approx. 190×190 m; (**b**) Zoomed in on plastic debris (1.9 m pixel cell size); (**c**) Panchromatic band of same subset as (b), with a 0.5 m spatial resolution; (**d**) Orthorectified RGB image with 50% transparency over the orthorectified panchromatic image. *WorldView-2 ©2020 DigitalGlobe, Inc., a Maxar company.*

material's abundance within a given pixel. This approach was inspired by work done in Topouzelis et al. (2019), in which auxiliary data from unmanned aerial systems was used for calculating percentage plastic coverage of Sentinel-2 pixels covering an artificial floating target. The high-resolution drone imagery facilitated the accurate derivation of pixel coverage through object-based image analysis.

In this study, no drone imagery was available; however, the panchromatic band offered significantly higher spatial resolution relative to the multispectral channels. From the confirmed plastic target in the 20200519 WorldView-2 image (Figure 4.7), plastic coverage of each pixel was estimated by utilising the sensor's panchromatic band (0.5 spatial resolution) as a base map with the true colour (RGB) pixels of 1.9 m cell size overlaid as a grid at 60% transparency. For improved geometric accuracy, all bands were orthorectified prior to the segmentation. Then, a quantitative assessment of the plastic target, covered by six lower-resolution pixels (Figure 4.8, A–F), was conducted using a simple thresholding technique. The mean response of panchromatic background pixels was calculated from a random sample of 200 seawater pixels, while a similar calculation was carried out for the plastic target. Next, using the means and standard deviations of background and plastics as a basis for determining thresholds, the panchromatic pixels were either labelled as 'on' or 'off' (i.e., plastic or non-plastic) – not accounting for seawater influence or partial target

submersion.

The resulting estimates of percentage plastic coverage are given in Figure 4.8, where pixel E contains the highest amount of plastics and the least amount of seawater, followed by A, B, D, F, and C (in decreasing order). It should be noted that the spatial resolution of the sensor is not high enough to determine type, density, colour, or absolute extent of the plastic target, and that the calculated abundances are rough estimates only.

To the author's knowledge, such a method for calculating abundance fractions has not been conducted in previously published research. Hence, this work represents first steps towards developing the technique further. For future applications utilising a similar approach, it is advised to take the fraction calculation one step further by introducing a regression analysis or mixture modelling of the panchromatic pixels' magnitude (i.e., estimate fraction of mixture in high-resolution pan-pixels based on pixel intensity relative to the background). This way, a higher accuracy in plastic abundance estimation may be achieved.

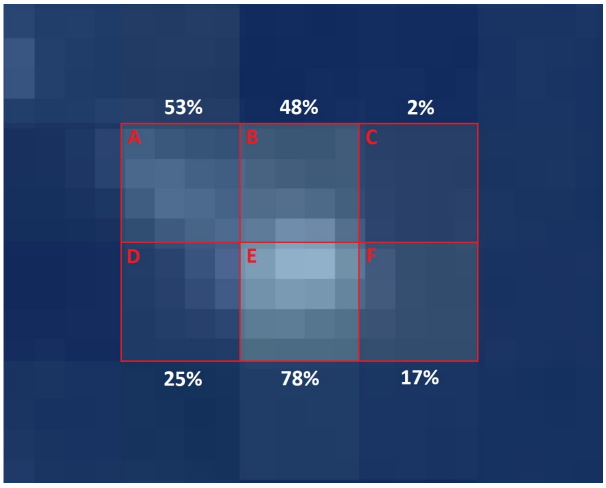

Figure 4.8: Estimated percentage pixel coverage of a GPS tracked plastic target captured by the WorldView-2 imager. The RGB composite is shown with 60% transparency over the panchromatic sensor's band, with 1.9 m and 0.5 m spatial resolution, respectively. Both images have been orthorectified to improve geometric accuracy. *WorldView-2 ©2020 DigitalGlobe, Inc., a Maxar company.*

The ACOMP image, which was delivered as an Ortho-Ready Standard product (OR2A), has a spatial resolution of 2 m instead of 1.9 m. The difference in resolution arises from the standard processing of OR2A products, where the panchromatic and multispectral data are resampled to exactly the same geographic extents (i.e., the GSD is increased for the multispectral bands to

match the extents of the pan band). Hence, abundance calculations had to be repeated for this image. The results yielded an estimated plastic fraction of 65% for the strongest plastic pixel – a lower abundance than for the 1B Basic products, caused by the increased pixel size.

Assuming that the six pixels in Fig. 4.8 only comprise floating plastics and seawater, the inverse spectral unmixing calculation (Section 2.5.3, Eq. (2.28)) takes the form of

$$S_p(\lambda) = \frac{S_{mix}(\lambda) - a_W S_W(\lambda)}{a_p} \tag{4.5}$$

where S_p is the unknown pure plastic spectrum, S_{mix} and S_W are the spectral signatures of the mixed pixel and the water endmember, respectively, and a_W and a_p are the respective fractional abundances of water and plastics. Using the PPI and n-D Visualiser in ENVI, the endmember signature of seawater was derived for both the atmospherically corrected (ACOLITE, ACOMP, and FLAASH) and top-of-atmosphere reflectance scenes. To verify the accuracy of the derived water endmembers, their signatures were compared to the average spectral response of the surrounding waters and also to the library endmember spectrum for open ocean water from the U.S. Geological Survey[15].

Pixel E was used for the unmixing calculation as it had the highest estimated plastic coverage (78%) and was therefore less likely to be influenced by other potential endmembers (e.g., algae, sea foam, or timber) unaccounted for in Eq. (4.5). For the ACOMP image, the brightest pixel corresponding to 65% plastic was used. The mixed pixel's reflectance spectrum was then extracted from both the BOA and TOA images, which allowed the spectral response of the plastic target to be computed for each channel by inserting all known variables into Equation (4.5). Finally, the resulting pure plastic spectra were saved to ASCII files for use in later processing.

Cloud Shadow Influence

A cloud shadow correction of the derived plastic spectra was considered, as visual inspection of the scene confirmed an area of darker seawater surrounding the plastic target (Figure 4.9a). Although cloud shadows in optical imagery generally represent sources of error that should either be removed or corrected for, an assessment of the need for such corrections was conducted individually for this scene. Due to the time of image capture (close to solar noon), it is likely that the shaded region is a *partial* shadowing from the hazy edge of the cloud; that is, direct solar photon interaction is reduced, albeit not

15. Available at: `https://crustal.usgs.gov/speclab/QueryAll07a.php`

blocked[16]. Furthermore, since the water endmembers used in the spectral unmixing calculation are derived from nonshadow pixels, the pure plastic spectra will already be partially corrected for cloud shadow influence through the endmember calculation.

To quantify the impacts of the shadowed area, several regions of water in the ACOMP image were selected to form two classes – one affected and one unaffected by cloud shadowing. The mean spectra of the classes, illustrated in Figure 4.9b, were then used to compute the average brightness difference for each channel. At the maximum, the nonshadowed class exhibited a brightness increase of ~15% (in the coastal blue and blue bands) relative to the darker water. The percentage of increased brightness was reduced for the longer wavelengths, ranging between 2.4% and 5.4% for the yellow, red, and NIR bands. It was not possible to test if the same multiplicative effects would have been seen in plastics, due to the extremely limited training data. However, as shown in Carder et al. (1993), the average reflectance spectrum shift caused by cloud shadows is only about 3.5%, with the shape of the signal mostly preserved.

On account of these arguments, in addition to the uncertainties that were introduced with the abundance estimation (Figure 4.8), cloud shadow influence on the plastic spectral signature was deemed negligible and thus not corrected for. Yet, it should be noted that longer wavelengths (>608 nm) are nearly unaffected by the different scattering conditions (direct vs. indirect; as seen in Fig. 4.9b, indicating that these channels may be preferred for the detection of plastic targets.

4.4.3 SAM Classification

In conventional image classification, knowledge of all endmembers present in a scene is required. However, for the purpose of general target detection, supervised classification can be applied with the use of a single endmember spectrum. This technique, when used on atmospherically corrected[17] reflectance data, is relatively insensitive to illumination and albedo effects – an advantageous attribute for feature detection on a wavy ocean surface.

Using the FLAASH and ACOLITE processed WorldView imagery, the Spectral Angle Mapper (SAM) classification algorithm was applied with the derived

16. A completely shadowed region will only be illuminated by scattered skylight photons, while an unshadowed region is irradiated by both direct solar photons and indirect skylight.
17. SAM can also be used on TOA data, but this was found to produce a high number of misclassifications due to lower spectral separability of endmember spectra.

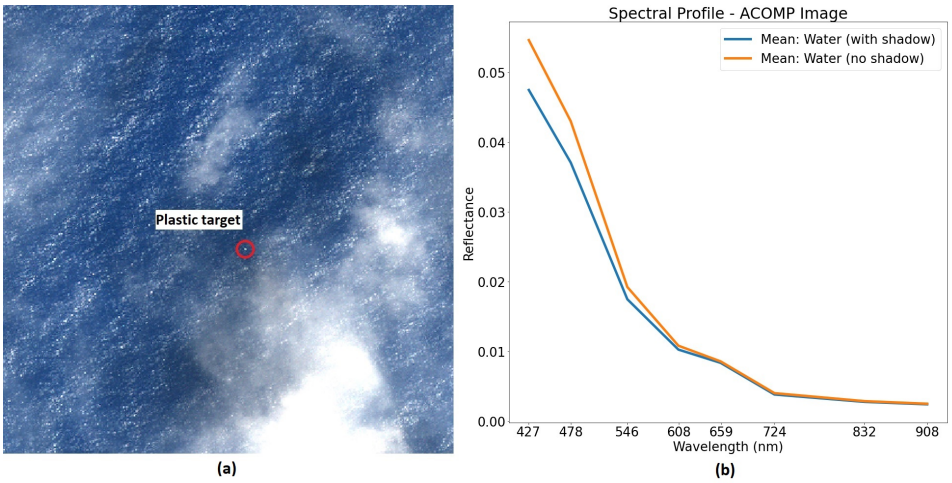

Figure 4.9: The plastic target falls within an area affected by cloud shadow, as seen in (**a**). The spectral plot in (**b**) illustrates the average signal increase for each channel based on the response of selected water pixels for each class – with and without the influence of cloud shadows. *WorldView-2 ©2020 DigitalGlobe, Inc., a Maxar company.*

plastic endmember as reference spectrum. Although the PPI was applied to all individual images in efforts of deriving scene-dependent reference spectra (this would have been beneficial considering differences in image spatial resolution), no spectral signatures believed to be plastics could be extracted. For the SAM classification, at-surface reflectance data was used to ensure that the bands' (hence, feature vectors') origin was at zero in order to minimise errors in angle calculation. A spectral angle threshold was determined through inspection of rule image[18] pixel values of the known plastic target, which showed an angle of 0.08 radians for the pixel of highest plastic abundance (~78%). Based on this, the maximum angle was set to 0.09 radians. For consistency, the FLAASH imagery was chosen for subsequent evaluation of results, as it also offered one extra dimension (band) compared to ACOLITE (due to the faulty processing of the coastal blue band).

4.4.4 Spectral Indices

In methods that involve spectral band manipulations, successful information extraction from images depends on the accuracy of the derivable spectra (Jawak et al., 2019). For this reason, atmospheric effects should generally be removed from the imagery before application of spectral indices. However, uncertainties related to atmospheric correction algorithms, particularly in the North Pacific

18. A grayscale image that shows intermediate classification results for a given class.

Ocean, raised the question of which data would be most appropriate for the plastic detection task.

A training dataset of randomly selected pixels from the seawater and whitecaps class, as well as the two brightest plastic pixels from the 20200519 WV2 image (pixels B and E, Fig. 4.8), was employed to investigate effects of the various pre-processing methods with respect to the primary spectral index to be tested – the Normalised Difference Vegetation Index (NDVI). By creating box and whisker plots of the training samples' respective NDVI values (Fig. 5.9), inherent class variability and material separability could be visualised for each of the different pre-processing techniques: TOA reflectance, ACOLITE, and FLAASH. Based on these plots, the FLAASH image was ruled out for spectral index applications due to insufficient response (zero reflectance) in the NIR bands for a majority of the seawater training pixels. The plastic class was observed to be marginally more distinguishable from whitecaps in the ACOLITE image, but overall highest distinction between all classes (seawater, whitecaps, and plastics) was seen in the TOA reflectance scene. Moreover, the plastic pixels' NDVI scores (Table 4.1) were most similar to what has been found in other research (e.g., Themistocleous et al. (2020)) when derived from TOA pixel values. The at-sensor reflectance imagery was therefore selected for subsequent application of spectral indices, which, additionally, would mitigate effects from AC processing.

Table 4.1: NDVI values of two plastic pixels, derived from differently pre-processed versions of the 20200519 WV2 scene. The maximum NDVI value corresponds to the brightest plastic pixel (i.e., highest fraction of plastic) in all cases. (*ACOMP processing was only available for a small subset and can thus not be adopted for analysis of other WorldView imagery).

Radiometric Processing	**Plastic Min. Value**	**Plastic Max. Value**
TOA Reflectance	-0.1338	-0.0606
ACOLITE	0.0493	0.0799
FLAASH	-0.0215	0.0402
*ACOMP**	*0.1042*	*0.1217*

Using NDVI values alone, the two plastic training pixels were clearly separable from surrounding waters and whitecaps in the training dataset (Figure 4.10). However, employing the NDVI values in Table 4.1 as upper and lower limits for further plastics detection resulted in a large number of false positives (i.e., whitecaps misclassified as plastic debris). On the basis of this observation, the dimensionality of the feature space was augmented to facilitate greater differentiation between classes. A number of different spectral indices were explored, including the Reversed WorldView Water Index (RWV-WI; Dominici et al., 2019), the Plastic Index (PI; Themistocleous et al., 2020), a Reversed Normalised Dif-

ference Water Index (RNDWI), and the WorldView Non-Homogeneous Feature Difference Index (WV-NHFD; Harris Geospatial Solutions, 2020) – all of which are described in Table 4.2. Using the training dataset, each index was evaluated individually, in which the following observations were made:

- The RWV-WI conveyed low variability in the water class, as expected, but poor distinction between plastics and whitecaps.
- The PI yielded the same results as the NDVI in terms of class separation, as both indices utilise the same bands (however, this observation contradicts findings in Themistocleous et al. (2020), where the PI demonstrated superior detection capabilities of plastic debris relative to the NDVI).
- The RNDWI largely separated the classes but with a slight overlap of plastics and whitecaps.
- The WV-NHFD resulted in highest values for whitecaps as well as no distinct clustering of classes.

Based on this, the RNDWI was chosen to extend the detection task to a two-variable feature space (NDVI and RNDWI); however, whitecaps still prevented thresholds from being set without inducing the detection of numerous false positives. On account of this, a new spectral index was developed for the purpose of this study, specifically targeted at enhancing bright features on the water surface. The index, denoted the WorldView Whitecaps Index (WV-WCI), is based on spectral characteristics of the training data and endmembers derived from the PPI, where whitecaps and/or spume generally were found to exhibit an absorption feature around 608 nm (yellow band) and increased reflectance at 659 nm (red band) – effects that were unique to this class. Leveraging these spectral differences, the index was defined as

$$\text{WV-WCI} = \frac{R_{\text{RED}}}{R_{\text{RED}} + R_{\text{YELLOW}}} \tag{4.6}$$

where R_{RED} and R_{YELLOW} represent the reflectance in the red and yellow bands of the WorldView-2/-3 imager, respectively.

The remaining WorldView top-of-atmosphere imagery was then processed with three spectral indices: NDVI, RNDWI, and WV-WCI. Mapped in a three-variable feature space, plastic pixels showed sufficient clustering and class separability to define spectral index thresholds for detection of other potential plastics. Using the values of the known plastic pixels as a baseline, upper and lower index limits were determined through iterative thresholding and systematic inspection of the detected pixels' spectral responses (within the 20200519 WV2 image). The final ranges were set to $[-0.09, -0.05]$ for NDVI, $[-0.30, -0.23]$ for RNDWI, and $[0.46, 0.48]$ for WV-WCI, and only pixels conforming to all three ranges were classified as plastic debris.

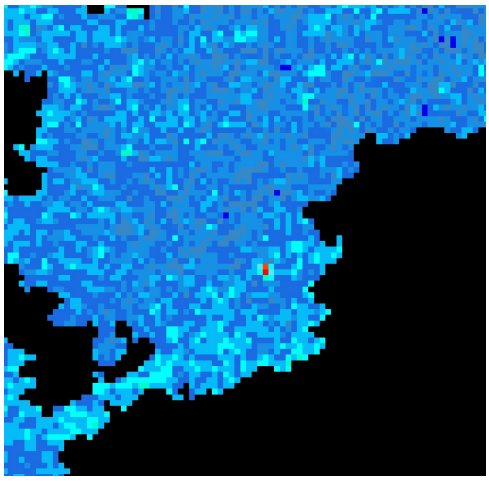

Figure 4.10: Assigning specific colours to discrete NDVI ranges allows for visual identification of spectral classes. Here, the plastic target can be seen in red and orange.

Table 4.2: Spectral indices tested on the WorldView imagery for detection of plastic debris.

$\text{NDVI} = (\text{NIR}_1 - \text{Red})/(\text{NIR}_1 + \text{Red})$	(1)
$\text{RNDWI} = (\text{NIR}_1 - \text{Green})/(\text{NIR}_1 + \text{Green})$	(2)
$\text{RWV-WI} = (\text{NIR}_2 - \text{Coastal})/(\text{NIR}_2 + \text{Coastal})$	(3)
$\text{PI} = \text{NIR}_1/(\text{NIR}_1 + \text{Red})$	(4)
$\text{WV-NHFD} = (\text{Red Edge} - \text{Coastal})/(\text{Red Edge} + \text{Coastal})$	(5)
$\text{WV-WCI} = \text{Red}/(\text{Yellow} + \text{Red})$	(6)

4.4.5 MTMF

Mixture Tuned Matched Filtering is a partial linear spectral unmixing approach for identifying pixels that are likely to contain some fraction of a target material. MTMF is implemented as a fully automated algorithm in ENVI, requiring only two parameters for input: 1) an image with uncorrelated noise and unit variance and 2) the spectral signature of a target endmember matching the space of the input image. These conditions can be met by applying an MNF transform to the imagery and endmember spectra.

The different pre-processing methods called for a decision of which imagery to use. For intercomparison across scenes, images should be on a common radiometric scale, which is only achievable through atmospheric correction when dealing with different sensor types. However, since the WorldView-2

and WorldView-3 satellites carry the same spectral instrument (WorldView-110 camera), the plastic endmember derived from the 20200519 WV2 image can also be used in units of radiance or TOA reflectance for input to other individual WV2 or WV3 scenes. The SPOT imagery, on the other hand, was not processed with MTMF. With only four spectral bands, these images are poor candidates for detection algorithms relying on accurate spectral information.

Image SNR (signal-to-noise ratio) was also investigated before and after atmospheric correction by utilising a sample of 600 randomly selected open ocean pixels. Since marine plastics concentrations generally produce a weak signal (Topouzelis et al., 2020), a high SNR is required to detect materials on subpixel scales (Martínez-Vicente et al., 2019). The detection capabilities of the WorldView sensor were assessed based on each band's SNR. As seen in Figure 4.11, estimates of image signal-to-noise ratio revealed an overall higher SNR value for non-atmospherically corrected imagery, potentially benefiting detection. However, as the TOA signal comprises both the true surface signal and signal from atmospheric contributions, the SNR estimates fail to show the correct significance for TOA data – particularly in the shorter wavelength channels where atmospheric scattering is more severe. In addition to this, Figure 4.11 shows that SNRs are similar for all radiometric pre-processing methods in the red edge and near-infrared regions (724-908 nm). Nevertheless, to attenuate possible errors arising from the atmospheric correction schemes, at-sensor (TOA) reflection data was employed for the MNF transform and MTMF algorithm.

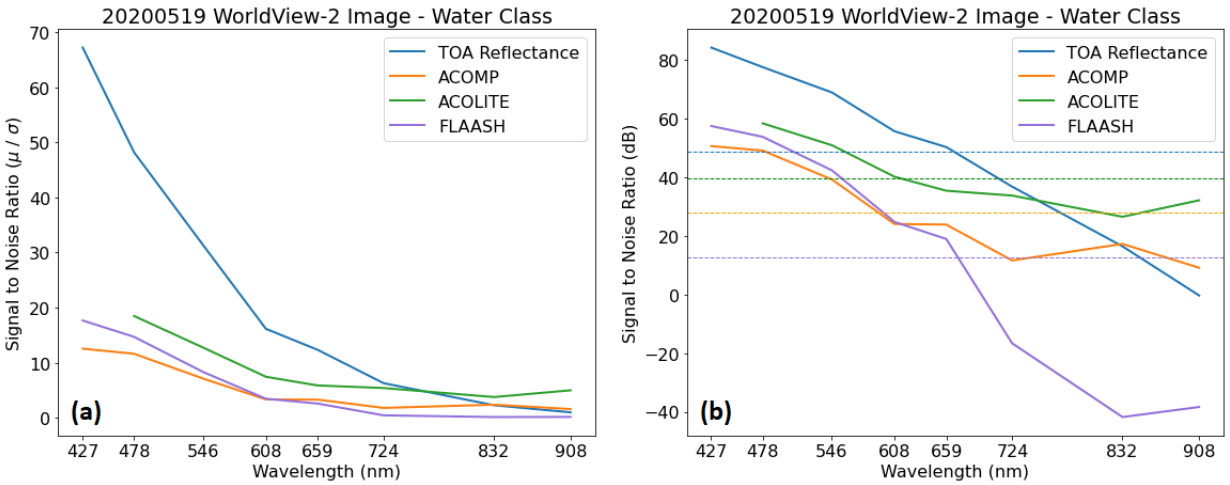

Figure 4.11: SNR calculated from a random sample of open ocean pixels for the different pre-processed 20200519 WV2 imagery, illustrated in (**a**) standard scale and (**b**) logarithmic decibel scale. The latter also indicates the mean SNR of all channels plotted as dashed lines in matching colour to their respective correction algorithm.

To project the data to MNF space, image noise statistics were estimated using the shift difference method. ENVI assumes that each pixel contains both signal and noise, and that each neighbouring pixel contains the same signal but with different noise (Harris Geospatial Solutions, 2020). The method therefore works best when noise statistics are gathered from homogeneous regions rather than from the entire scene. Consequently, the shift difference region was constrained using a 2000 × 1800 pixel subset from the 20200519 WV2 image, encompassing the single confirmed plastic event. A cloud mask was applied to the image to mitigate noise estimates from clouds and haze, removing roughly 43% of the pixels from the subset area. The resulting subset covered ~7.5 square kilometres of uniform[19] ocean cells, which was then used for the shift difference statistics extraction.

Although a dimensionality reduction of the MNF data can improve results by removing ineffectual noise bands, this is generally not encouraged for multispectral imagery. Such a process can potentially eliminate usable information for a sensor of already few spectral bands and cause ambiguous results. For this reason, all 8 MNF bands resulting from the 8-band WorldView imagery were used for the subsequent MTMF algorithm.

In MTMF post-processing, the feasibility of matched filtering scores is evaluated against the corresponding infeasibility values. Using a two-dimensional scatterplot for visuals (an artificial example is given in Figure 4.12), the theoretical infeasibility threshold can be identified as a conical shape in which the properly classified pixels are contained (Figure 4.12, region **a**). However, previous research (Mundt et al., 2007; Mitchell and Glenn, 2009) indicates that the true positives rather fall within region **b** (Fig. 4.12), delineating an almost inverse relationship from what is theoretically expected.

Based on the MTMF results of the only known plastic target (presented in Section 5.6, Table 5.3; Figure 5.12), thresholds for minimum and maximum MF and infeasibility values were determined. Initially, the minimum matched filtering score and the maximum infeasibility threshold were set to 0.3 and 6.0, respectively, to facilitate detection of potential plastic pixels with mixed spectra. However, this resulted in the misdetection of several cloud outlines and hazy pixels. Because the removal of these artefacts can be difficult, especially in automated cloud masking algorithms, the MF threshold was adjusted to 0.49 to avoid such false positives. This way, the detected pixels would also have a higher chance of exhibiting spectral responses resembling that of plastics, given that no other ground truth was available for validation. In accordance

19. Notably, the spatial subset is not purely spectrally uniform and contains oceanic surface features such as waves and spume, in addition to the known plastic target. However, residual instrument noise (e.g., data striping) can be mitigated this way.

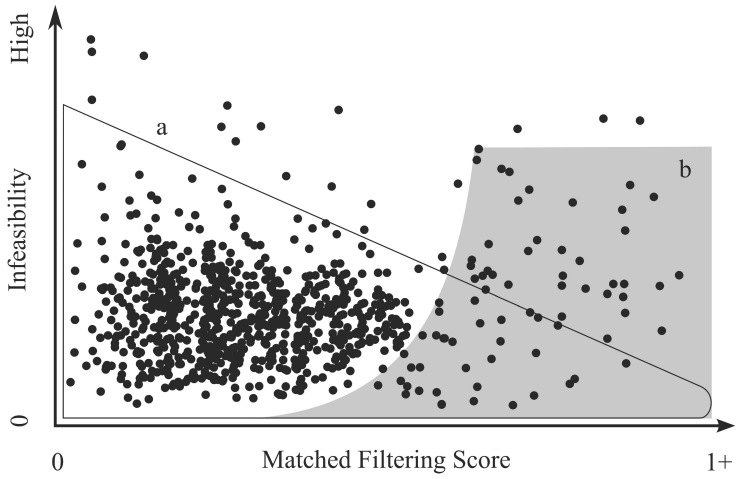

Figure 4.12: An example scatterplot of artificially generated MF scores and infeasibility values, where **a** denotes the theoretically expected region of correctly classified pixels. However, previous research suggests that the true target pixels instead fall within the shaded region, **b**, delineating a nearly inverse relationship to the theoretical region. Figure from (Routh et al., 2018).

with the MF threshold shift, efforts were made to investigate the effects of an increased maximum infeasibility value on the detected pixels' spectral signatures. Through iterative masking (based on various MT thresholds) and systematic inspection of resulting MTMF scatterplots and the detected pixels' spectral responses, the final infeasibility threshold was set to 8.5 – a margin below the closest hazy pixel detection with an infeasibility of 9.

Constrained by the MF and MT thresholds, the feasible region (blue shaded area in Figure 4.13) contained five pixels from the 20200519 WV2 image that were classified as containing plastic (these are illustrated and further discussed in Chapter 5). The detected pixels' spectral signatures revealed similar spectral characteristics to that of the plastic endmember. Thus, the determined thresholds were used for subsequent MTMF post-processing of the remaining imagery. Finally, using the pan-sharpened image, a training dataset comprising different ocean surface material classes was created to assess the separability of ocean surface features in terms of MTMF scores.

For the sake of exploration, MTMF was also applied to the atmospherically corrected data. Not unexpectedly, this method resulted in the detection of many false positives[20] (>0.49 MF score) with low infeasibility values, indicating that AC algorithms are immature for such detection tasks in large-scale open ocean imagery.

20. Based on validation from spectral response and visuals of pan-sharpened imagery.

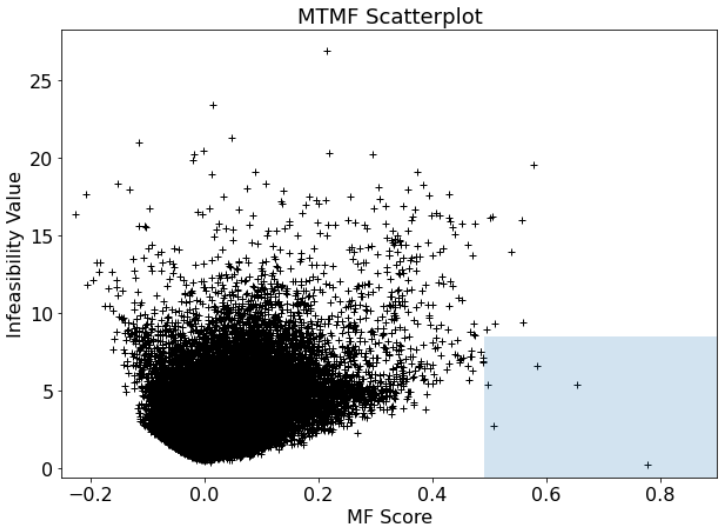

Figure 4.13: Scatterplot of MF scores versus infeasibility values from randomly selected pixels across the MTMF processed image. The pixels that fall within the shaded blue area are classified to contain plastic.

5

Results and Discussion

5.1 Movement of Floating Plastic Debris

In situ data for the satellite imagery included four GPS trackers attached to floating plastic debris. Three out of the four trackers were used to estimate the trajectory and speed of floating plastic patches, where the daily average debris speed was calculated for five individual days. As seen in Table 5.1, plastics' travelling speed ranged from 0.044 to 0.215 m/s with an overall average of 0.148 m/s or 12.8 km/day. Compared to the results from other research, where plastics' average travel speed was found to be 6 km/day (Kikaki et al., 2020), these findings present a speed that is approximately twice as high. However, since the study of Kikaki et al. was conducted in the Caribbean Sea over the course of five years, differences may arise from dissimilar spatial and temporal conditions.

During the debris tracking events, ocean surface currents appeared to have velocities ranging from 0.08 to 0.28 m/s and easterly winds were recorded with speeds of 4.9 to 8.3 m/s. In all five cases, the travelling plastics' speed was found to be lower than that of the currents', indicating that the debris' weight and partial submersion slows its pace. Moreover, the movement direction of the current seemed to be consistent with the direction of the debris. Using a simple regression analysis, the estimated speed of plastic debris was found to be highly correlated with currents' velocity ($R^2 = 0.91$, $p < 0.02$, $n = 5$), yet no correlation was seen between debris and wind speeds ($R^2 = 0.06$, $p > 0.05$, $n = 5$). These findings are in agreement with what was found in Kikaki et

Table 5.1: Estimated speed and direction of GPS tracked plastic debris with multiple recorded signals. The estimated debris speed is the tracker's average speed at the given date. Ocean currents and wind conditions are also presented, collected from the OSCAR and CMEMS databases and the Advanced Scatterometer (ASCAT MetOp-A), respectively.

Tracker ID	Date	Debris Direction	Debris Speed *m/s*	Currents Direction	Currents Speed *m/s*	Wind Direction	Wind Speed *m/s*
Tracker A	18/05/20	S	0.044	S	0.08	WSW	4.9
Tracker C	11/06/20	NNE	0.086	NNE	0.19	SW	7.4
Tracker D	01/07/20	NNW	0.215	NNW	0.27	W	5.1
	05/07/20	WNW	0.185	NW	0.25	W	6.3
	06/07/20	WNW	0.211	NW	0.28	W	8.1

al. However, due to the inconsistency between GPS tracker observations, any attempt at establishing a relationship between debris trajectory, ocean currents, and surface winds would have been subject to a high degree of uncertainty, and was thus deemed futile.

5.2 Spectral Behaviour of Marine Plastic Debris

The plastic conglomerate attached to Tracker B was used as a baseline for understanding the spectral behaviour of floating plastics. With fractional coverage of roughly six pixels, the target's abundance within each pixel was estimated using a higher-resolution panchromatic band. Next, spectral signatures of all six pixels were extracted to examine the influence of various seawater coverage on plastic detectability. The results, which are presented in Figure 5.1, showed a clear spectral distinction of the highest percentage plastic cover of 78% for the TOA reflectance, ACOLITE, and FLAASH imagery (ACOMP was not included due to slightly larger cell sizes and thus different fractions of plastic coverage). Spectral signal shapes were not consistent with various fractions of plastic, suggesting that individual pieces of debris were composed of different material colours and/or chemical compositions. Moreover, sea foam or sun glint may have altered spectral responses in pixels with lower plastic abundance. Consequently, plastic debris can be challenging to identify, particularly for cell abundances below ~50%. Nevertheless, mixed plastic pixels were found to be distinguishable from seawater in all cases.

The six plastic pixels were plotted in a two-dimensional scatter plot to visualise their relative distribution using the green and NIR1 band as plot axes. Theoretically, mixed pixel cells comprising various fractions of any two endmembers

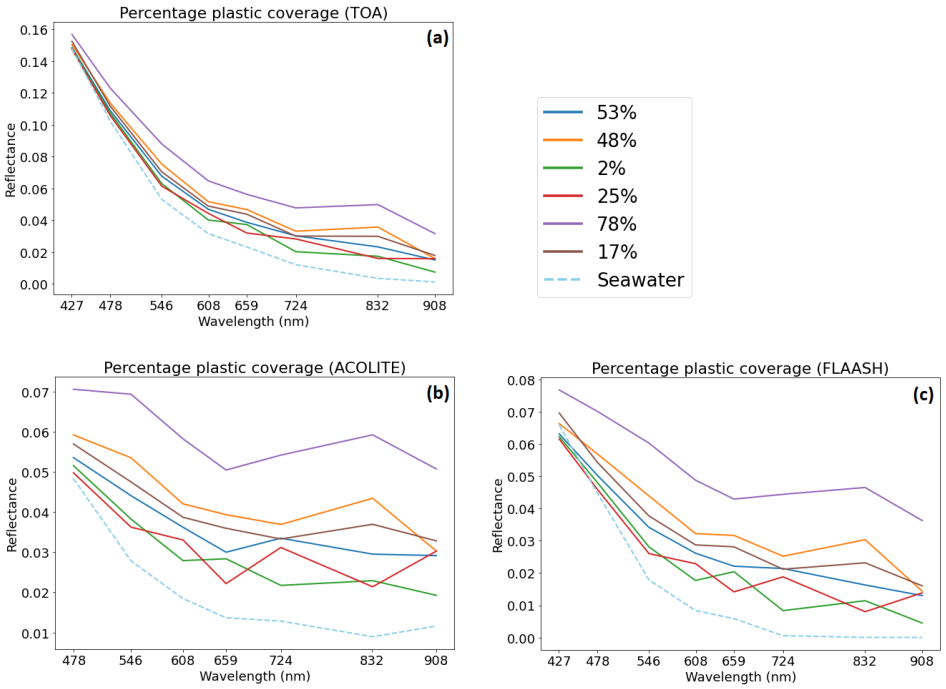

Figure 5.1: Percentage pixel coverage of the plastic target captured by the WorldView-2 imager and matching pixel spectra from three different radiometric corrections: (**a**) Top-of-atmosphere reflectance, (**b**) ACOLITE, and (**c**) FLAASH.

will occur between the two extremes, as the spectrally purest pixels always form the corners of the data cloud. As seen in Figure 5.2, the mixed pixels exhibited a nearly linear relationship, where the strongest plastic pixel (E, 78%) formed one vertex of the data, homogeneous seawater pixels formed a second, and all other instances fell in between. However, since a pixel's fractional coverage directly corresponds to its position between the two endmember spectra, the plot revealed potential errors in the plastic abundance estimation. In theory, pixel A, which was estimated to 53% plastic coverage, should plot as the closest data point to pixel E, but was instead positioned at the lower end of the data cloud. Similarly, pixel F, estimated to comprise 17% plastics, was located directly between pixel E and the water endmembers - indicating either a mixture of a third endmember or a substantially fuller plastic coverage. Compared to their respective spectral signatures in Figure 5.1, pixels A–F appear in consistent order from strongest signal intensity to lowest (i.e., the same order as demonstrated in Fig. 5.2). Thus, it is highly likely that the fraction calculation was erroneous to some degree, but the propagation of error was mitigated by only considering one of the samples in subsequent processing.

Endmember extraction was conducted using a combination of two methods: the Pixel Purity Index (PPI) for derivation of open ocean endmembers and inverse

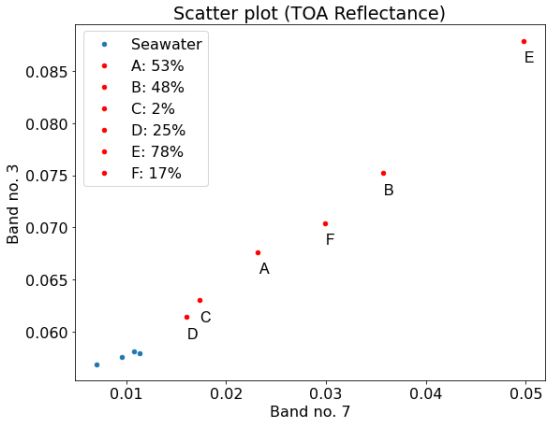

Figure 5.2: Scatter plot image bands as plot axes, showing the nearly linear distribution of mixed plastic pixels with calculated abundance estimations. Pure seawater pixels are seen in blue. The pixels were extracted from the TOA reflectance image and plotted with respect to the green and NIR1 bands.

spectral unmixing for calculation of pure plastic spectra. Due to the limited availability of ground truth data, endmember extraction of plastic targets was only attempted on the 20200519 WorldView-2 image, using pixel E only on account of its superior plastic abundance. As seen in Figure 5.3, derived plastic endmember spectra show a similar spectral response to that of the mixed pixel, with differentiation mostly in the intensity and not in the shape of the signal. Inaccuracy in cell abundance estimations is thus of less significance for the result, as the spectral shape largely remains intact given an increase of 22 percentage points.

Results from this study demonstrate that floating plastic debris has a significant reflectance feature in the NIR, not only for pure spectra but also for mixed pixels of various proportions (Fig. 5.1). These findings are consistent with previous research (e.g., Biermann et al., 2020). A slight spectral peak is also seen in the green band, indicating that the dominant colour of the floating materials is indeed green. Clear seawater characteristically absorbs in the NIR channels and exhibits strongest reflectance in the visible region - particularly in the blue bands - as expected. Furthermore, the water class shows low inherent variability in reflectance properties (Fig. 5.3).

The level of uncertainty related to the plastic spectral signature is possibly attributed to numerous different factors. With only a few pixels of ground truth, all of which were mixed with different fractions of seawater, the standard deviation of plastic targets could not be estimated to a satisfactory degree of accuracy (such calculations are typically challenging for small targets with a scarce spatial distribution). Moreover, the inverse spectral unmixing process

is a deterministic equation, meaning that additive noise[1] has been excluded in the derivation of plastic endmember spectra. In addition, the plastic coverage estimation did not account for potential partial submersion of the target, which would likely have an impact on the spectral response. The relationship between degree of submersion and reflectance properties of plastics cannot be thoroughly investigated in a study of this nature, yet evidence is seen that seawater presence in mixed pixels will lower the magnitude of reflectance while mostly retaining the spectral shape. Also, the shape and intensity of the signal are largely affected by atmospheric correction algorithms, which is further addressed in the following section.

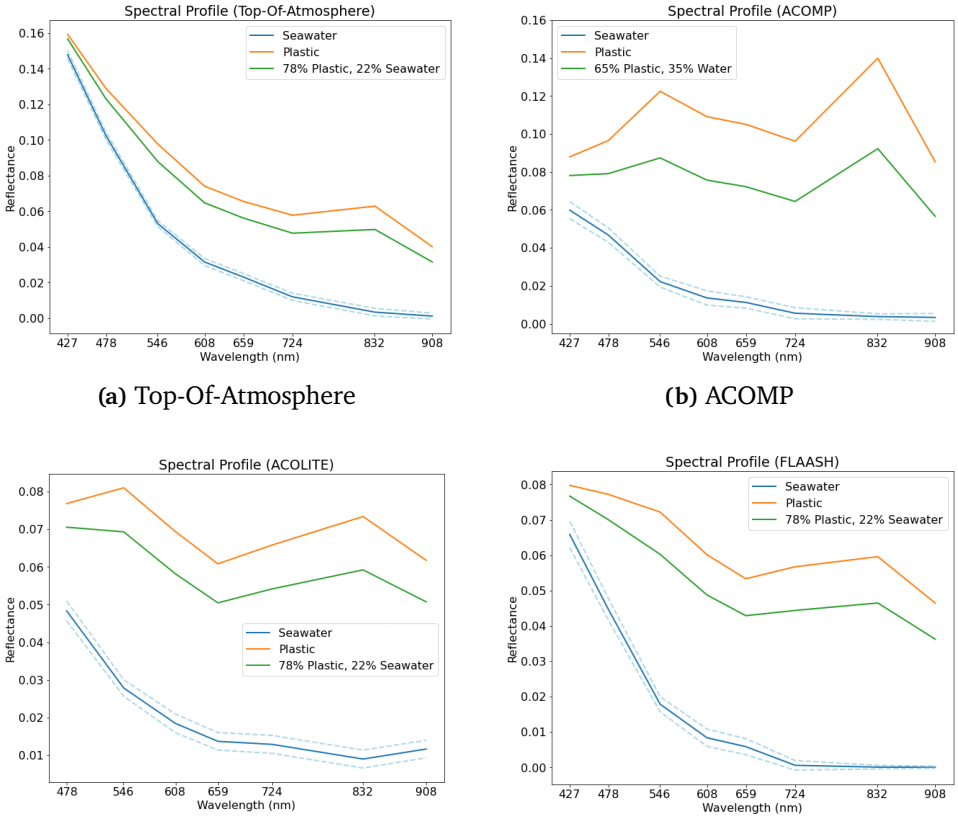

(a) Top-Of-Atmosphere **(b)** ACOMP

(c) ACOLITE **(d)** FLAASH

Figure 5.3: Results of the inverse spectral unmixing approach in which plastic endmembers were derived for four different radiometric corrections. The dashed blue line represents standard deviation of the water class (standard deviations for plastics could not be derived due to limited ground truth pixels).

1. Additive noise effects in remote sensing imagery are typically independent of the data and can generally be represented as a Gaussian distributed, zero-mean process.

5.2.1 Effects of Atmospheric Correction

Top-of-atmosphere reflectance of the plastic endmember was higher than bottom-of-atmosphere products in the coastal blue and blue channels as expected. However, the TOA plastic spectrum had the second lowest reflectance in the NIR, after FLAASH. From the spectral plot in Figure 5.4a, it is evident that the different AC algorithms have significant impacts on the resulting spectral signatures and thus also on detection schemes. The ACOMP product had notably higher reflectance compared to both the ACOLITE and FLAASH data, particularly in the NIR, which was also the band exhibiting overall strongest signal. FLAASH and ACOLITE produced plastic spectra that were more similar in shape, though the FLAASH data was slightly lower in magnitude. In contrast, water endmember spectra (Fig. 5.4b) were highest in intensity for ACOLITE, followed by ACOMP and FLAASH, respectively. FLAASH obtained zero to negative reflectance values from the red edge to the near-infrared (negative values were corrected to zero for the plot), while ACOLITE showed an irregular increase in signal intensity around 908 nm. The latter indicates either an error in processing or in endmember selection, as this is a nontypical behaviour for oceanic spectra – a target generally recognised as dark in the NIR and SWIR regions. Compared to a USGS[2] spectral library signature of open ocean, all three seawater spectra were of lower magnitude – an effect which may be owing to different illumination conditions.

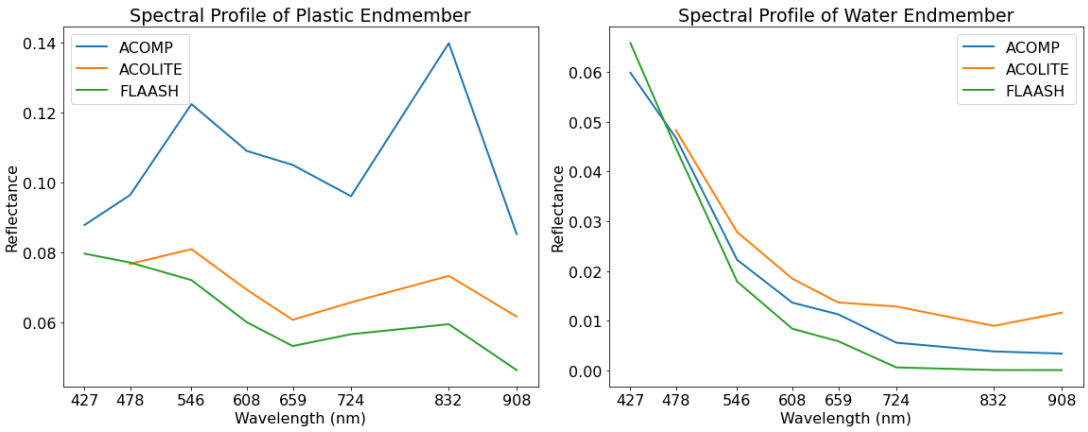

(a) **(b)**

Figure 5.4: Spectral plots of (**a**) plastic and (**b**) water endmembers using three different atmospheric corrections.

Unbiased percentage differences at different wavebands (Table 5.2) varied from 1% to 81% with pairwise comparison of AC algorithms. These differences were highest in the NIR band centred around 833 nm, where the ACOMP to FLAASH

2. https://www.usgs.gov/labs/spec-lab/capabilities/spectral-library

comparison peaked at 81%, compared to FLAASH/ACOLITE at 21%. Lowest percentage differences were seen in the blue band (478 nm), spanning 1–23% (not considering the coastal blue band, which was excluded from the ACOLITE imagery). The spectral average UPD ranged from 15–50% and was, by a large margin, lowest in the FLAASH/ACOLITE comparison.

Table 5.2: Unbiased percentage differences between ACOMP, ACOLITE, and FLAASH bottom-of-atmosphere corrected spectra of the confirmed plastic target. UPD could not be computed for the coastal blue band in comparisons involving ACOLITE, due to the removal of this band during processing.

Wavelength (nm)	ACOMP / FLAASH (%)	ACOMP / ACOLITE (%)	FLAASH / ACOLITE (%)
427	10	–	–
478	22	23	1
546	52	41	12
608	58	45	14
659	65	53	13
724	52	37	15
833	81	62	21
908	59	32	28
UPD Average	50	42	15

Although the comparison between FLAASH and ACOLITE shows the lowest unbiased percentage difference, this does not mean they obtained the most accurate results. But as no reference data is available, the 'best' algorithm cannot be determined. Additionally, low availability of ACOMP data prevented further assessment of this particular AC processing. However, all three atmospheric correction algorithms (ACOMP, FLAASH, ACOLITE) evaluated at the confirmed plastic target suggest that floating plastic debris can indeed be detected and is also spectrally distinct from seawater. Future studies should further assess how atmospheric correction algorithms affect plastic spectral responses in terms of shape and intensity, but results seen here suggest that removing environmental perturbations from the signal enhances characteristic reflectance and absorption features rather than masking them.

5.2.2 Class Spectral Separability

Distinguishing plastics from seawater is essential for detection, but water is not the only material class influencing remote sensing of marine plastic debris. Whitecaps, spume, algae, coloured dissolved organic matter, and timber, all of which have individual spectral characteristics, can affect and potentially compromise the detection of plastics. Accuracy in derived endmember spectra,

as well as sufficiently high spectral resolution, is therefore of utmost importance to account for the influence of other sea surface targets. Although *in situ* measurements of these materials were not available for this study, future missions should gather such information for a detailed assessment of class separability.

Despite limited ground truth data on other ocean bright targets, plastics were investigated for their discrimination from whitecaps/wave crests – a common source of false positives present in most open ocean imagery. Using spectral signatures derived from the PPI and n-D Visualizer, an endmember signature for whitecaps was identified[3] and compared to the derived plastic endmember spectra (Figure 5.5). Although whitecaps were found to have a significantly different spectral shape than that of plastics, they also, similar to plastics, exhibited a spectral peak in the NIR. However, spectral response of whitecaps were of overall lower intensity and showed additional strong absorption around 608 and 724 nm (yellow and red edge bands, respectively). Results seen here suggest that plastics can indeed be distinguished from whitecaps, although further analysis including target variability is advised for future research.

Class separability of plastics, seawater, and whitecaps was also evaluated using two-dimensional scatter plots (Figure 5.6). With spectral bands as plot axes, a rigorous inspection of all band combinations was carried out to determine the two best channels for enhancing class distinction. These were found to be the blue (478 nm) and NIR 1 (833 nm) bands, which was an unexpected result given the apparent proximity of spectral response for whitecaps and plastics in the blue band (Fig. 5.5). However, it should be noted that whitecaps exhibited large inherent variability (as observed from the scatter plots) – a factor that is unaccounted for in endmember spectra.

Plastics did not show signs of clustering, but as only two pixels were evaluated (pixels B and E (Fig. 4.8), with an estimated plastic abundance of 48% and 78%, respectively), no hard conclusions can be drawn. However, Figure 5.6 demonstrates that plastics are distinguishable from the water and whitecaps classes even when mixed with fractions of seawater. Excluding the ACOMP subset (this image was evaluated on a separate training dataset due to a larger cell size), no major differences were observed between the BOA and TOA imagery in terms of class separability.

3. Identification of spectral signatures was conducted using supervised classification.

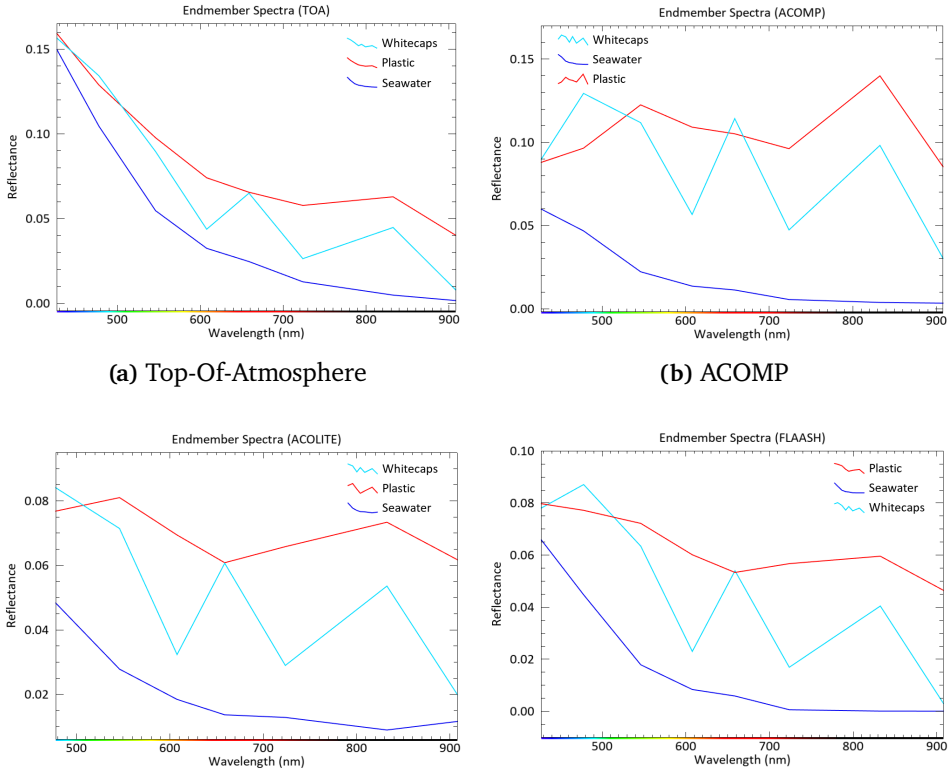

(a) Top-Of-Atmosphere **(b)** ACOMP

(c) ACOLITE **(d)** FLAASH

Figure 5.5: Endmember spectral signatures of seawater, whitecaps, and floating plastics, derived from the WorldView-2 20200519 image using four different radiometric corrections.

5.3 Linear Interpolation and Anomaly Detection

Linear interpolation and subsequent RX anomaly detection were conducted on both the SPOT and WorldView imagery with associated GPS trackers (excluding the 20200519 WV2 image in which the plastic target was visually identified). The linear interpolation alone provided no immediate detections (i.e., likely plastic patches could not be pinpointed), which was an expected result given the dynamic nature of ocean currents and winds. At most, the closest GPS tracker recording was made 3 hours and 3 minutes post-image capture (WV2 20200611 and WV3 20200701 images), while the shortest delay spanned roughly 10 minutes (SPOT-6 20200727)[4]. Anomalies were detected in all three SPOT scenes (as illustrated in Figure 5.7), while for the WorldView images, only one of three contained positive anomaly detections (Figure 5.8). Despite interactive inspection of spectral signatures from all visually distinct pixels surrounding

4. See Section 3.3 for details on GPS trackers.

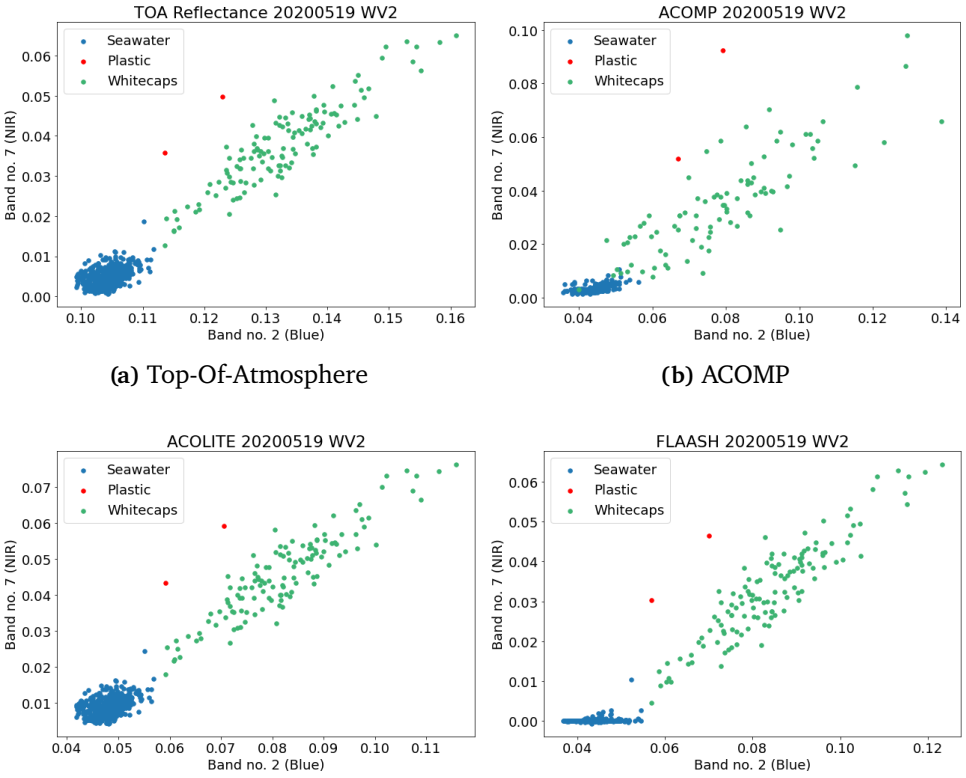

(a) Top-Of-Atmosphere **(b)** ACOMP

(c) ACOLITE **(d)** FLAASH

Figure 5.6: Two-dimensional scatter plots demonstrating class separability of seawater, whitecaps, and floating plastics, using the Blue and NIR1 bands of different pre-processing schemes as plot axes. The two plastic samples represent pixels B and E from the plastic abundance calculation, while the seawater and whitecap regions were manually identified in the multispectral imagery (the pan-sharpened image was used to aid visual interpretation but not for extraction of pixel values).

the estimated tracker positions, no evidence of additional plastic pixels was observed.

Of the three SPOT scenes in Figure 5.7, the anomalous pixels in the SPOT-7 20200705 image (Fig. 5.7b) were the only detections exhibiting plastic-like spectral characteristics. A sharp peak is seen in the NIR channel for both signatures[5], which is typical for marine plastic debris but also for photosynthetic plant material (e.g., seaweeds and algae). The image spatial resolution of 6 m indicates that the two neighbouring outliers encompassed a total area of 72 square metres, and with no records of the GPS-tracked plastics' physical

5. Since atmospheric components were not removed from the spectra, their BOA equivalents would typically have been lower in overall intensity.

dimensions (these can also vary over time), this study cannot confirm nor reject the anomalies as potential plastics based on the target's spatial extent. Its proximity to the estimated tracker position, as well as drift direction parallel to sea surface currents, strengthens the plastic hypothesis, albeit not to a degree of validation. Without *in situ* data, a minimum requirement for viable detections of small targets would be a sensor with higher spectral and/or spatial resolution, in addition to a robust atmospheric correction algorithm. However, the SPOT instruments could prove useful in detection tasks of larger plastic aggregations provided a sensor-specific plastic endmember was available for verification.

Three anomalies were detected in the WV2 20200611 image (Fig. 5.8**b**), whereas no spectral outliers were found in the remaining two WorldView scenes. The latter is possibly attributed to heavy cloud cover near the estimated positions (5.8**a**; 5.8**c**), obstructing the view of the plastic patches. For the WV3 image, specifically, another reason for the null result could be a strong presence of whitecaps/wave crests, compromising the anomaly detection by overestimating the sample mean vector (i.e., spectrally distinct targets are interpreted as background due to target overabundance). As for the three anomalous pixels in Fig. 5.8**b**, spectral signatures were of overall lower intensity, particularly in the near-infrared, compared to the derived plastic endmember. A slight increase in the NIR1 channel was observed for two of the anomalies, as well as similar spectral shapes to that of known mixed pixels (Fig. 5.1). Given the image spatial resolution of 4.2 metres, detected anomalies – if plastics – are likely to be mixed with various fractions of seawater.

The detected anomalies exhibiting similar spectral characteristics to that of known plastic spectra could potentially be used in the identification of other mixed pixels (e.g., using SAM classification). However, due to time constraints, it was not possible to explore such a method further in this study.

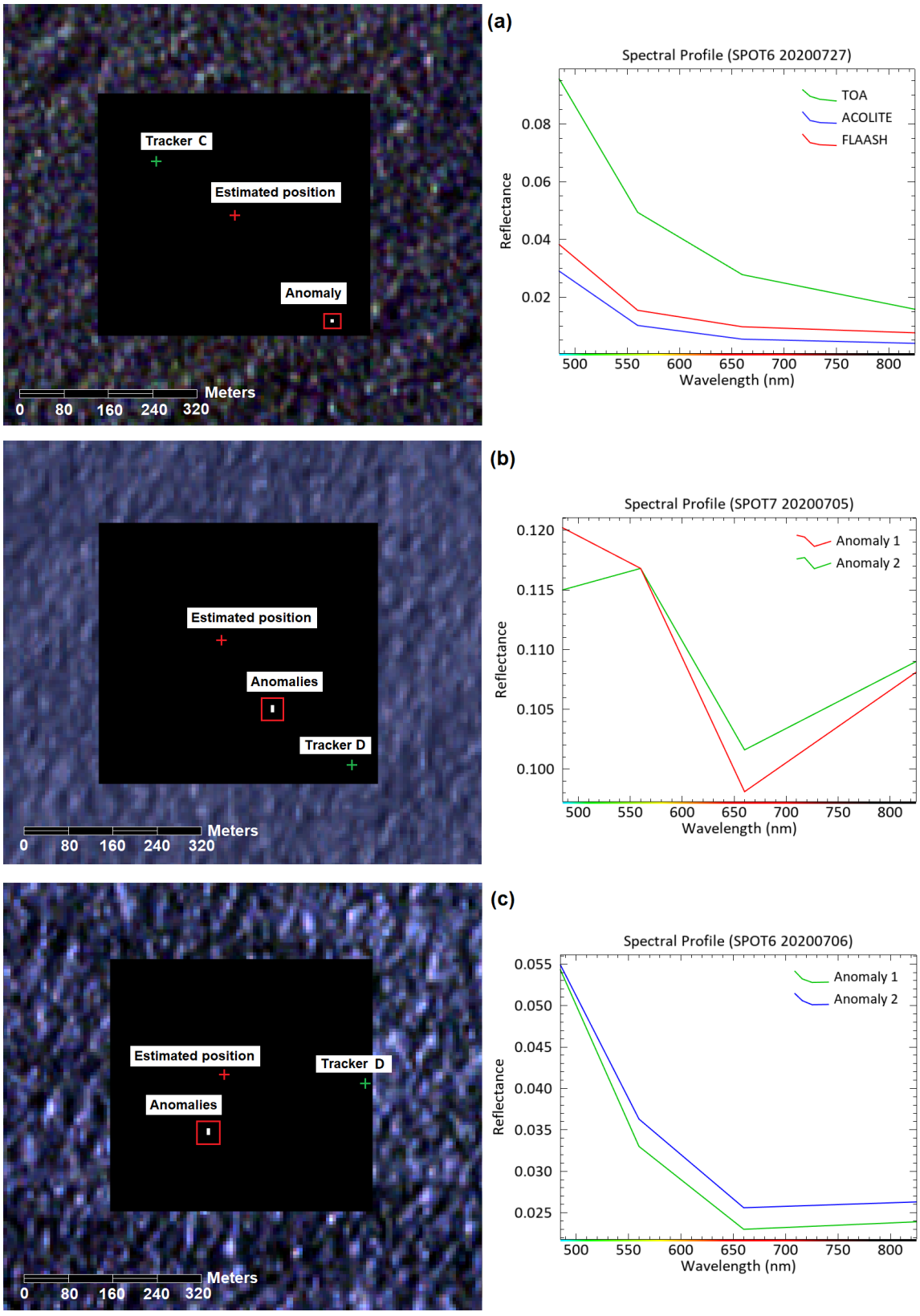

Figure 5.7: Anomaly detection using the SPOT imagery, specifically (**a**) SPOT-6, 20200727; (**b**) SPOT-7, 20200705; (**c**) SPOT-6, 20200706. The red markers indicate the estimated tracker positions through linear interpolation/extrapolation, while the green markers represent the closest recorded GPS position. Spectral signatures associated with the anomalous pixels are illustrated to the right, in which one, two, and two anomalies were detected in image **a**, **b**, and **c**, respectively. *©Airbus DS/Spot Image 2020.*

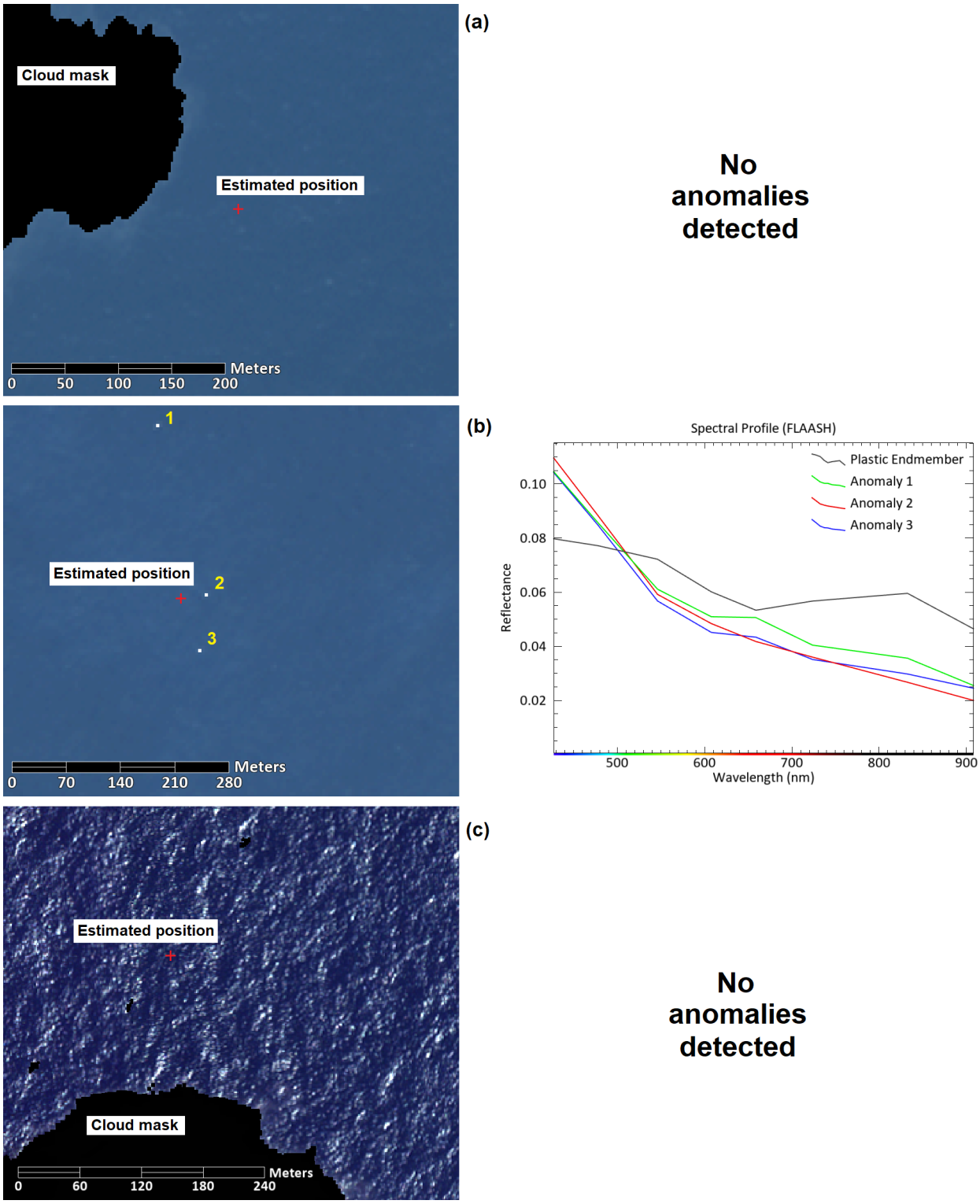

Figure 5.8: Anomaly detection using the WorldView imagery, specifically (**a**) WV2, 20200518; (**b**) WV2, 20200611; (**c**) WV3, 20200701. Anomalous pixels were only detected in image (**b**). *WorldView-2/3 ©2020 DigitalGlobe, Inc., a Maxar company.*

5.4 SAM Classification

In total, the Spectral Angle Mapper classified 237 pixels as plastic across the four multispectral WorldView images (see Table 5.5 for details). Pixels identified per image ranged from 2 to 138, with fewest detections in the 20200518 WV2 image and most in the 20200701 WV3 scene. Although most potential plastics were identified in the image of highest spatial resolution (1.3 m), the number of detections was not correlated to pixel cell size. Of the six pixels covering the known plastic target in the 20200519 image (Fig. 4.8), one was classified as plastic (pixel E).

Despite the high number of classified pixels, inspection of their respective spectral signatures indicated that the majority actually were whitecaps and/or sun glint rather than potential plastics. Two reasons for this can be identified: i) overestimation of the spectral angle threshold and ii) the pixels' mixture model. Since most floating plastic aggregations are relatively small targets, the majority of pixels containing plastic will be mixed. Thus, for the SAM classification to be successful, the spectral angle threshold must be determined such that it classifies even partial plastic pixels as plastic, but also such that other sea surface features are not falsely interpreted as the target material. Despite rigorous inspection of classification results with associated rule images, no evidence that such a threshold exists for the given data was found.

The SAM was able to detect the mixed pixel of 78% plastic abundance with the specified threshold of 0.09 radians, yet none of the other known plastic pixels were classified. This observation is likely attributed to the fact that the input endmember was derived from that exact pixel, and it also indicates that plastic targets must cover a large portion of a given pixel (>50–70%) to be within the classification threshold limit. With low availability of input endmember spectra, in addition to inadequate image spatial resolutions, SAM classification did not yield useful results for the available datasets and is likely more suitable in the detection of larger targets.

5.5 Spectral Indices

Using the Normalised Difference Vegetation Index (NDVI) alone, mixed plastic pixels (B and E, Fig. 5.12) were distinguishable from seawater and whitecaps in the training dataset (Figure 5.9). However, as the entire plastics class was based on only two samples, both of which were mixed with seawater, the inherent variability may not depict a true representation of the plastics class as a whole. It should also be noted that the NDVI values related to the TOA reflectance data cannot be directly adopted for use with imagery of other sensors (as different

atmospheric conditions are not addressed and corrected for). Despite this, pixels' NDVI scores of different atmospheric corrections (Table 4.1) were not in absolute agreement, suggesting that AC algorithms in this part of the ocean are underdeveloped for establishing strict spectral index thresholds. Consistency in radiometric pre-processing is therefore considered crucial for detection tasks across multiple sensor products, and although TOA data was selected for the spectral index analysis in this study, intercomparison campaigns with other AC products (e.g., ACOLITE) are needed to further assess the viability of various pre-processing methods.

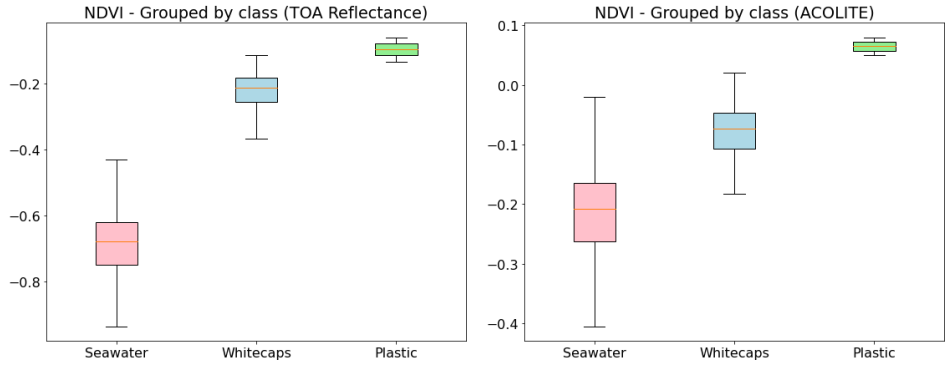

(a) **(b)**

Figure 5.9: Boxplots of classified materials on the sea surface using the NDVI. Calculated on the TOA reflectance image (**a**), we see that clear seawater, whitecaps, and plastics occupy distinct NDVI ranges. When using the ACOLITE image (**b**), the seawater and whitecaps classes largely overlap, while the plastics appear distinguishable.

Although the NDVI method can be useful in delineating plastics from water, it should be noted that its values are sensitive to variable environmental and observing conditions (e.g., aerosols and solar/viewing geometry; Hu, 2009). Such conditions can not only affect the visual contrast between plastic targets and water pixels, but also change their absolute NDVI values. Thus, a manual colour stretching of individual scenes is often required to account for these effects (Hu and He, 2008), making it difficult to implement a robust NDVI detection scheme in larger regions (such as the Pacific Ocean). Extensive testing and high-quality *in situ* data is necessary to explore this method further.

Using a three-variable feature space (Fig. 5.10 c–d), plastic pixels were detected by leveraging NDVI values against two other band ratios: the Reversed Normalised Difference Water Index (RNDWI) and the WorldView Whitecaps Index (WV-WCI) – the latter of which was specifically developed for this study. Detections were constrained by threshold ranges in each of the three band ratios, and only the pixels contained within all three ranges were classified as potential plastics. This resulted in the detection of three pixels for the 20200518 WV2

image, 18 pixels for the 20200519 WV2 image, and 29 pixels for the 20200701 WV3 image (Table 5.5). No pixels were detected in the 20200611 WV2 scene, which may be attributed to its lower spatial resolution (4.2 m) relative to the other imagery, causing possible mixed plastic pixels to be below detectable limits.

The detected pixels' mean spectral signatures were extracted individually for each scene and compared to the derived plastic endmember spectra. As seen in Figure 5.11, spectral shapes were most similar to the plastic endmember signature in the 20200519 and 20200701 images, albeit with a lower intensity. The mean spectral response of the three pixels detected in the 20200518 scene, however, was larger in magnitude relative to the endmember spectra. Moreover, their response exhibited an increased reflectance in the visible channels, particularly in the blue and red – a spectral behaviour that was typically seen for whitecaps in the WorldView imagery, but could also be a result of differently coloured plastic materials. Notably, all mean spectra for detected plastics had characteristic reflectance peaks in the NIR.

In the different spectral indices that were tested (Table 4.2), seawater was distinguishable from plastics in all cases. The detection problem is therefore mainly restricted to separating marine litter from other bright targets on the ocean surface. When evaluated on a training dataset, the NDVI alone demonstrates distinct ranges for seawater, whitecaps, and plastics, but for classification of the scene in its entirety, additional spectral indices were required to discriminate between plastic targets and other surface features. Indeed, the accuracy of the training data could affect the initial results seen in Figure 5.9 and Figure 5.10, and although it was not attempted here, a larger dataset of high-quality training samples should be employed to further capture class variability across the whole image. Furthermore, it may be beneficial to quantify each index' capability of detecting marine plastic litter (e.g., by using an objective sensitivity analysis as done in Themistocleous et al. (2020)) for improved validation of their performance. Nevertheless, results obtained here suggest promising detection abilities using the three-variable spectral index method, based on the spectral information of identified targets (Fig. 5.11).

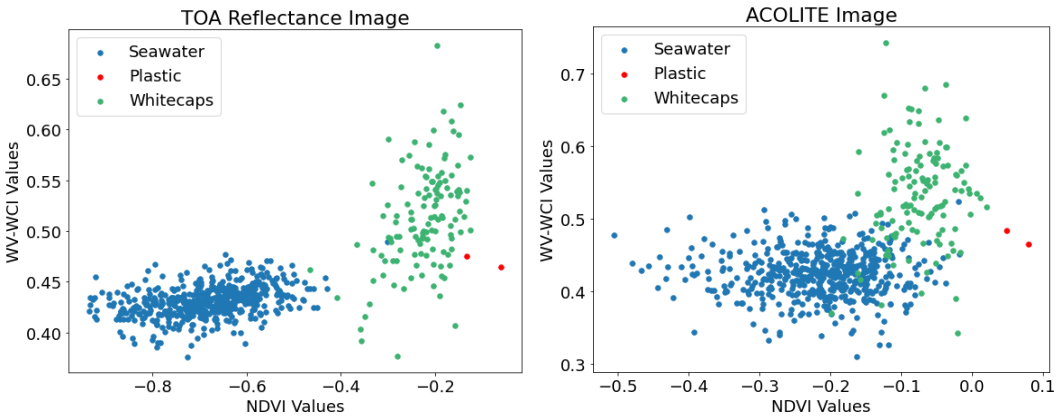

(a) TOA, 2-D **(b)** ACOLITE, 2-D

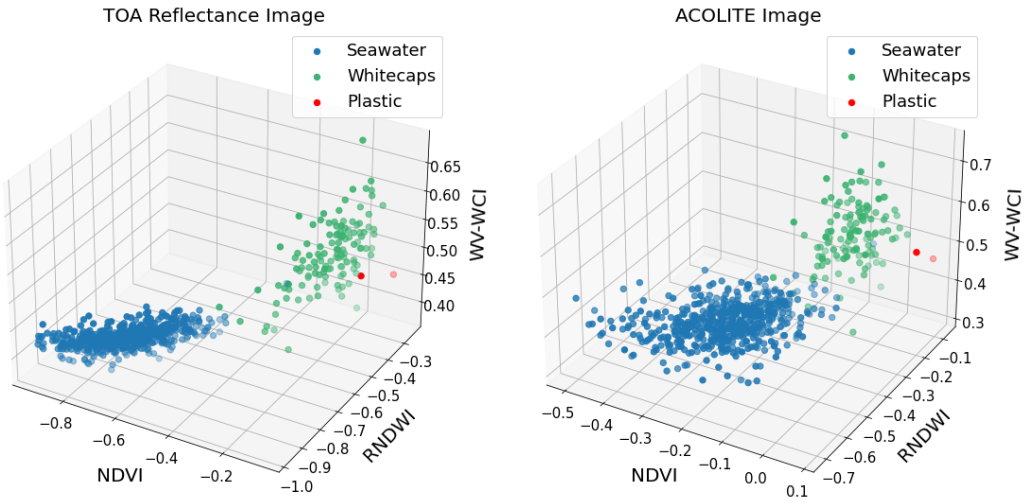

(c) TOA, 3-D **(d)** ACOLITE, 3-D

Figure 5.10: Two- and three-dimensional scatter plots illustrating class separability using spectral indices (20200519 WV2 image). Evaluated on a training dataset of 545 water pixels, 127 whitecaps pixels, and only two (mixed) plastic samples, the ACOLITE image demonstrates slightly higher distinction for plastics, yet lower overall separability between all three classes.

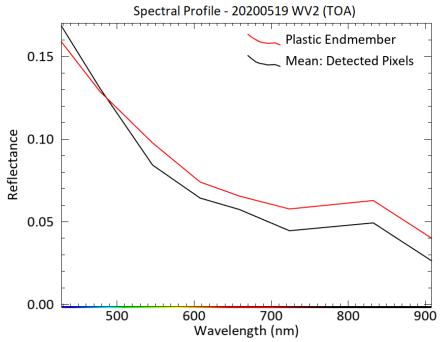

(a) TOA, 20200519 WV2

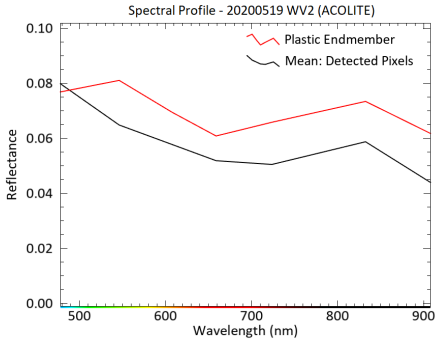

(b) ACOLITE, 20200519 WV2

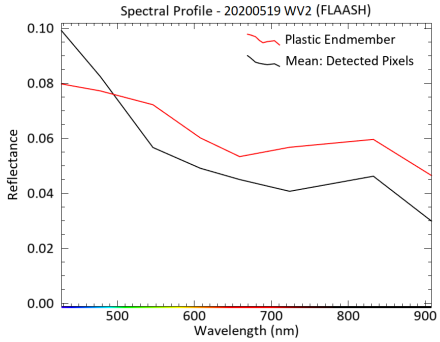

(c) FLAASH, 20200519 WV2

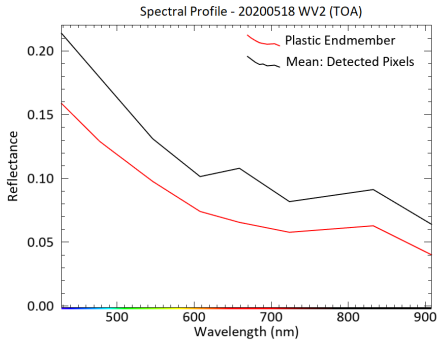

(d) TOA, 20200518 WV2

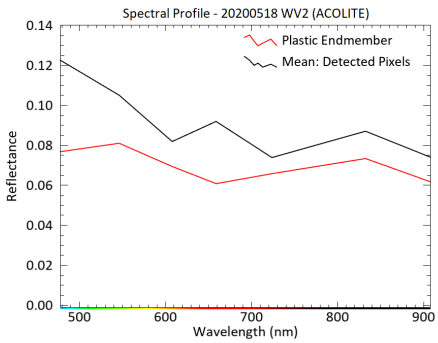

(e) ACOLITE, 20200518 WV2

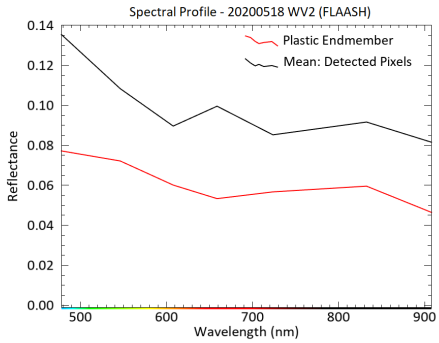

(f) FLAASH, 20200518 WV2

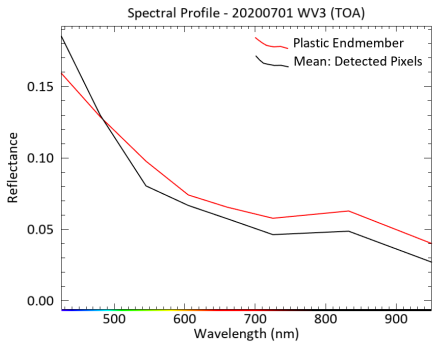

(g) TOA, 20200701 WV3

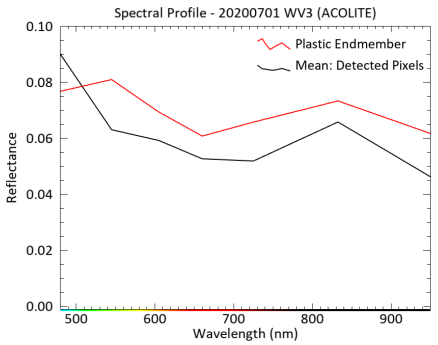

(h) ACOLITE, 20200701 WV3

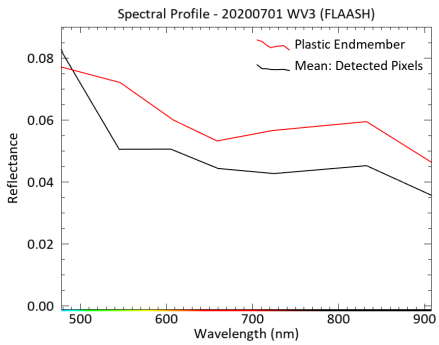

(i) FLAASH, 20200701 WV3

Figure 5.11: Mean spectral signatures (black) of detected plastic pixels in three WorldView images. The derived plastic endmember spectra (red) have been plotted for comparison.

5.6 Spectral Unmixing – MTMF

The endmember derived from the reversed spectral unmixing process was used for MTMF classification of all four multispectral WorldView scenes. In order to compare MTMF performance with estimated abundance fractions, results were first evaluated for the known plastic target, from which the endmember signature was extracted. The results for the six pixels covering the GPS tracked plastic cluster are presented in Table 5.3.

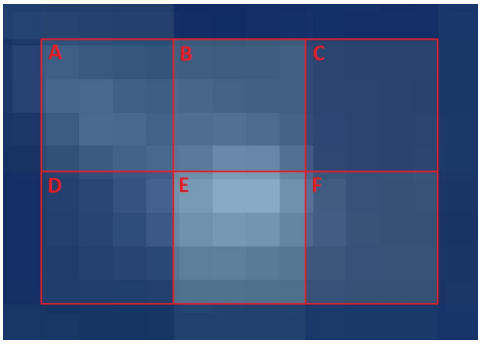

Figure 5.12: Pixels used for plastic abundance estimation of known target.

Pixel Name	Estimated Plastic Coverage	MF Score	Infeasibility Value
A	53 %	0.39	3.9
B	48 %	0.50	5.3
C	2 %	0.17	4.1
D	25 %	0.34	5.4
E	78 %	0.78	0.2
F	17 %	0.39	3.2

Table 5.3: Percentage calculation of the plastic coverage in each WV2 pixel with associated matched filtering and infeasibility scores.

Pixel E (Figure 5.12), used for the endmember derivation, obtained an MF score of 0.78 (equivalent of 78% plastic coverage) as expected. However, the remaining pixels' abundance were either over- or underestimated according to their respective MF scores. This observation is possibly attributed to two main factors: degree of wetness and degree of dispersion in the plastic target. As this cannot be estimated from the imagery without *in situ* data, the plastic coverage estimation does not account for partial submersion or debris density. Such properties can affect the spectral characteristics of plastic, e.g. produce a weaker signal in the NIR channels than what is expected or induce a uniformly lower reflectance for all bands. As seen in Table 5.3, the cell containing the second highest abundance calculation (pixel A, 53%) produces a lower MF score than its adjacent pixel B, estimated at 48% plastic coverage. This could be due to a higher degree of dispersion or a partial submersion of the plastic in pixel A, but it could also be a result purely arising from inaccuracy in the abundance estimation.

The results in Table 5.4 were also used as a baseline for determining classification thresholds. Maximum infeasibility score was set to 8.5 as a result of iterative testing, in accordance with previous work (Mundt et al., 2007; Routh et al., 2018) that demonstrates an increased threshold for high-coverage targets. To prevent cloud outlines and hazy pixels from being falsely classified as

plastics, it was necessary to set the minimum MF score to 0.49. Theoretically, such a high value results in the mapping of high percent cover plastics but also increases the risk of not detecting true positives (e.g., pixels A, C, D, and F are excluded from detection). Depending on the image spatial resolution, smaller plastic patches can go undetected. As no ground truth data was available for validation of classification, it was decided, for the purpose of this study, to only target high coverage pixels that could be partially validated through their spectral signatures. However, for projects involving the directional guidance of a vessel for cleanup, this study suggests decreasing the matched filtering threshold and to interactively inspect detections.

In total, eight pixels across the four multispectral WorldView images were classified as containing plastic. As seen in Table 5.4, the 20200519 WV2 scene had 5 such detections; two of which originated from the training target (Figure 5.13 *2*; Figure 5.14b). The three other pixel detections located two additional (potential) plastic clusters, as illustrated in Figure 5.13 *1* and *3*, and in Figure 5.14 a and c. Spectral signatures of the detected pixels were compared to the endmember input (Figure 5.15), revealing spectral characteristics similar to that of marine plastic debris. However, the MF scores were not consistent with target brightness, indicating that the abundance of plastic may have been overestimated in some pixels. For example, the pixel associated with the second highest MF score (0.65) also had the lowest reflectance signal in the NIR1 channel, which is an untypical behaviour for plastic debris.

Table 5.4: Number of pixels detected with >49% plastic abundance from the MTMF classification of the WorldView data.

Image and Sensor	Spatial Resolution	Detected Plastic Pixels
20200518, WV2	2.7 m	0
20200519, WV2	1.9 m	5
20200611, WV2	4.2 m	0
20200701, WV3	1.3 m	3

In the 20200701 WV3 image, three pixels were detected within the constraints of the MTMF classification. All three pixels were conformed to the same patch, as illustrated in Figure 5.16. No detections were found in proximity of Tracker D, whose position had been estimated through linear interpolation, despite efforts of adjusting MTMF thresholds. Spectral signatures of the three detections (Figure 5.17) were extracted from the ACOLITE processed multispectral and SWIR imagery, as ACOLITE proved to be the only algorithm to produce valid reflectance values in oceanic SWIR pixels. Two of these spectral profiles conveyed reflectance peaks at NIR (832 nm), while the third had a lower reflectance in this band (albeit higher than that of water pixels).

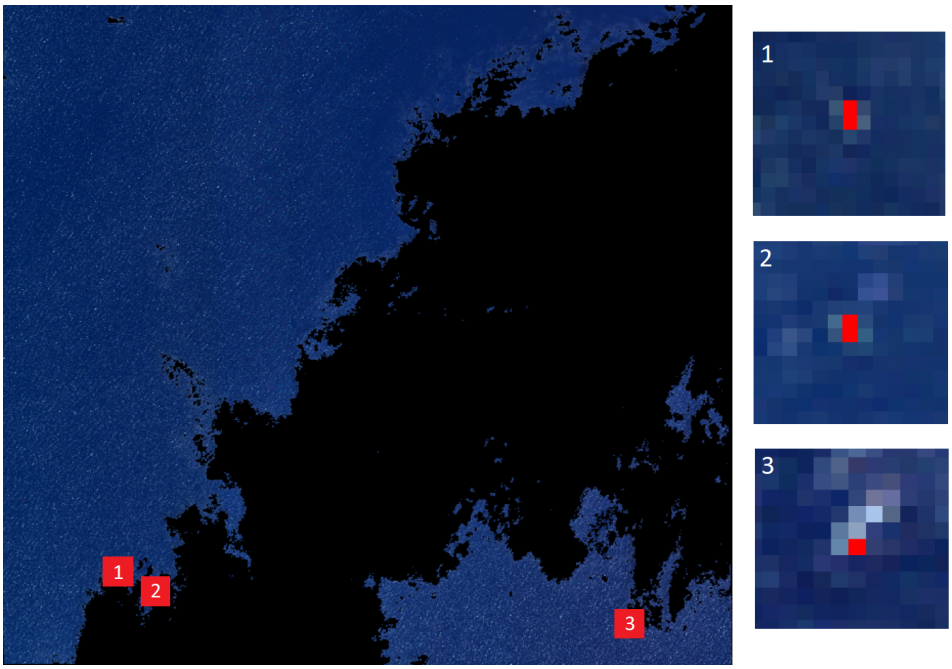

Figure 5.13: Relative location of the five detected pixels within the feasible region of MTMF classification. *WorldView-2 ©2020 DigitalGlobe, Inc., a Maxar company.*

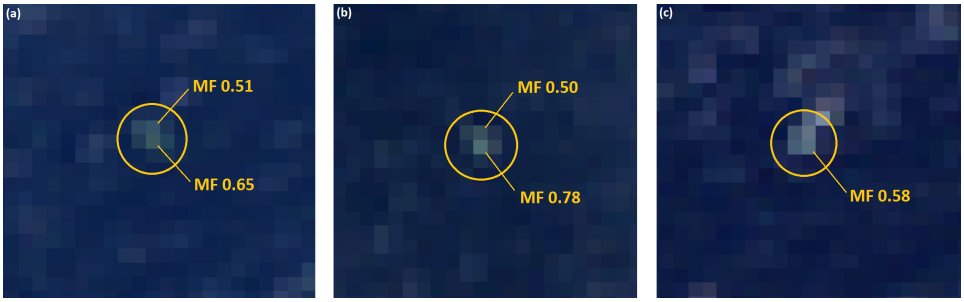

Figure 5.14: Detected pixels from MTMF classification of the 20200519 WorldView-2 image, indicating potential clusters of plastic debris (circled in yellow). (**b**) represents the known plastic patch from Tracker B, while (**a**) and (**c**) are located in different parts of the image without associated ground truth. *WorldView-2 ©2020 DigitalGlobe, Inc., a Maxar company.*

The SWIR spectra exhibited similar spectral characteristics for all detections (Figure 5.17). According to published literature, plastics are expected to have a spectral peak around 1600 nm (Topouzelis et al., 2019) and spectral absorption features around 931, 1215, 1417, 1732, and 2310 nm (Garaba et al., 2018; Maximenko et al., 2019; Martínez-Vicente et al., 2019; Dubucq et al., 2020). Although hyperspectral imagery is necessary for an accurate assessment, some

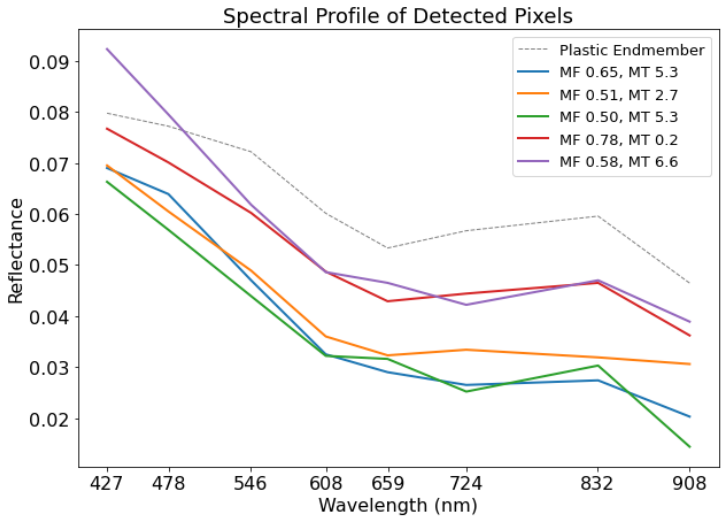

Figure 5.15: Spectral signatures of five detected plastic pixels in the 20200519 WV2 scene, based on MF and infeasibility thresholds of >0.49 and <8.5, respectively. The profiles are derived from the FLAASH corrected image.

evidence of such features were found from the 8-band SWIR image. The most evident absorption feature is seen at around 2200 nm, likely due to a higher spectral resolution around this band. Both the 1210 nm and 1730 nm bands show potential absorption characteristics, and the 1570 nm band could possibly represent a spectral crest. However, these suspicions cannot be confirmed due to coarseness in spectral resolution, and a minimum of three narrow wavebands (the absorption band itself, as well as one band to the left and one to the right of the crest of the absorption feature) are needed for accurate quantification and validation based on band depth.

Evaluated from a training class dataset on the 20200519 WV2 image, water (representing background) obtained matched filtering scores centred around zero[6] and with a standard deviation of 0.05. Infeasibility values were low for all instances, and the most extreme outlier had an MF score of 0.14 with corresponding MT value of 4.9. Whitecaps and spume appeared to have MF scores ranging from negative to 0.37, where higher scores (>0.2) generally were associated with infeasibility values of 12 or larger. Class values for water were found to be consistent across the WorldView imagery (evaluated from separate training datasets), but generally lower MF values were seen in the WV2 20200518 and 20200611 images for the whitecaps/spume class. For hazy pixels and cloud outlines falling outside the cloud mask, MF scores ranged from 0.02 to 0.51 with corresponding infeasibility scores floored at 1 and ceilinged at 19. All pixels in this class were outside the determined MTMF thresholds for

6. The majority of water pixels were on the negative side.

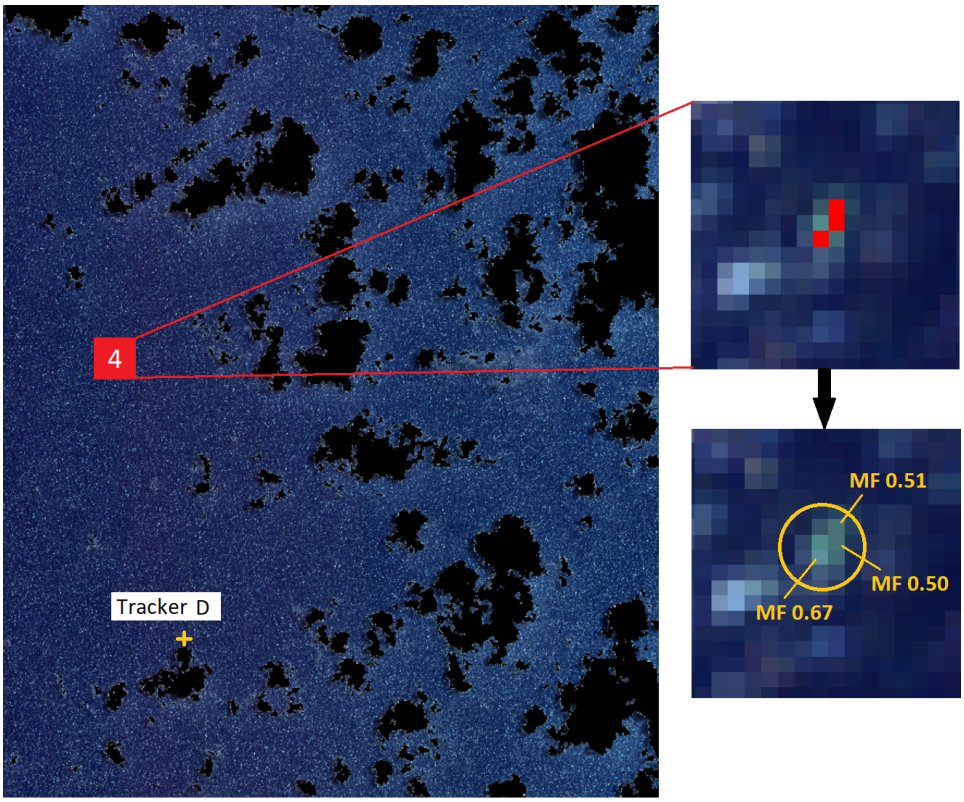

Figure 5.16: Detected pixels from MTMF classification of the 20200519 WorldView-3 image, where all three detections correspond to the same potential cluster of plastics (circled in yellow). The estimated position (through linear interpolation) of Tracker D is marked in yellow, but MTMF yielded no classified plastic pixels in proximity of this area. *WorldView-3 ©2020 DigitalGlobe, Inc., a Maxar company.*

all four scenes.

No plastic detections were made in either of the 20200518 and 20200611 WorldView-2 images. These results could be attributed to the scenes' lower spatial resolution (2.7 m and 4.2 m, respectively) affecting detection of small plastic targets. Because of this, MF and MT thresholds were adjusted in favour of facilitating detections of lower fractional coverage (<0.49), but no viable plastic pixels were found. Another factor impacting results could be owing to the images' heavy cloud cover, significantly decreasing the area in which plastics can be detected.

For the purpose of general exploration, the atmospherically corrected imagery was also processed with MTMF to assess differences in detection capabilities from that of TOA data. This resulted in an increased number of detected plastic

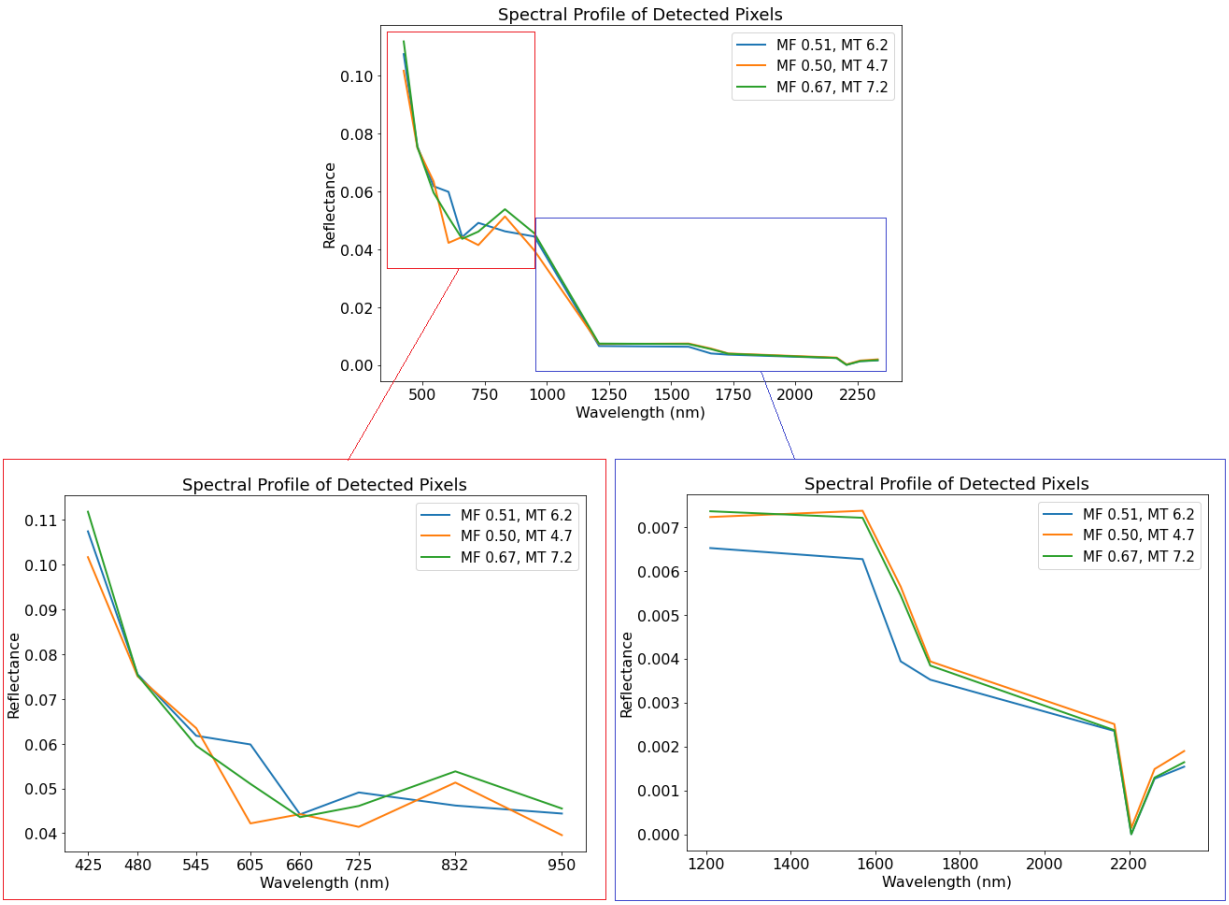

Figure 5.17: Spectral signatures of three detected plastic pixels in the 20200701 WV3 scene, based on MF and infeasibility thresholds of >0.49 and <8.5, respectively. The profiles are derived from the ACOLITE corrected image and split into separate multispectral and SWIR plots for better visualisation of spectral features.

pixels, although a majority were assumed to be false positives after inspection of associated spectral signatures. Additionally, the separability of plastic targets from other ocean surface features was significantly decreased[7], indicating that more robust AC schemes may be required for future research.

Uncertainties related to the MTMF method are introduced at various stages of its application. Indeed, without access to high-quality *in situ* data, it is possible that detected pixels are in fact other floating natural materials. From previous research (e.g., Biermann et al., 2020), driftwood/timber, seaweeds/algae, and

7. Similar MF and infeasibility scores for multiple classes obscured distinction between plastics and whitecaps/haze.

sea foam/spume have all been demonstrated to exhibit similar spectral characteristics as to that of plastics. Furthermore, the georeferencing step in image pre-processing performs a spatial resampling of pixels which can alter their values and affect MNF transformations (hence also MTMF results, although only minor effects are expected). The MTMF algorithm is also sensitive to illumination variations, which can cause both over- and underestimation of target abundance in a pixel. Detection probability is decreased with increasing cell sizes (i.e., lower spatial resolutions), as seen for the 20200518 and 20200611 WV2 imagery, suggesting that several true positives may go undetected. Moreover, because the MTMF processing is conducted with only one endmember, detected pixels are likely to be limited to a single material class of plastics (e.g., PET). Different types of plastic could therefore stay unclassified (undetected) without their endmember signature as input.

The MTMF algorithm does not rely on the endmember spectra in their original space, but rather on the target spectral signatures that exist solely in the MNF space (Routh et al., 2018). Therefore, accuracy of the abundance estimations may be improved by orthorectifying the imagery *after* MTMF classification, as the effects of spatial resampling are minimised. Such an approach should be evaluated for its effects in future research. Furthermore, as hazy areas within the shift difference region may affect the estimated noise statistics in the MNF transform, cloud mask accuracy is of high importance – particularly in imagery with strong presence of cloud cover, preventing the shift difference region from being selected in cloud-free areas.

5.7 Comparison of Detection Methods

In this study, three analytical methods have been explored for their ability to detect floating plastic litter on the ocean surface: the Spectral Angle Mapper (SAM), Mixture Tuned Matched Filtering (MTMF), and spectral indices in a three-dimensional feature space. The results, obtained from four individual WorldView scenes, are presented and compared in Table 5.5. Essentially, only two pixels were identified as plastics by all three methods – one of which was associated with the known plastic target (Fig. 5.12, pixel E), while the second corresponded to the patch illustrated in Figure 5.14a.

The SAM classification appeared to be the least viable algorithm in terms of true positives. In the 20200611 image, the SAM marked 89 pixels as plastic, whereas neither of the other two methods found any such candidates. This could indicate that thresholds should be determined adaptively based on each individual scene's spatial resolution and dynamic range, but also that the SAM algorithm may be generally unsuitable for detection of small plastic targets

Table 5.5: Results and comparison of three detection and mapping algorithms: 3D–SI (spectral indices in three-dimensional feature space: NDVI, WV-WCI, and RNDWI), MTMF (spectral unmixing), and SAM (supervised classification), applied to WorldView imagery.

Pixels Classified as Plastic in WorldView Images

Image	3D-SI	SAM	MTMF	Overlap 3D-SI+ SAM	Overlap 3D-SI+ MTMF	Overlap SAM+ MTMF	Overlap All
20200518	3	2	0	2	0	0	0
20200519	18	8	5	2	2	3	2
20200611	0	89	0	0	0	0	0
20200701	29	138	3	1	0	1	0

(due to poor separation between mixed target spectra and those of other ocean surface elements, e.g., whitecaps).

Despite its limitations, the Spectral Angle Mapper holds an advantage over the other two techniques. By comparing the angle between known and unknown spectra, the algorithm utilises only the direction and not the length of the spectral vector, making it insensitive to the gain factor caused by topographic illumination variations (Shrestha et al., 2002). In comparison, these effects represent a limiting factor in spectral unmixing methods, particularly in imagery affected by heavy cloud cover and cloud shadows, as the selection of endmembers can be biased by the varying illumination conditions. Nevertheless, cloud shadow influence has been shown to be negligible in the longer wavelength bands (Fig. 4.9), which is also the region where the spectral separation between plastics and seawater is greatest. Compared to the SAM, MTMF and the spectral indices tested here demonstrate higher robustness in the detection of mixed plastic pixels.

As no reference dataset or hot spot maps for plastic concentrations exist (specifically over the area encompassing the GPGP), it remains uncertain whether the amount of pixel detections can be considered a reasonable number. However, given the large spatial extent over which the imagery spans, as well as recent reports of floating plastic mass in the North Pacific Ocean[8], the WorldView scenes could be expected to contain substantially larger amounts of plastic litter than what was found, particularly for MTMF. It is likely, yet unconfirmable, that several true plastic pixels fall outside of the determined thresholds (i.e., false negatives). An increased number of ground truth training samples are therefore needed to properly assess the performance of the methods.

8. Estimates of 6,350–236,000 tonnes (Maximenko et al., 2019).

Lastly, it should be noted that inconsistency in pre-processing (i.e., top-of-atmosphere data was used for MTMF and the spectral indices, while bottom-of-atmosphere (FLAASH) data[9] was used for the SAM classification) implies that the various results should not be directly compared. Thus, Table 5.5 only serves as a summary of the obtained results across the WorldView imagery – not a rigorous assessment of algorithm performance.

9. Using TOA data for the SAM algorithm was found to produce no useful results as plastics could not be distinguished from whitecaps.

6

Conclusion

The exploratory nature of this study casts a wide net, and the qualitative data it collects cannot form the basis of sweeping generalisations. The methodological framework presented here represents first steps towards the detection of marine plastic debris, in which high-resolution satellite imagery is exploited for its spectral and spatial properties. Several parameters influence detection, including atmospheric correction algorithms, whitecaps, clouds, cloud shadows, image signal-to-noise ratio, surface reflected sun glint, debris density, floating non-anthropogenic materials (e.g., algae), and waves. At present, remote sensing technology and data analysis techniques are underdeveloped for accurate detection schemes to be established. However, evidence seen here indicates that marine plastic litter can be detected from space if accumulated into sufficiently large patches and, furthermore, is distinguishable from seawater and whitecaps for adequately abundant target fractions in a given pixel.

Literature has previously reported that floating plastics are seen from space as bright objects (Topouzelis et al., 2019). This is in agreement with the findings of this study, where a high pixel percentage coverage generally was associated with a high intensity signal. Furthermore, the observed spectral characteristics of plastic targets conformed to conventional spectra for marine debris found in previous research (e.g., Biermann et al. (2020); Kikaki et al. (2020)), with a sharp reflectance peak in the NIR region (831 nm central wavelength for the WorldView sensor). Atmospheric correction algorithms were demonstrated to enhance this reflectance feature, albeit with notable differences in magnitude and shape of the signal depending on the chosen AC

method. These differences were most evident in the ACOMP plastic spectrum, whereas ACOLITE and FLAASH produced more similar spectral responses. To determine the most appropriate algorithm for marine debris detection applications, future studies must evaluate the suitability of AC methodologies through rigorous intercomparison with the vastness of the Pacific Ocean in mind.

Detection capabilities of satellite instruments were also explored using top-of-atmosphere data. Although imagery (particularly those of different sensors) must be on a common radiometric scale for determining absolute thresholds in detection algorithms, TOA data represents a possible, yet temporary solution to the atmospheric correction problem. However, the effects of using at-sensor imagery should be investigated further.

Of the numerous GPS tracker recordings that were made for the sake of plastics detection (Table 3.6), only one of the markers (Tracker B) proved to be a reliable source for pinpointing floating plastics to a high degree of certainty. The lack of ground truth information was a severely limiting factor, particularly when determining class thresholds for the various detection algorithms. Still, the methods evaluated with the available data showed promising results in terms of possible plastic pixels, although with fewer feasible detections than expected. Nevertheless, spectral signatures for detected pixels were, in many cases, similar to those of known targets.

6.1 Suggestions for Future Work

A base requirement in all detection schemes is the availability of target end-member spectra, whose quality depend on the accuracy of atmospheric correction algorithms. Through intercomparison between different sensors and AC methodologies, accompanied by further research on spectral behaviour of various marine plastic types (in a real, aquatic environment), a reference dataset comprising high-quality spectral signatures of marine debris can be produced. Access to generalised training data is crucial for automation in large-scale detection systems, and for the derivation of accurate and continuous spectra, hyperspectral imagery (e.g., PRISMA and the upcoming PACE[1] mission) should be employed. Combining the high spatial resolution of broadband sensors with the fine spectral resolution of hyperspectral instruments presents an opportunity to gather extensive spectral information on smaller plastic targets and is a natural next step in marine litter research.

1. A NASA Earth observation spacecraft scheduled for launch in 2022. More info can be found at: `https://pace.oceansciences.org`.

Reliable ground truth data is of utmost importance for further advancement in detection algorithms. New machine learning techniques, in which models are trained for debris detection with minimal requirement of human interference, should be explored; yet such tasks demand abundant high-quality *in situ* data. A cost-effective tool for collecting ground truth information could be the deployment of unmanned aerial vehicles (UAVs) from clean-up vessels in the area of interest to capture high-resolution imagery of plastic targets. This would allow for a more accurate derivation of plastic endmembers via spectral unmixing methods but would also require intricate logistics (e.g., timing with satellite overpasses). Another and perhaps more viable option could be to have an increased number of GPS trackers attached to very large plastic conglomerates to facilitate full-pixel coverage for a high-resolution sensor (e.g., WorldView-2/-3). Furthermore, a higher frequency of logged positions of existing GPS trackers, especially in proximity of image capture time, would significantly increase chances of detection (provided cloud-free observing conditions).

The use of high-resolution SAR systems should also be subject to research, given their ability to observe the surface regardless of solar illumination and cloud cover. If used together with frequent GPS tracker information, SAR technology has the potential to provide comprehensive descriptions of floating plastic dynamics, such as its profile above sea level, drift velocities relative to surrounding waters, and dampening effects on surrounding waves (Maximenko et al., 2019). To fully understand marine plastic behaviour, and to advance towards automated detection algorithms, such characteristics are of high importance.

A recurrent problem with plastic debris detection is the environmental perturbations from other ocean bright targets (breaking waves, spume, whitecaps, sun glint). Therefore, to attenuate the proportion of false positives, this study suggests a multitemporal approach in which subsequent images of the same area are acquired with delays of a few minutes. In this time, wave patterns will have reformed from those of the initial image and can be identified as such, while plastic patches will likely not have moved far from their original position. Combined with abundant GPS tracker information, this technique could enable accurate distinction of plastics from dynamic ocean surface features.

Signal-to-noise ratios represent another key parameter in spectral target detection algorithms. Since marine plastic aggregations produce a weak signal (Topouzelis et al., 2020), future campaigns should work towards a complete assessment of different sensors' detection capabilities. Based on band-specific SNRs, one can estimate the minimum concentrations that can be accurately detected, as well as determine appropriate bands for spectral indices or band

boosting[2]. This evaluation is also necessary to determine an optimal SNR for future satellite missions aimed at marine litter detection.

Lastly, in the advent of supervised machine learning algorithms, cross-validation should be introduced as an evaluation tool to assess the performance of various detection methodologies and classification models. Requiring high-quality *in situ* data, this approach is advised after a generic ground truth reference dataset has been established, but it could also be used following an extensive field campaign. In future research, cross-validation could serve as a critical component in computing model accuracies and should be preferred over user-directed, interactive accuracy analysis as this study has been limited to.

2. Fusion of two or more bands for enhancing spectral characteristics of a target material.

References

Airbus Defence and Space (2021). *SPOT 6/7 User Guide*. Document. URL: https://www.intelligence-airbusds.com/en/8718-user-guides.

Aoyama, T. (2016). "Extraction of marine debris in the Sea of Japan using high-spatial-resolution satellite images." In: *Remote Sensing of the Oceans and Inland Waters: Techniques, Applications, and Challenges*. DOI: https://doi.org/10.1117/12.2220370.

Bayen, A. M. and T. Siauw (2015). *An Introduction to MATLAB® Programming and Numerical Methods for Engineers*. Boston: Academic Press. ISBN: 978-0-12-420228-3. DOI: https://doi.org/10.1016/B978-0-12-420228-3.00021-X. URL: https://www.sciencedirect.com/science/article/pii/B978012420228300021X.

Beaumont, N. J., M. Aanesen, et al. (2019). "Global ecological, social and economic impacts of marine plastic." In: *Marine Pollution Bulletin* 142, pp. 189–195. ISSN: 1879-3363 (Electronic) 0025-326X (Linking). DOI: 10.1016/j.marpolbul.2019.03.022. URL: https://www.ncbi.nlm.nih.gov/pubmed/31232294.

Bhatt, J. S. and M. V. Joshi (2016). *Regularization in Hyperspectral Unmixing*. Vol. 146. Spie, p. 44. ISBN: 9781510607590. DOI: 10.1117/3.2264037.

Biermann, L., D. Clewley, V. Martinez-Vicente, and K. Topouzelis (2020). "Finding Plastic Patches in Coastal Waters Using Optical Satellite Data." In: *Scientific Reports* 10.1, p. 5364. ISSN: 2045-2322 (Electronic) 2045-2322 (Linking). DOI: 10.1038/s41598-020-62298-z. URL: https://www.ncbi.nlm.nih.gov/pubmed/32327674.

Biermann, L., V. Martinez-Vicente, S. Sailley, A. Mata, and C. Steele (2019). *Towards a Method for Detecting Macroplastics by Satellite: Examining Sentinel-2 Earth Observation Data for Floating Debris in the Coastal Zone*. Conference Paper. URL: https://ui.adsabs.harvard.edu/abs/2019EGUGA..2117469B.

Boardman, J. W. (1998). "Leveraging the High Dimensionality of AVIRIS Data for improved Sub-Pixel Target Unmixing and Rejection of False Positives: Mixture Tuned Matched Filtering." In: *Summaries of the Seventh JPL Airborne Geoscience Workshop* 97, pp. 55–56.

Boardman, J. W. and F. A. Kruse (2011). "Analysis of Imaging Spectrometer Data Using N-Dimensional Geometry and a Mixture-Tuned Matched Filtering Approach." In: *IEEE Transactions on Geoscience and Remote Sensing* 49.11,

pp. 4138–4152. ISSN: 0196-2892 1558-0644. DOI: 10.1109/tgrs.2011.2161585.

Carder, K. L., P. Reinersman, and R. F. Chen (1993). "AVIRIS calibration using the cloud-shadow method." In: *Summaries of the Fourth Annual JPL Airborne Geoscience Workshop* 1, pp. 15–18.

CCRS (2019). *Fundamentals of Remote Sensing*. Remote Sensing Tutorials. Canada Centre for Mapping and Earth Observation. URL: https://www.nrcan.gc.ca/sites/www.nrcan.gc.ca/files/earthsciences/pdf/resource/tutor/fundam/pdf/fundamentals_e.pdf.

Cheng, P. and C. Chuck (2010). "Pan-sharpening and Geometric Correction - WorldView-2 Satellite." In: *PCI Geomatics*.

Corbari, L., A. Maltese, F. Capodici, M. C. Mangano, G. Sara, and G. Ciraolo (2020). "Indoor spectroradiometric characterization of plastic litters commonly polluting the Mediterranean Sea: toward the application of multispectral imagery." In: *Scientific Reports* 10.1, p. 19850. ISSN: 2045-2322 (Electronic) 2045-2322 (Linking). DOI: 10.1038/s41598-020-74543-6. URL: https://www.ncbi.nlm.nih.gov/pubmed/33199690.

Dominici, D., S. Zollini, M. Alicandro, F. Della Torre, P. Buscema, and V. Baiocchi (2019). "High Resolution Satellite Images for Instantaneous Shoreline Extraction Using New Enhancement Algorithms." In: *Geosciences* 9.3. ISSN: 2076-3263. DOI: 10.3390/geosciences9030123.

Dubucq, D., R. Jatiault, P. Boymond, and A. Rusquet (2020). "Remote sensing detection of plastic waste: recent improvements and remaining challenges." In: *Earth Resources and Environmental Remote Sensing/GIS Applications XI* 11534. DOI: https://doi.org/10.1117/12.2574026.

Elachi, C. and J. v. Zyl (2006). *Introduction to the Physics and Techniques of Remote Sensing*. 2nd ed. John Wiley and Sons, p. 558.

Fallati, L., A. Polidori, C. Salvatore, L. Saponari, A. Savini, and P. Galli (2019). "Anthropogenic Marine Debris assessment with Unmanned Aerial Vehicle imagery and deep learning: A case study along the beaches of the Republic of Maldives." In: *Science of The Total Environment* 693, p. 133581. ISSN: 0048-9697. DOI: https://doi.org/10.1016/j.scitotenv.2019.133581. URL: https://www.sciencedirect.com/science/article/pii/S0048969719335065.

Garaba, S. P., J. Aitken, B. Slat, H. M. Dierssen, L. Lebreton, O. Zielinski, and J. Reisser (2018). "Sensing Ocean Plastics with an Airborne Hyperspectral Shortwave Infrared Imager." In: *Environmental Science & Technology* 52.20, pp. 11699–11707. ISSN: 1520-5851 (Electronic) 0013-936X (Linking). DOI: 10.1021/acs.est.8b02855. URL: https://www.ncbi.nlm.nih.gov/pubmed/30249095.

Garaba, S. P. and O. Zielinski (July 2013). "Comparison of remote sensing reflectance from above-water and in-water measurements west of Greenland, Labrador Sea, Denmark Strait, and west of Iceland." In: *Opt. Express*

21.13, pp. 15938–15950. DOI: 10.1364/OE.21.015938. URL: http://www.opticsexpress.org/abstract.cfm?URI=oe-21-13-15938.

Goddijn-Murphy, L., S. Peters, E. van Sebille, N. A. James, and S. Gibb (2018). "Concept for a hyperspectral remote sensing algorithm for floating marine macro plastics." In: *Marine Pollution Bulletin* 126, pp. 255–262. ISSN: 1879-3363 (Electronic) 0025-326X (Linking). DOI: 10.1016/j.marpolbul.2017.11.011. URL: https://www.ncbi.nlm.nih.gov/pubmed/29421096.

González, C., J. Resano, D. Mozos, A. Plaza, and D. Valencia (2010). "FPGA Implementation of the Pixel Purity Index Algorithm for Remotely Sensed Hyperspectral Image Analysis." In: *EURASIP Journal on Advances in Signal Processing* 2010.1. ISSN: 1687-6180. DOI: 10.1155/2010/969806.

Harris Geospatial Solutions (2020). *Documentation Center - ENVI*. URL: https://www.l3harrisgeospatial.com/docs/.

HSU (2014). *Image Classification*. Introduction to Remote Sensing - Learning Module 6.1. Humboldt State University. URL: http://gsp.humboldt.edu/OLM/Courses/GSP_216_Online/lesson6-1/index.html.

Hu, C. (2009). "A novel ocean color index to detect floating algae in the global oceans." In: *Remote Sensing of Environment* 113.10, pp. 2118–2129. ISSN: 00344257. DOI: 10.1016/j.rse.2009.05.012.

Hu, C. and M.-X. He (2008). "Origin and offshore extent of floating algae in Olympic sailing area." In: *EOS* 89.33, 302-303. DOI: https://doi.org/10.1029/2008EO330002.

Huang, X., J. Zhu, B. Han, C. Jamet, Z. Tian, Y. Zhao, J. Li, and T. Li (2019). "Evaluation of Four Atmospheric Correction Algorithms for GOCI Images over the Yellow Sea." In: *Remote Sensing* 11.14. ISSN: 2072-4292. DOI: 10.3390/rs11141631. URL: https://www.mdpi.com/2072-4292/11/14/1631.

ITT Visual Information Solutions (2009). *Atmospheric Correction Module: QUAC and FLAASH User's Guide*. Atmospheric Correction Module version 4.7. URL: https://www.l3harrisgeospatial.com/portals/0/pdfs/envi/flaash_module.pdf.

Jawak, S. D., S. F. Wankhede, and A. J. Luis (2019). "Explorative Study on Mapping Surface Facies of Selected Glaciers from Chandra Basin, Himalaya Using WorldView-2 Data." In: *Remote Sensing* 11.10. ISSN: 2072-4292. DOI: 10.3390/rs11101207.

Jeon, G., S. Kang, and Y.-S. Lee (2012). *Noise Level Estimation for Image Processing*. Ed. by G. Lee, D. Howard, and J. J. Kang. Berlin, Heidelberg: Springer Berlin Heidelberg, pp. 350–356. ISBN: 978-3-642-32645-5.

Kikaki, A., K. Karantzalos, C. A. Power, and D. E. Raitsos (2020). "Remotely Sensing the Source and Transport of Marine Plastic Debris in Bay Islands of Honduras (Caribbean Sea)." In: *Remote Sensing* 12.11. ISSN: 2072-4292. DOI: 10.3390/rs12111727.

Kornei, K. (2019). *Satellite Imagery Reveals Plastic Garbage in the Ocean*. Newspaper Article. URL: eos.org/articles/satellite-imagery-reveals-plastic-garbage-in-the-ocean.

Koutroumbas, K. and S. Theodoridis (2009). *Pattern Recognition*. 4th ed. Elsevier Inc., p. 984.

Kruse, F. A., W. Baugh, and S. Perry (May 2015). "Validation of DigitalGlobe WorldView-3 Earth imaging satellite shortwave infrared bands for mineral mapping." In: *Journal of Applied Remote Sensing* 9. DOI: 10.1117/1.JRS.9.096044.

Kruse, F. A., A. B. Lefkoff, J. W. Boardman, K. B. Heidebrecht, A. T. Shapiro, P. J. Barloon, and A. F. H. Goetz (1993). "The spectral image processing system (SIPS)—interactive visualization and analysis of imaging spectrometer data." In: *Remote Sensing of Environment* 44.2. Airbone Imaging Spectrometry, pp. 145–163. ISSN: 0034-4257. DOI: https://doi.org/10.1016/0034-4257(93)90013-N. URL: https://www.sciencedirect.com/science/article/pii/003442579390013N.

Kuester, M. A. (2017). *Absolute Radiometric Calibration 2016v0*. DigitalGlobe Adjustment Factors.

Laben, C. A. and B. V. Brower (2000). "Process For Enhancing The Spatial Resolution Of Multispectral Imagery Using Pan-sharpening." Granted Patent US 6011875 A (United States). URL: https://lens.org/135-660-046-023-136.

Lebreton, L., B. Slat, et al. (2018). "Evidence that the Great Pacific Garbage Patch is rapidly accumulating plastic." In: *Scientific Reports* 8.4666. DOI: https://doi.org/10.1038/s41598-018-22939-w.

Liang, S., X. Li, and J. Wang (2012). *Advanced Remote Sensing: Terrestrial Information Extraction and Applications*. 1st ed. Academic Press. Chap. 1, pp. 1–31.

Lillesand, T. M., J. Wright, and R. W. Kiefer (2004). *Remote Sensing and Image Interpretation*. 5th ed. Vol. 146. The Geographical Journal. Wiley. ISBN: 00167398. DOI: 10.2307/634969.

Lisens, G., P. Kempencers, F. Fierens, and J. Van Rensbergen (2000). "Development of cloud, snow, and shadow masking algorithms for VEGETATION imagery." In: *IGARSS 2000. IEEE 2000 International Geoscience and Remote Sensing Symposium. Taking the Pulse of the Planet: The Role of Remote Sensing in Managing the Environment. Proceedings (Cat. No.00CH37120)*. Vol. 2, 834–836 vol.2. DOI: 10.1109/IGARSS.2000.861719.

Liubartseva, S., G. Coppini, R. Lecci, and E. Clementi (2018). "Tracking plastics in the Mediterranean: 2D Lagrangian model." In: *Mar Pollut Bull* 129.1, pp. 151–162. ISSN: 1879-3363 (Electronic) 0025-326X (Linking). DOI: 10.1016/j.marpolbul.2018.02.019. URL: https://www.ncbi.nlm.nih.gov/pubmed/29680533.

Mansui, J., G. Darmon, T. Ballerini, O. van Canneyt, Y. Ourmieres, and C. Miaud (Mar. 2020). "Predicting marine litter accumulation patterns in the Mediterranean basin: Spatio-temporal variability and comparison with empirical data." In: *Progress in Oceanography* 182, p. 102268. DOI: 10.1016/j.pocean.2020.102268.

Martínez-Vicente, V., J. R. Clark, et al. (2019). "Measuring Marine Plastic Debris from Space: Initial Assessment of Observation Requirements." In: *Remote Sensing* 11.20, pp. 2243–2262. ISSN: 2072-4292. DOI: 10.3390/rs11202443. URL: www.mdpi.com/2072-4292/11/20/2443/htm.

Maxar Technologies (2020). *Atmospheric Compensation*. Data Sheet.

Maximenko, N., P. Corradi, et al. (2019). "Toward the Integrated Marine Debris Observing System." In: *Frontiers in Marine Science* 6. ISSN: 2296-7745. DOI: 10.3389/fmars.2019.00447.

Mehr, S., V. Ahadnejad, R. Abbaspour, and M. Hamzeh (May 2013). "Using the mixture-tuned matched filtering method for lithological mapping with Landsat TM5 images." In: *International Journal of Remote Sensing* 34, pp. 8803–8816. DOI: 10.1080/01431161.2013.853144.

Meyerjürgens, J., T. H. Badewien, S. P. Garaba, J.-O. Wolff, and O. Zielinski (2019). "A State-of-the-Art Compact Surface Drifter Reveals Pathways of Floating Marine Litter in the German Bight." In: *Frontiers in Marine Science* 6. ISSN: 2296-7745. DOI: 10.3389/fmars.2019.00058.

Micalizio, C.-S. (2019). *Great Pacific Garbage Patch*. National Geographic - Encyclopedic Entry. URL: https://www.nationalgeographic.org/encyclopedia/great-pacific-garbage-patch.

Mitchell, J. J. and N. F. Glenn (2009). "Subpixel abundance estimates in mixture-tuned matched filtering classifications of leafy spurge (Euphorbia esula L.)" In: *International Journal of Remote Sensing* 30.23, pp. 6099–6119. DOI: 10.1080/01431160902810620.

Moy, K., B. Neilson, A. Chung, A. Meadows, M. Castrence, S. Ambagis, and K. Davidson (2018). "Mapping coastal marine debris using aerial imagery and spatial analysis." In: *Marine Pollution Bulletin* 132, pp. 52–59. ISSN: 1879-3363 (Electronic) 0025-326X (Linking). DOI: 10.1016/j.marpolbul.2017.11.045. URL: https://www.ncbi.nlm.nih.gov/pubmed/29273243.

Mundt, J. T., D. R. Streutker, and N. F. Glenn (2007). *Partial Unmixing of Hyperspectral Imagery: Theory and Methods*. ASPRS Annual Conference. Tampa, Florida.

NOAA (2021). *Garbage Patches*. Web Page, Marine Debris Program. URL: https://marinedebris.noaa.gov/info/patch.html.

Papachristopoulou, I., A. Filippides, E. Fakiris, and G. Papatheodorou (2020). "Vessel-based photographic assessment of beach litter in remote coasts. A wide scale application in Saronikos Gulf, Greece." In: *Marine Pollution Bulletin* 150, p. 110684. ISSN: 0025-326X. DOI: https://doi.org/10.1016/j.marpolbul.2019.110684. URL: https://www.sciencedirect.com/science/article/pii/S0025326X19308409.

Pichel, W. G., J. H. Churnside, T. S. Veenstra, D. G. Foley, K. S. Friedman, R. E. Brainard, J. B. Nicoll, Q. Zheng, and P. Clemente-Colon (2007). "Marine debris collects within the North Pacific Subtropical Convergence Zone." In: *Marine Pollution Bulletin* 54.8, pp. 1207–1211. ISSN: 0025-326X (Print)

0025-326X (Linking). DOI: 10.1016/j.marpolbul.2007.04.010. URL: https://www.ncbi.nlm.nih.gov/pubmed/17568624.

Plaza, A., P. Martinez, R. Perez, and J. Plaza (2002). "Spatial/spectral endmember extraction by multidimensional morphological operations." In: *IEEE Transactions on Geoscience and Remote Sensing* 40.9, pp. 2025–2041. ISSN: 0196-2892. DOI: 10.1109/tgrs.2002.802494.

Politikos, D. V., C. Ioakeimidis, G. Papatheodorou, and K. Tsiaras (2017). "Modeling the Fate and Distribution of Floating Litter Particles in the Aegean Sea (E. Mediterranean)." In: *Frontiers in Marine Science* 4, p. 191. ISSN: 2296-7745. DOI: 10.3389/fmars.2017.00191. URL: https://www.frontiersin.org/article/10.3389/fmars.2017.00191.

Prevenios, M., C. Zeri, C. Tsangaris, S. Liubartseva, E. Fakiris, and G. Papatheodorou (2018). "Beach litter dynamics on Mediterranean coasts: Distinguishing sources and pathways." In: *Marine Pollution Bulletin* 129.2, pp. 448–457. ISSN: 0025-326X. DOI: https://doi.org/10.1016/j.marpolbul.2017.10.013. URL: https://www.sciencedirect.com/science/article/pii/S0025326X17308305.

Reed, I. and X. Yu (1990). "Adaptive multiple-band CFAR detection of an optical pattern with unknown spectral distribution." In: *IEEE Transactions on Acoustics, Speech, and Signal Processing* 38.10, pp. 1760–1770. DOI: 10.1109/29.60107.

Rizeei, H. M. and B. Pradhan (2019). "Urban Mapping Accuracy Enhancement in High-Rise Built-Up Areas Deployed by 3D-Orthorectification Correction from WorldView-3 and LiDAR Imageries." In: *Remote Sensing* 11.6. ISSN: 2072-4292. DOI: 10.3390/rs11060692. URL: https://www.mdpi.com/2072-4292/11/6/692.

Rochman, C. M., A. Tahir, S. L. Williams, D. V. Baxa, R. Lam, J. T. Miller, F. C. Teh, S. Werorilangi, and S. J. Teh (2015). "Anthropogenic debris in seafood: Plastic debris and fibers from textiles in fish and bivalves sold for human consumption." In: *Scientific Reports* 5, p. 14340. ISSN: 2045-2322 (Electronic) 2045-2322 (Linking). DOI: 10.1038/srep14340. URL: https://www.ncbi.nlm.nih.gov/pubmed/26399762.

Rouse, J., R. H. Haas, J. A. Schell, and D. Deering (1973). "Monitoring vegetation systems in the Great Plains with ERTS." In: *Third Earth Resources Technology Satellite-1 Symposium* 1, 309-317.

Routh, D., L. Seegmiller, C. Bettigole, C. Kuhn, C. D. Oliver, and H. B. Glick (2018). "Improving the Reliability of Mixture Tuned Matched Filtering Remote Sensing Classification Results Using Supervised Learning Algorithms and Cross-Validation." In: *Remote Sensing* 10.11. ISSN: 2072-4292. DOI: 10.3390/rs10111675. URL: https://www.mdpi.com/2072-4292/10/11/1675.

Sebille, E. van, S. Aliani, et al. (Feb. 2020). "The physical oceanography of the transport of floating marine debris." In: *Environmental Research Letters* 15.2, p. 023003. DOI: 10.1088/1748-9326/ab6d7d. URL: https://doi.org/10.1088/1748-9326/ab6d7d.

Shrestha, D. P., D. Margate, V. A. Hoang, and F. Meer (Aug. 2002). "Spectral unmixing versus spectral angle mapper for land degradation assessment: a case study in southern Spain." In: *World Congress of Soil Science*. Bangkok, Thailand, pp. 1–10.

Suaria, G. and S. Aliani (2014). "Floating debris in the Mediterranean Sea." In: *Marine Pollution Bulletin* 86.1, pp. 494–504. ISSN: 0025-326X. DOI: https://doi.org/10.1016/j.marpolbul.2014.06.025. URL: https://www.sciencedirect.com/science/article/pii/S0025326X14004056.

The Ocean Cleanup (2021). *The Great Pacific Garbage Patch*. Web Page. URL: https://theoceancleanup.com/great-pacific-garbage-patch/.

Themistocleous, K., C. Papoutsa, S. Michaelides, and D. Hadjimitsis (2020). "Investigating Detection of Floating Plastic Litter from Space Using Sentinel-2 Imagery." In: *Remote Sensing* 12.16. ISSN: 2072-4292. DOI: 10.3390/rs12162648.

Thiel, M., I. A. Hinojosa, T. Joschko, and L. Gutow (2011). "Spatio-temporal distribution of floating objects in the German Bight (North Sea)." In: *Journal of Sea Research* 65.3, pp. 368–379. ISSN: 13851101. DOI: 10.1016/j.seares.2011.03.002.

Topouzelis, K., D. Papageorgiou, A. Karagaitanakis, A. Papakonstantinou, and M. Arias Ballesteros (2020). "Remote Sensing of Sea Surface Artificial Floating Plastic Targets with Sentinel-2 and Unmanned Aerial Systems (Plastic Litter Project 2019)." In: *Remote Sensing* 12.12. ISSN: 2072-4292. DOI: 10.3390/rs12122013.

Topouzelis, K., A. Papakonstantinou, and S. P. Garaba (2019). "Detection of floating plastics from satellite and unmanned aerial systems (Plastic Litter Project 2018)." In: *International Journal of Applied Earth Observation and Geoinformation* 79, pp. 175–183. ISSN: 03032434. DOI: 10.1016/j.jag.2019.03.011. URL: https://www.sciencedirect.com/science/article/abs/pii/S0303243419301163.

Vanhellemont, Q. (Sept. 2020). "Sensitivity analysis of the dark spectrum fitting atmospheric correction for metre- and decametre-scale satellite imagery using autonomous hyperspectral radiometry." In: *Opt. Express* 28.20, pp. 29948–29965. DOI: 10.1364/OE.397456. URL: http://www.opticsexpress.org/abstract.cfm?URI=oe-28-20-29948.

Vanhellemont, Q. and K. Ruddick (2018). "Atmospheric correction of metre-scale optical satellite data for inland and coastal water applications." In: *Remote Sensing of Environment* 216, pp. 586–597. ISSN: 00344257. DOI: 10.1016/j.rse.2018.07.015.

Verdoja, F. and M. Grangetto (2020). "Graph Laplacian for image anomaly detection." In: *Machine Vision and Applications* 31.1-2. ISSN: 0932-8092 1432-1769. DOI: 10.1007/s00138-020-01059-4.

Vince, J. and B. D. Hardesty (2017). "Plastic pollution challenges in marine and coastal environments: from local to global governance." In: *Restoration Ecology* 25.1, pp. 123–128. ISSN: 10612971. DOI: 10.1111/rec.12388.

Weyermann, J., D. Schläpfer, A. Hueni, M. Kneubühler, and M. Schaepman (2009). "Spectral Angle Mapper (SAM) for anisotropy class indexing in imaging spectrometry data." In: *Imaging Spectrometry XIV*. Ed. by S. S. Shen and P. E. Lewis. Vol. 7457. International Society for Optics and Photonics. SPIE, pp. 67–78. DOI: 10.1117/12.825991.